Doctoral Thesis

Study of the Magnetic-Field and Pressure Effects on the Metal-to-Insulator Transition System $BaVS_3$

Taimu Tahara

Department of Physics, Graduate School of Science

Osaka University

February, 2020

Abstract

This thesis presents a series of studies to elucidate the complex electronic properties of the metal-to-insulator transition compound $BaVS_3$, in which physical phenomena originating from multiple degrees of freedom such as spin, orbital, lattice and charge are driven by their correlation. The physical properties of $BaVS_3$ are so complicated that misunderstandings about them often occurred and their interpretation has been still under debate.

$BaVS_3$ has a hexagonal perovskite-type structure (space group: $P6_3/mmc$), where face sharing VS_6 octahedral compose a spin chain along the c-direction. The metal-to-insulator transition in $BaVS_3$ takes place at $T_{\mathrm{MI}} \sim 70$K accompanied by the formation of charge density waves. Although various studies on this material revealed that one-dimensional Peierls instability is important in determining physical properties of $BaVS_3$, few studies have focused on magnetism, and the magnetic properties of $BaVS_3$ are almost unclear. Since vanadium ions have a formal valence of V^{4+}, it had been assumed that the localized spin of $S = 1/2$ plays a role in magnetism. Although this interpretation has been widely accepted, through detailed analysis of magnetic susceptibility, it turns out that localized spin model discussed in previous researches does not reproduce the experimental results even in a high temperature paramagnetic state.

Applying a pressure to the system is a powerful way to elucidate the electronic state with complex internal degrees of freedom. In general, characteristic energy such as elastic energy of a crystal structure and Coulomb repulsion between electrons can be adjusted by applying a hydrostatic pressure. In the case of $BaVS_3$, it has been reported that the MI transition is suppressed by applying critical pressure p_{cr} of 2.2 GPa. Thus, we have performed magnetic susceptibility and high-field magnetization measurements under high pressure with the expectation that a significant change of magnetism would occur. Because there was no experimental environment that could measure under the combination of the required high pressure and high magnetic fields, we started by developing the measurement method. As a result, small changes in the magnetization of this material could be measured under high pressure of 1.15 GPa and pulsed high magnetic fields up to about 50 T.

From the magnetization measurement using the above measuring methods, it was found that 67 % of the total amount of magnetic moment was involved in a metamagnetic transition in $BaVS_3$ with a critical pressure p_{M} of 0.90 GPa, where the transition must be suppressed to 0 T. This critical pressure p_{M} is significantly smaller than the critical pressure p_{cr} for destructing the charge density wave.

From the results of magnetic susceptibility measurements, we found an anomaly at $T_{\mathrm{a}} \sim 60$ K, which is in addition to the metal-to-insulator transition (at $T_{\mathrm{MI}} \sim 70$ K) and a magnetic ordering (at $T_{\mathrm{N}} \sim 30$K). This anomaly has the critical pressure p_{M} of 0.90 GPa, which is the same as that for the metamagnetic transition, and was found to be related to the formation of a spin gap. Accordingly, we have revealed that two spin gaps and (at least) one charge gap opens below the metal-to-insulator transition temperature T_{MI}. We have reconstructed the discussion by considering metallic magnetism. We hypothesized two models, c-d hybridization model and multiple Peierls transition model, and showed that these models could explain most of the magnetism in $BaVS_3$.

Contents

1 Introduction

1.1 Review of metal-to-insulator transition

According to the Landau mean field theory,[1] quantum fluctuations diverge and some coherent order parameter is realized at the boundary between two different states. That is, in the vicinity of the phase transition, it is expected that novel physical properties that are macroscopically affected by the quantum effect are observed. A typical example of such phase transition is a metal-to-insulator (MI) transition in which the electric resistivity changes up to about ten orders of magnitude. The MI transition is a common phenomenon in condensed matter physics. [2] Since charge degrees of freedom combine with many degrees of freedom inside matter and various transition mechanisms exist, the MI transition is one of the most important and interesting phenomena in condensed matter physics.

Our research target $BaVS_3$ shows clearly a MI transition with formation of superlattice and decrease in susceptibility at $T_{\mathrm{MI}} \sim 70$ K. This material has a quasi-one-dimensional structure along the c-axis direction and the Peierls instability plays an important role in determination of physical properties. To assist in understanding the complex MI transitions of this material, we present in this section typical examples of "structure-driven","charge-driven", and "magnetism-driven" MI transitions and their properties.

1.1.1 Peierls transition

The Peierls transition is a phase transition in which Fermi surface instability and periodic distortion of lattice cooperatively occur due to electron-lattice interaction.[3] This phase transition originates from **one-dimensional structural instability** and is a common phenomenon in one-dimensional electron systems with weak electron-electron correlation.

Figure 1.1 gives a classic explanation of the change in the electron system accompanying the Peierls transition. Since the energy of phonon is smaller than that of electrons, only phonon near the Fermi wave number interact with electrons according to the requirement of the law of conservation of energy. This causes the softening of the phonon at $Q = 2k_{\mathrm{F}}$, and the softened phonon combine with the modulation of the electron density. As a result, a charge density wave (CDW) appears, and a static twice-period structure appears in the lattice system, and system becomes an insulator. Next, the degree of freedom of the spin system is also considered. If the anti-ferro magnetic exchange interaction between the nearest neighbor spins is modulated, a gapped spin-singlet state may occur simultaneously with the Peierls transition.[4]

A typical example of Peierls transition, a molecular conductor $TTF(SCN)_{0.54}$ is shown in Fig. 1.2. [5] The TTF molecule is composed of two five-membered rings, and in TTF (SCN), (a, b)the molecules are stacked in the c-axis direction and connected one-dimensionally. (c) Above 200K, it exhibits metallic temperature-dependent electric conductivity. In the temperature range of 200 - 140 K, the electric conductivity decreases rapidly, and becomes zero at 140 K, and the material becomes insulator. Anomalous decrease is also seen in (dia-)magnetic susceptibility in the same temperature range as the decrease in electric conductivity.

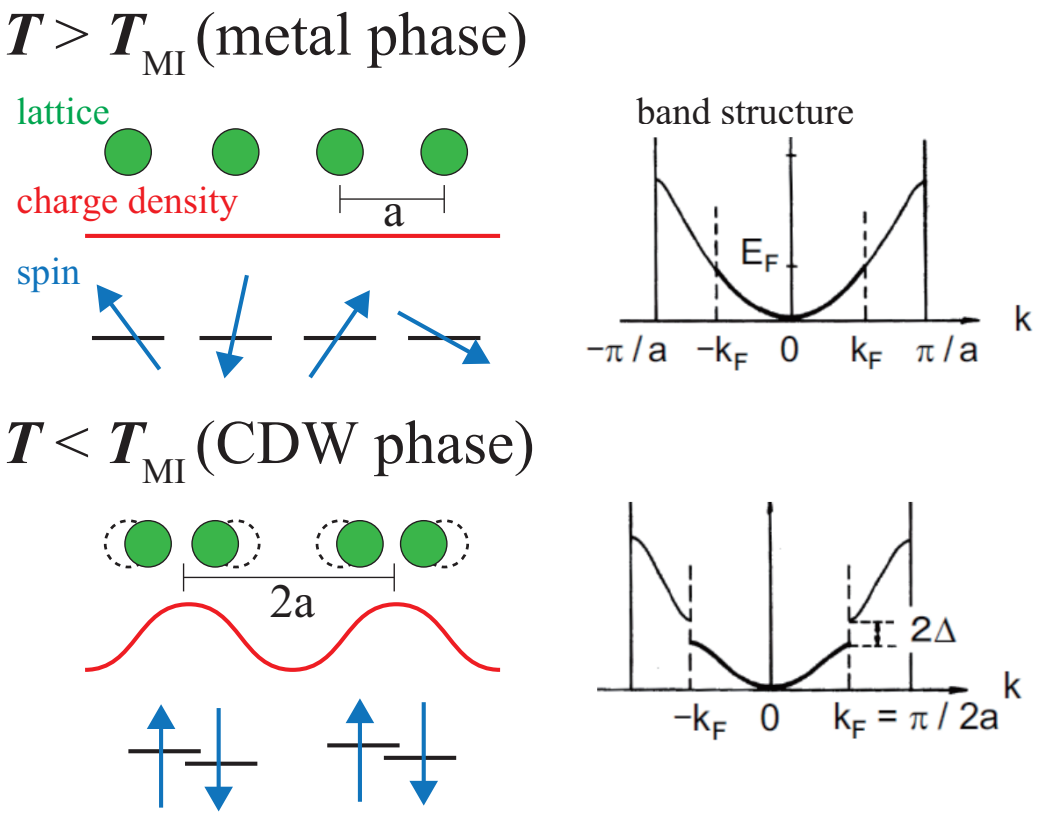

Figure 1.1: Schematic view of Peierls transition.[3] (upper): Metallic phase at high temperature region. The system has a lattice constant a and a uniform charge density. Magnetically, the system is in paramagnetic (or non-magnetic) state. (lower): Insulating 2-k_{F} CDW phase at low temperature region. A superlattice with a lattice constant of $2a$ forms, so that the charge density forms a standing wave (CDW state). Through spin-lattice interactions, spin-singlet ground states can be realized (e.g. spin Peierls transition).

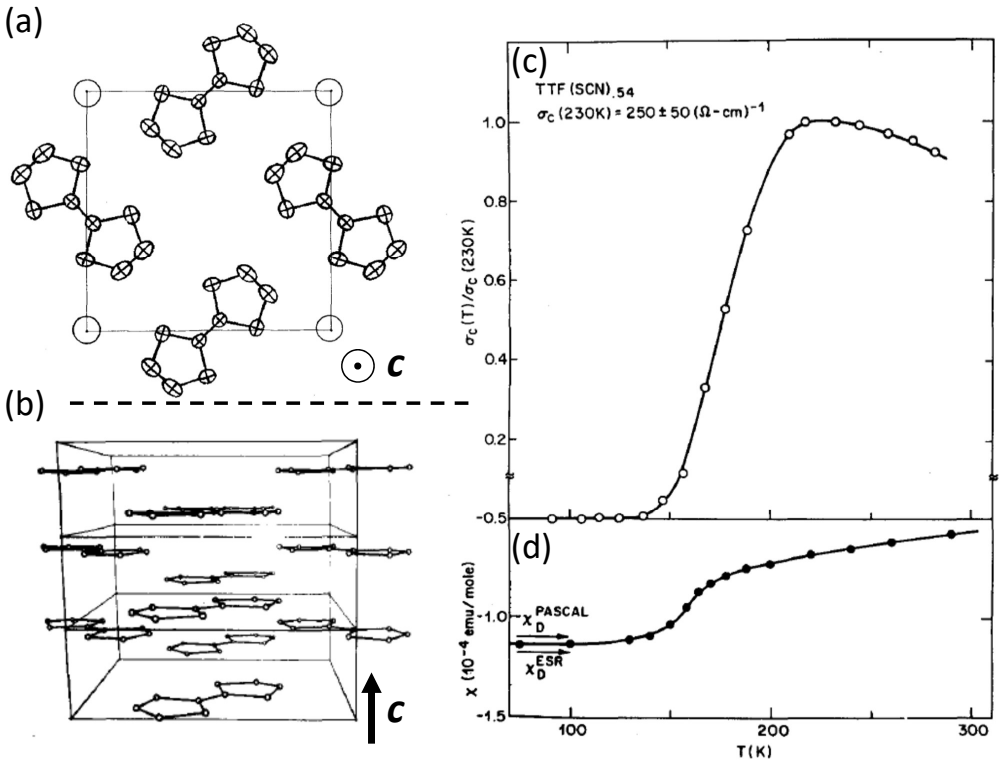

Figure 1.2: (a,b) Crystal structure of $TTF(SCN)_{0.54}$.[5] TTF molecules are arranged in a-b plane and stacked along the c-axis. Temperature dependence of (c) electric conductivity ratio $\sigma_c(T)/\sigma_c(230K)$ and (d) magnetic susceptibility.[5] The sharp drop in electric conductivity with decreasing temperature corresponds Peierls transition. A drop in magnetic susceptibility also observed in a similar temperature region to Peierls transition. This is due to the change in density of states caused by the Peierls transition, which is different from the spin-Peierls transition.

1.1.2 Mott transition

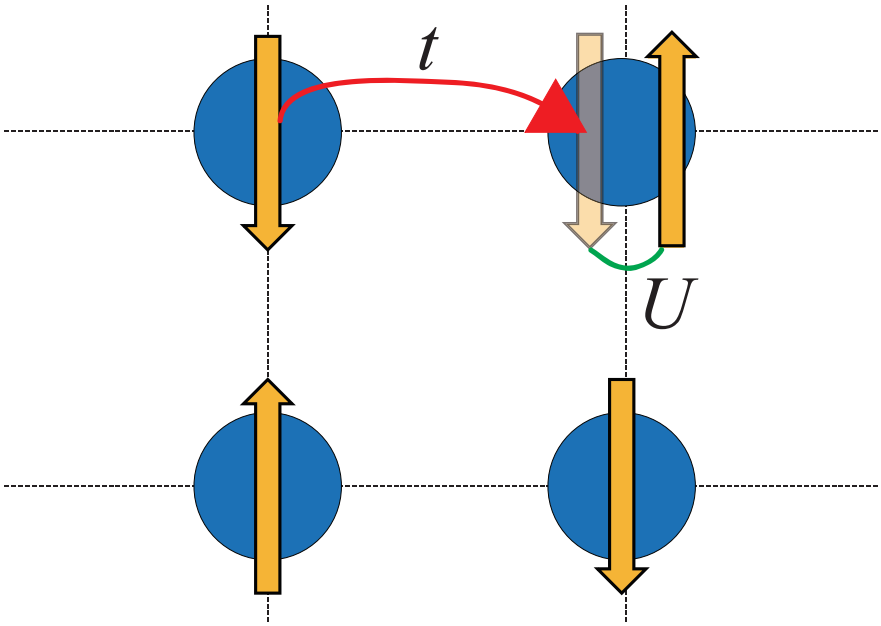

Figure 1.3: Schematic view of the Mott transition mechanism by using the Hubbard model. A material with half-filled conduction band becomes an insulator due to strong Coulomb repulsion between conduction electrons (see main text).

The Mott transition is one of the most important physical phenomena in strongly correlated electron systems. The Mott transition is well understood by the Hubbard model given by

$$\mathcal{H} = -t \sum_{<i,j>,\sigma} (c^{\dagger}_{i,\sigma} c_{j,\sigma} + h.c.) + U \sum_{i} n_{i,\uparrow} n_{i,\downarrow} \tag{1.1}$$

When $U \ll t$, a metallic state is realized, and each atom can be occupied by two electrons, an up-spin and a down-spin. In contrast when $U \gg t$, conduction electrons are localized by Coulomb repulsion and the system becomes an insulator. In other words, electrons lose the charge degree of freedom and only possess the spin degree of freedom. The driving force of the Mott transition is spin fluctuation, and the localized spin often exhibits anti-ferro magnetic order. In the Mott insulator such as copper oxides, many peculiar phenomena like high-T_C superconductivity have been found. Since band-filling can be easily controlled by an external field or a substitution of different ions, Mott insulators are suitable research targets for strongly correlated electron systems. In the Mott transition, single-band electron plays an important role in two properties: transport and magnetism. $BaVS_3$ described later differs in this point because electrons in different orbitals carry magnetism and conduction, respectively.

1.1.3 Kondo effect

We note physical properties of the Kondo-lattice system, one of the typical strongly correlated electron systems.[6, 7] The Hamiltonian is given by the interaction $J_{\rm cd}$, caused by hybridization between conduction (itinerant) electrons and localized magnetic moment of $3d$ ($4f$) electron (c-$d(f)$ hybridization).

$$H_{\rm cd} = J_{\rm cd}\frac{1}{2N_0}\sum_{kk'}[(c^\dagger_{{\rm k}'\uparrow}c_{{\rm k}\uparrow} - c^\dagger_{{\rm k}'\downarrow}c_{{\rm k}\downarrow})S_{\rm z} + c^\dagger_{{\rm k}'\downarrow}c_{{\rm k}\uparrow}S_+ + c^\dagger_{{\rm k}'\uparrow}c_{{\rm k}\downarrow}S_-], \tag{1.2}$$

$$J_{\rm cd} = 2 < |V|^2 > \left(\frac{1}{E_{\rm d} + U - \epsilon_{\rm F}} + \frac{1}{\epsilon_{\rm F} - E_{\rm d}}\right), \tag{1.3}$$

where V is a matrix element of c-d hybridization, $E_{\rm d}$ means the energy of d-electron with reference to the center of conduction band, U shows on-site Coulomb interaction between d electrons, $\epsilon_{\rm F}$ represents the Fermi energy, and $S_{\rm z}, S_+, S_-$ are spin operators of d electrons, as follows;

$$S_{\rm z} = \frac{1}{2}(d^\dagger_\uparrow d_\uparrow - d^\dagger_\downarrow d_\downarrow), \tag{1.4}$$

$$S_+ = d^\dagger_\uparrow d_\downarrow, \tag{1.5}$$

$$S_- = d^\dagger_\downarrow d_\uparrow. \tag{1.6}$$

Now, the scaling equation is written as follows depending on the bandwidth W and the density of states $D_{\rm c}(\epsilon)$.

$$\frac{dJ_{\rm cf}}{dW} = -\frac{D_{\rm c}(\epsilon_{\rm F})}{W}J^2_{\rm cf}. \tag{1.7}$$

Under the strong coupling condition $W \Rightarrow 0$, $J_{\rm cf}$ becomes divergent, so that the localized spin can be ignored. Since the effective mass is given by $m^* = h^2/W$, a Fermi liquid state with a heavy effective mass is realized in low temperature and weak magnetic field region. When hybridization is sufficiently large, a MI transition occurs at $T_{\rm K}$.

Focusing on magnetism, the Kondo effect forms a Kondo-singlet between the localized moment and conduction electrons. This singlet can be eliminated by a magnetic field, and a metamagnetic transition, in which the magnetization rapidly increases, is expected.

The Kondo effect is an universal phenomenon in magnetic impurity model, and many studies have been carried out on f electron compounds. As a typical example, the electric resistivity of SmB_6 is shown in Fig. 1.4. [8] The energy gap due to the Kondo effect is sensitive to the external field such as magnetic fields and/or high pressure. In the case of SmB_6, the gap decreases with applying pressure, and the metallic state is stabilized at pressure of about 40 kbar.

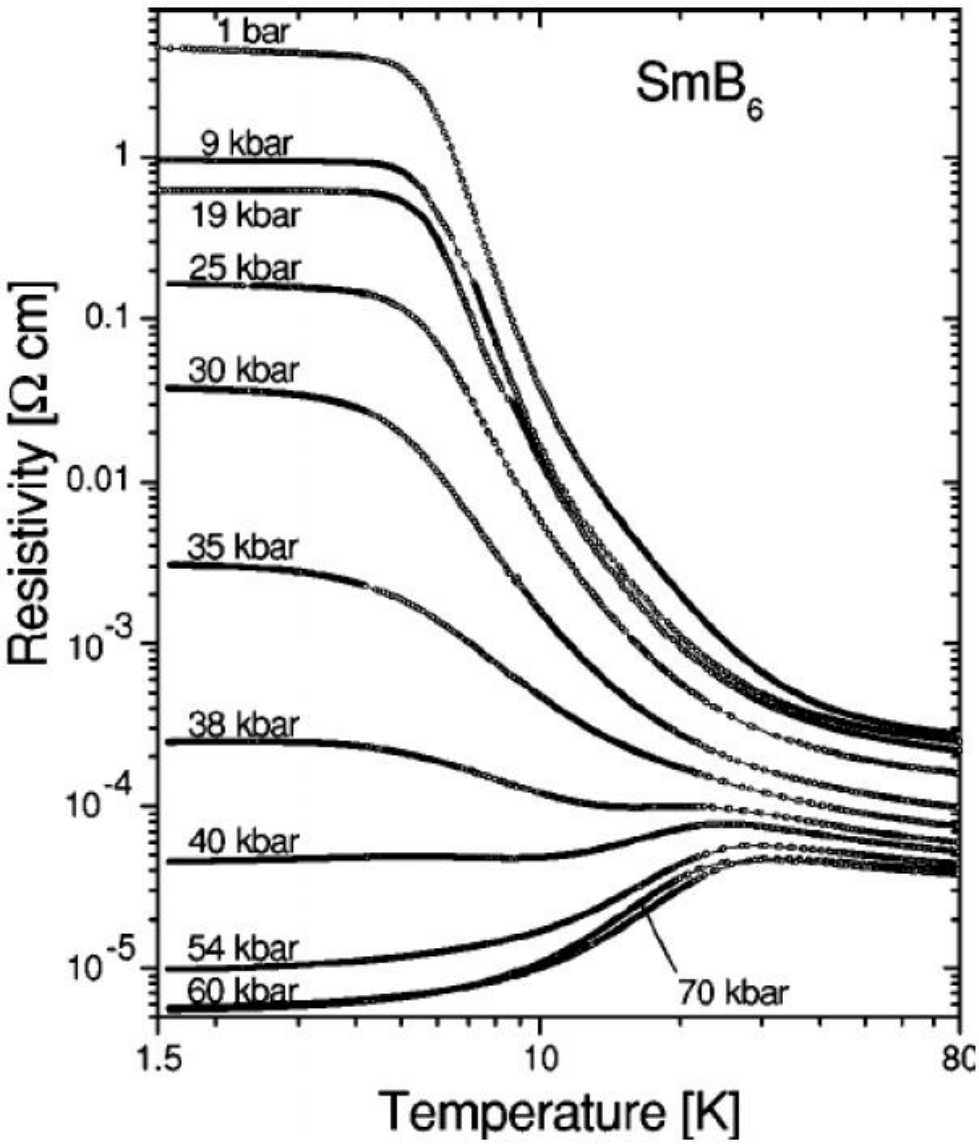

Figure 1.4: Temperature dependences of the electric resistivity of SmB_6 under several pressures.[8] The resistivity becomes metallic down to 1.5 K at pressure of 40 kbar.

1.2 Previous studies of $BaVS_3$

In this section, we describe the previous studies that are important for understanding the physical properties of $BaVS_3$.

$BaVS_3$ was first synthesized by Gardner *et al.* in 1969. [13] At this time, high quality single crystals could not be obtained and thus researchers mainly performed experiments using sintered samples. $BaVS_3$ was regarded as a quasi-one-dimensional conductor.

In 1995, Kuriyaki *et al.* successfully synthesized high quality single crystals by using the tellurium flux method. [14] From then researchers obtained sufficiently high quality data using single crystal samples. In 2000, Mihály *et al.* re-evaluated magnetic susceptibility and electric conductivity under ambient pressure, [15] and then interpretation of the nature of $BaVS_3$ shifted from one-dimensional conductor to the Mott-Hubbard insulator including two-dimensional geometrical frustration. Since no structural phase transition had been observed at T_{MI} at that time, the MI transition in $BaVS_3$ was considered to be a pure Mott transition, and discussion such as orbital order was actively made.

However, in 2007, T. Inami *et al.* revealed by their synchrotron radiation experiment that this MI transition was accompanied by a $Q = 2k_{\mathrm{F}}$ superlattice formation. [16] Most of the above results were re-examined, and it was almost ascertained that the driving force of the MI transition in $BaVS_3$ is Peierls instability.

This interpretation continues to this day, but hardly reproduces the magnetism, especially for metamagnetic transitions that occur below T_{MI}.

1.2.1 Structure and band calculation

First of all, we show the crystal structure of $BaVS_3$ at room temperature in Fig. 1.5.. [13, 16, 17, 18] The hexagonal perovskite-type structure ($P6_3/mmc$) includes face-sharing VS_6 octahedral chains along the c axis, resulting in one-dimensional structure. V ions form a triangular lattice in the ab plane. Structural transition to the orthorhombic phase ($CmC2_1$) with zigzag deformation of the VS_6 chain occurs at $T_s \sim$ 240 K.[13, 17, 18] This structural phase transition is mainly caused by the Jahn-Teller distortion, and the degeneracy of the $3d$ orbital is partially released. This crystal field splitting maintains down to the low temperatures and is the basis for determining low temperature magnetic properties. Note that at T_s, a small anomaly is seen in the electric resistivity (as shown in Fig. 1.13), but not in the magnetic susceptibility (in Fig. 1.18).[15] Therefore, from room temperature to low temperature, the magnetism of this material should be understood by one uniform model.

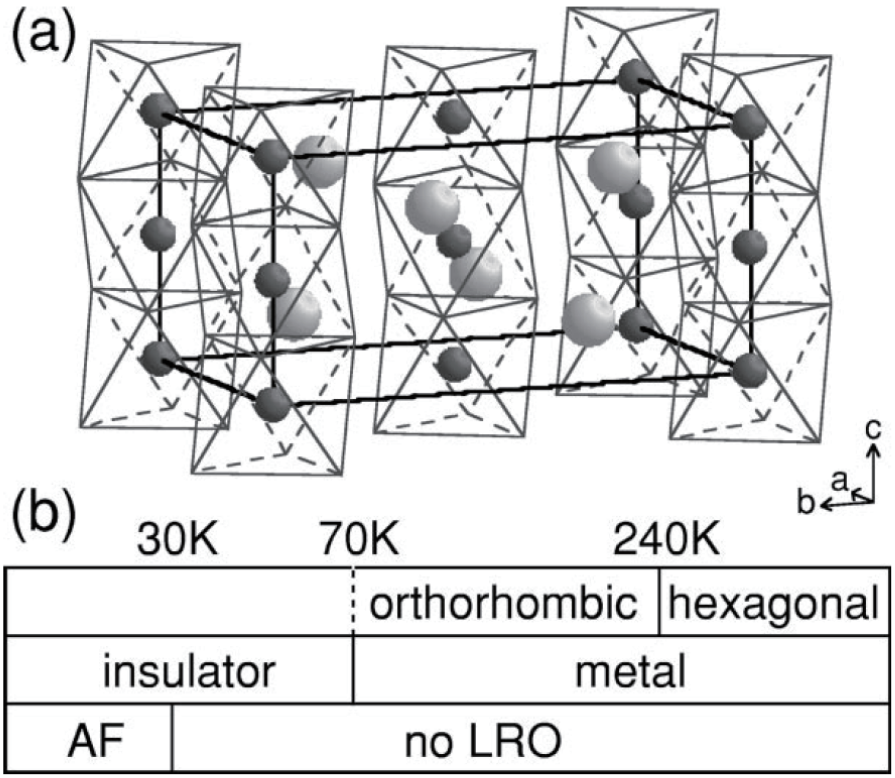

Figure 1.5: (a) Crystal structure of $BaVS_3$ at 100 K. [16, 17, 18] The small circle represents the atomic position of vanadium, and the large circle shows the atomic position of barium. Sulfur is located at the vertex of the octahedron. (b) Crystal structural, electric and magnetic characters of $BaVS_3$ chagne with temperature.

For the conventional localized model, we draw the crystal field splitting of vanadium $3d$ levels in Fig. 1.6. At room temperature, considering the effect of the VS_6 octahedral chain, the $3d$ orbitals split into doubly degenerate e_g orbital, A_{1g} orbital (d_{z^2} orbital), and doublly degenerate E_g orbitals ($e_{t_{2g}}$ orbitals). The latter two orbitals originate from the t_{2g} orbital. The A_{1g} orbital is parallel to VS_6 chain, and the E_g orbitals are almost perpendicular to the chain. Below T_S, E_g orbitals are slightly degenerate and form E_{g1} and E_{g2} orbitals due to the orthohombic deformation.[19]

Next, we discuss the band structure[20]. The Wannier function of the t_{2g} orbitals are shown in Fig. 1.7. The A_{1g} orbital extends along the direction of neighbor vanadium ions in the chain, and hopping transfer is possible along the c-axis. In contrast, the E_g orbital extends along the sulfur direction of the octahedron, and it hybridizes with the S($3p$) orbital. The density of state calculated by the local density approximation(LDA) in Fig. 1.8 can be understood in the almost same way as the localized model described above. However, from the calculations based on LDA + dynamic mean field theory (DMFT), it is clear that the localization model is not sufficient, and considering itinerant model with hybridization between bands is necessary.

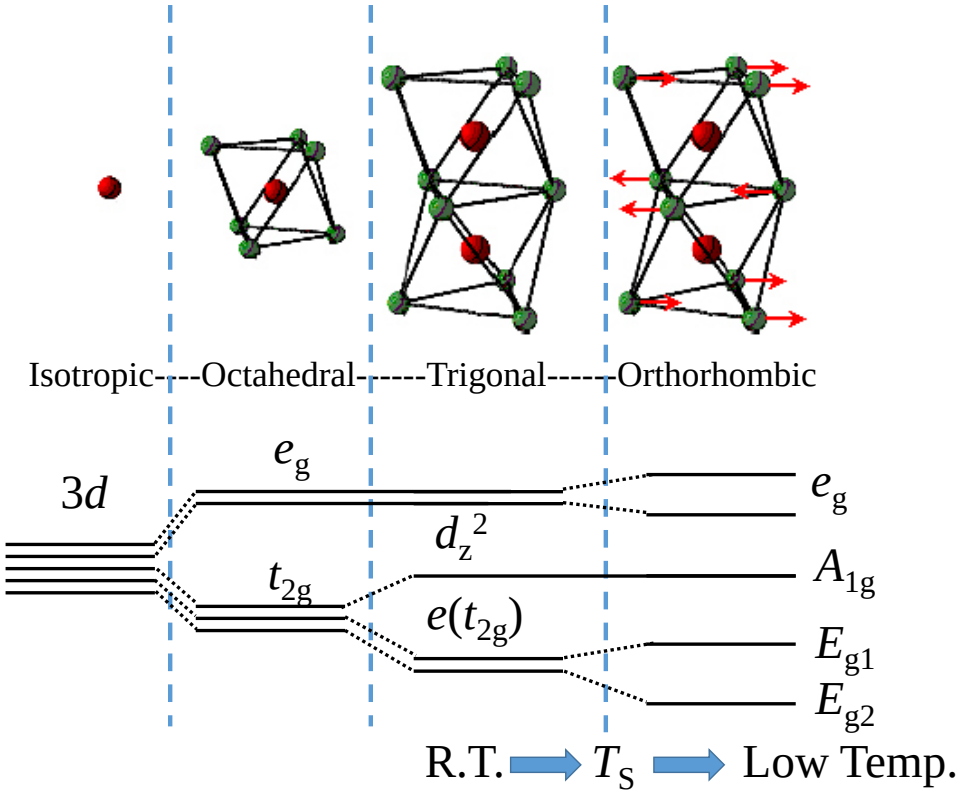

Figure 1.6: Level splitting of $3d^1$ electron by the crystal field. The $P6_3/mmc$ structure at room temperature has the trigonal crystal field effect for V sites, and the $Cm2_1$ structure below 240 K has the orthorhombic crystal field effect for V sites.[19]

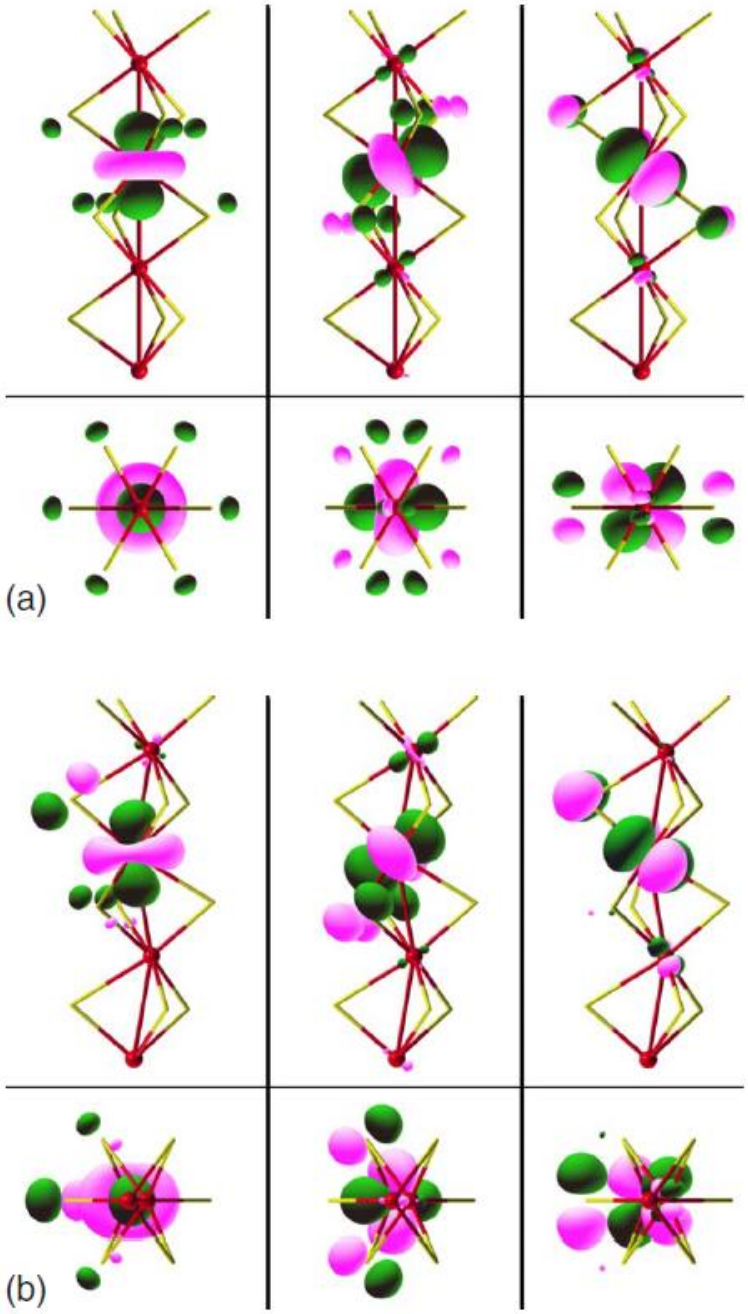

Figure 1.7: t_{2g} Wannier functions for $BaVS_3$ in the crystal field at (a) $T>T_S$ and (b)$T<T_S$. [20] Broad A_{1g} orbital (left), narrow E_{g1} orbital (center) and narrow E_{g2} orbital (right) viewed from *ab* plane (upper) and *c* axis (lower).

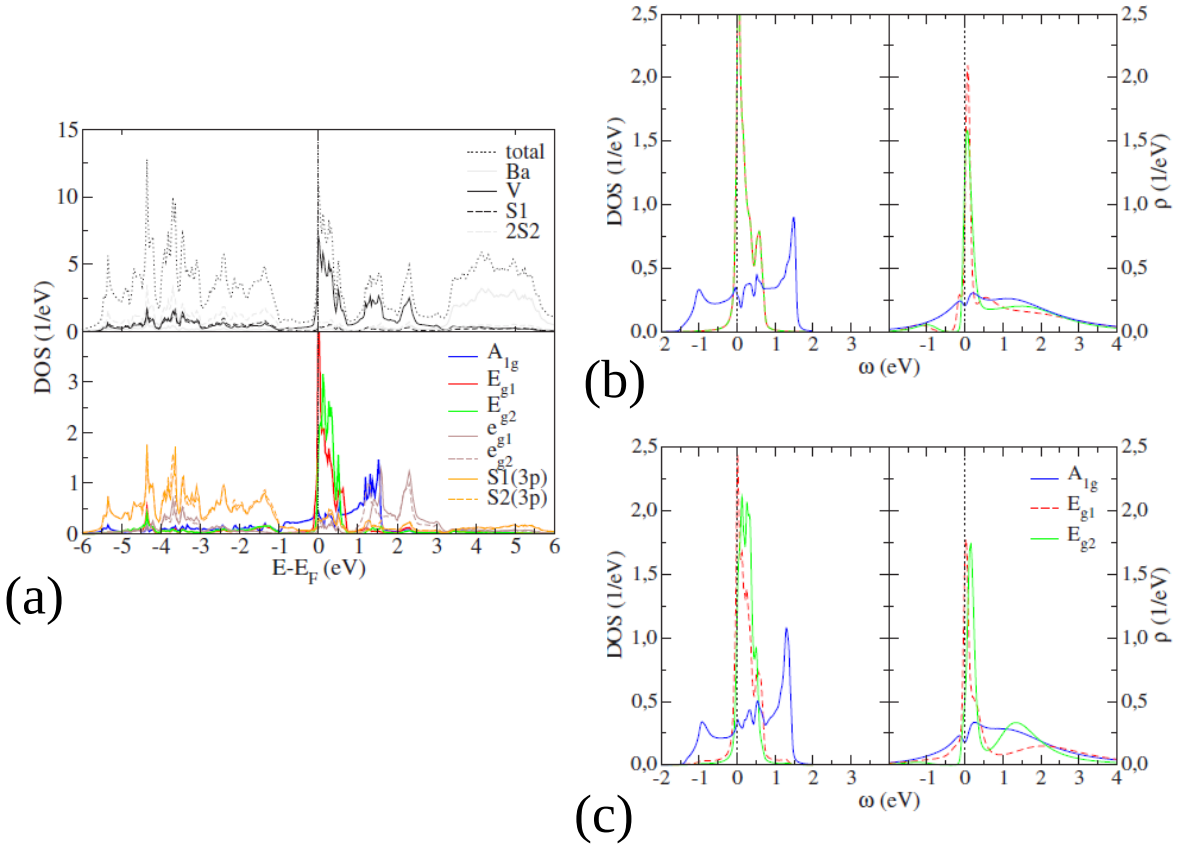

Figure 1.8: (a) Density of state (DOS) calculated by LDA. [20] The Fermi surface is mainly composed of A_{1g} and nearly double degenerate E_g orbitals. (b-c) Local spectral functions from LDA+DMFT (right) in comparison to the local LDA DOS for the t_{2g} Wannier function (left) in the crystal-field basis for (b) $P6_3/mmc$ and (c) $Cm2_1$ structure. Reconstruction of the Fermi surface due to the strong electron-electron interaction occurs even at room temperature ($P6_3/mmc$ structure) and enhanced below T_s ($Cm2_1$ structure)

Let's return to the crystal structure. When decreasing the temperature from room temperature, the one-dimensional instability along the c-axis direction starts to increase at around 170 K based on the analysis of half-width of half-maximum (HWHM) of the diffuse scattering at (-1 4 -2.5) Bragg position. [21] This fluctuation can be regarded as a precursor phenomenon of the CDW formation, which will be described later. Sato *et al.* confirmed that an incoherent gap starts to form in the d_{z^2} orbital around 120 K by the Angle-resolved photo-emission spectroscopy (ARPES) measurement. [22]

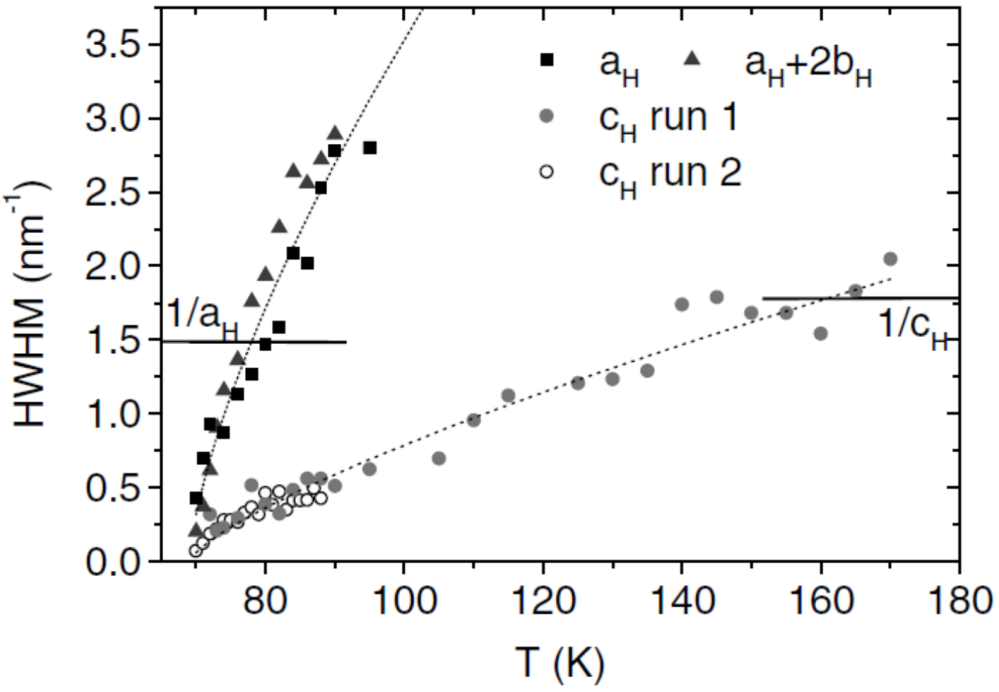

Figure 1.9: Temperature dependence of the half-width of the half-maximum HWHM of the (-1 4 -2.5) defuse scattering peak along a_H,$a_H + 2b_H$, and c_H directions. [21] a_H, b_H, and c_H represent the hexagonal unit cell directions. In the temperature region where HWHM is smaller than $1/a_H$ $(1/c_H)$, the incoherent CDW gap grows in the $a(c)$-axis direction.

From the synchrotron radiation XRD results, [16] it is clear that a superlattice formation occurs along the c-axis at T_{MI} ∼70K with coherent CDW formation, as shown in Fig. 1.10.

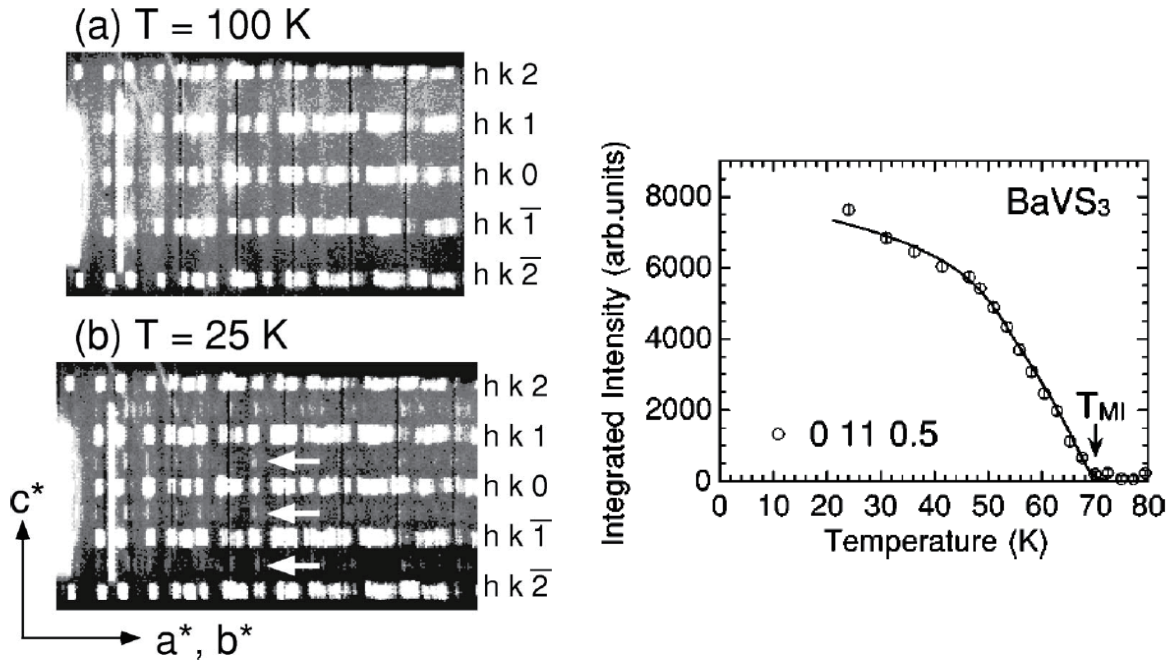

Figure 1.10: (a,b) Oscillation photographs of $BaVS_3$.[16] (a) At 100 K (above T_{MI}). The white points are fundamental Bragg reflections hkl, and are classified by l. (b) At 25 K (above T_{MI}). Super lattice reflections are observed on $l = n + \frac{1}{2}$ line, shown by arrows. (c) Temperature dependence of integrated intensity of the superlattice reflection 0 11 $\frac{1}{2}$. The intensity decreases with increasing temperature, and disappear at $T_{\mathrm{MI}} \sim 70$ K.

Since this CDW formation is caused by a Peierls transition due to structural fluctuations, [21] it is expected that the application of hydrostatic pressure will reduce the one-dimensionality and suppress the CDW formation. Actually, from the XRD measurements under high pressure[23] shown in Fig. 1.11, $BaVS_3$ does not show a structural phase transition below T_{MI} and 1.8 GPa , which is the critical pressure of MI transition on their experimental environment, and the CDW completely deformed above critical pressure.

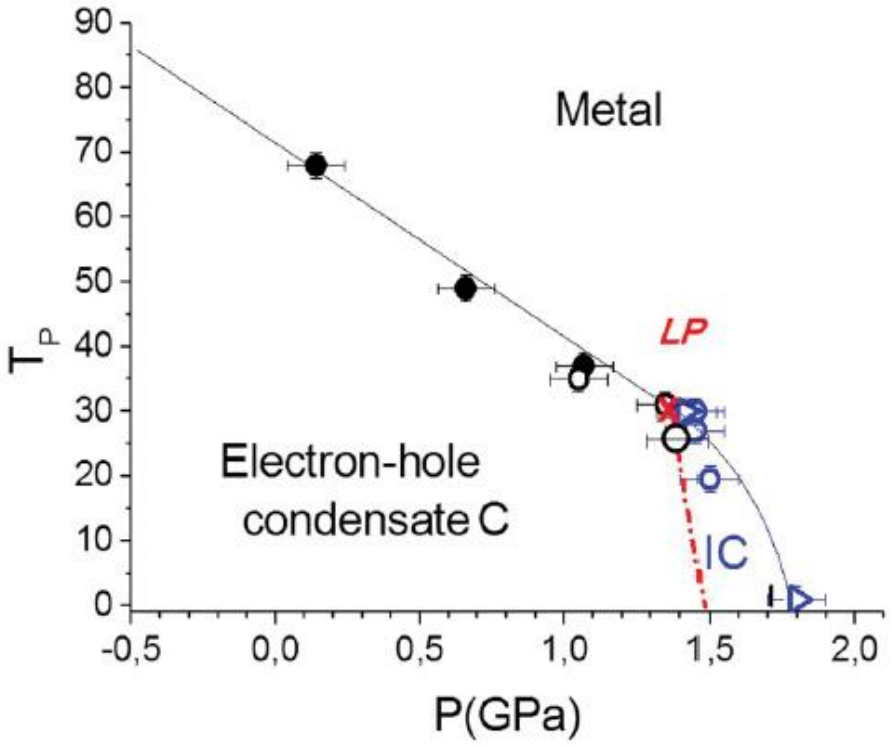

Figure 1.11: Temperature-Pressure phase diagram of $BaVS_3$ constructed by the superlattice formation temperature T_{P}, we consider which is equal to T_{MI}.[23] C and IC phases represent commensurate CDW and in-commensurate CDW state, respectively. The LP shown in figure means the possible location of Lifshitz point, the triple critical point of Metal, C and IC states.

1.2.2 Transport and thermal properties

First of all, we should note that in spite of the structural one-dimensionality, macroscopic properties of $BaVS_3$ (mentioned below) are almost isotropic. [15] So we will not mention about anisotropy unless it becomes particularly important.

The magnetic specific heat is evaluated by subtracting the specific heat of nonmagnetic $BaTiS_3$ as the contribution of the lattice as shown in Fig. 1.12(a, b) .[24] The broad peak at 150 K in Fig. 1.12 (b) can be understood by the evolution of structural fluctuations, which is not appear in non-MI transition compound $BaTiS_3$. A sharp peak is observed at $T_{\rm MI}$. Most importantly, a linear component with Sommerfeld constant$\gamma \sim 15.7\,{\rm mJ/K^2\,mole\,V}$ exists in the specific heat even in a low-temperature insulating state of $BaVS_3$, suggesting that heavy quasi-particles near the Fermi surface exist.

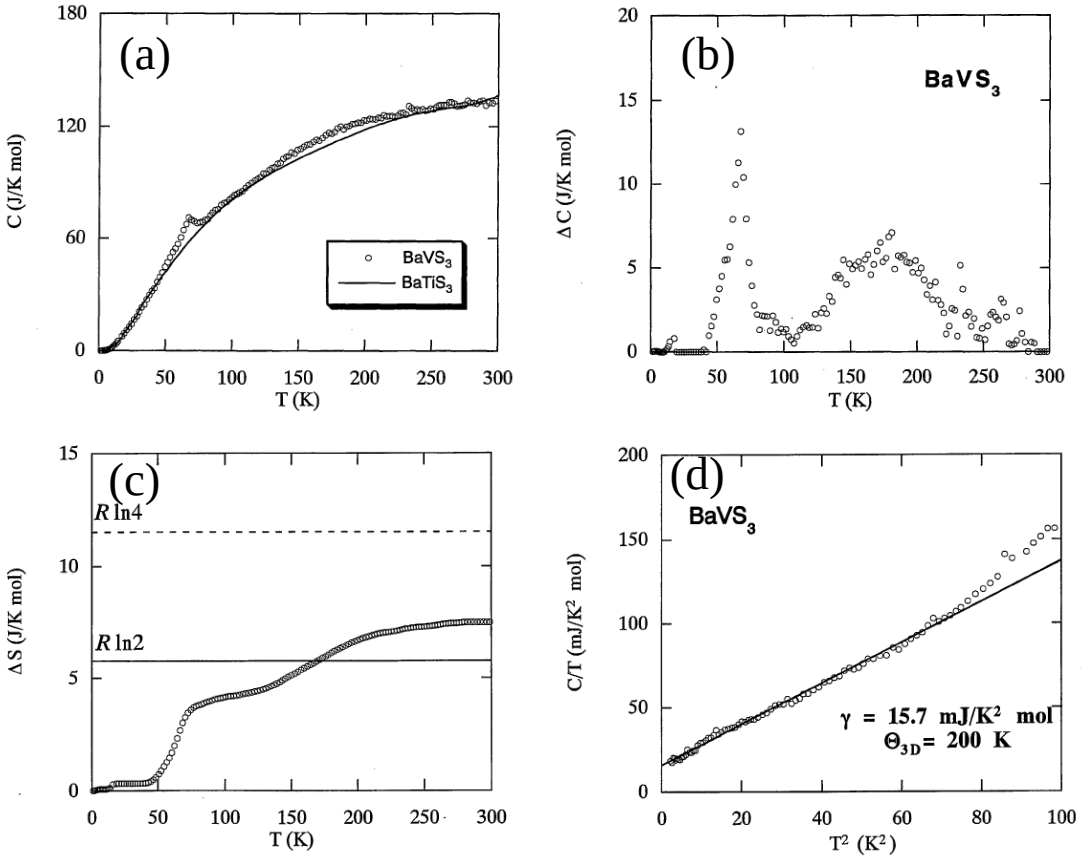

Figure 1.12: (a)Temperature dependence of specific heat of $BaVS_3$ and $BaTiS_3$.[24] (b) Evaluated magnetic specific heat of $BaVS_3$. The lattice contribution is estimated by the specific heat of nonmagnetic $BaTiS_3$. (c) Calculated magnetic entropy ΔS. The entropy consumption of 4.7 J/K mol at the peak at $T_{\rm MI}$ is not good agreement with $R{\rm ln}2 = 5.76$ J/K mol. (d) T-linear and T^3 component in specific heat in the low temperature region with the Sommerfeld constant$\gamma \sim 15.7\ {\rm mJ/K^2\,mole\,V}$.

As shown in Fig. 1.13, the electric resistivity at ambient pressure and above 150 K is metallic ($\mathrm{d}\rho/\mathrm{d}T > 0$) in high quality $BaVS_3$.[15] (Note that in sulfur deficient $BaVS_3$, the electric resistivity behaves as insulator in hall temperature range. See Appendix in detail.) Below 150 K, the electric resistivity turn to behave as semiconductor ($\mathrm{d}\rho/\mathrm{d}T < 0$). Then, metallic resistivity largely increases with the maximum in $\mathrm{d}\rho/\mathrm{d}(1/T)$ at $T_{\mathrm{MI}} \sim 70$ K, and undergoes the MI transition with formation of a charge gap. By applying the hydrostatic pressure[25, 26], the electric resistivity decreases and T_{MI} shifts to the low temperature side (see Fig. 1.14). Under the pressure of $p_{\mathrm{cr}} \sim 2.0$ GPa, the MI transition is completely suppressed, and a non-Fermi liquid state is realized, which is thought to be derived from the quantum critical point of anti-ferromagnetic spin fluctuation. From these results, the phase diagram was obtained as in Fig. 1.15 .

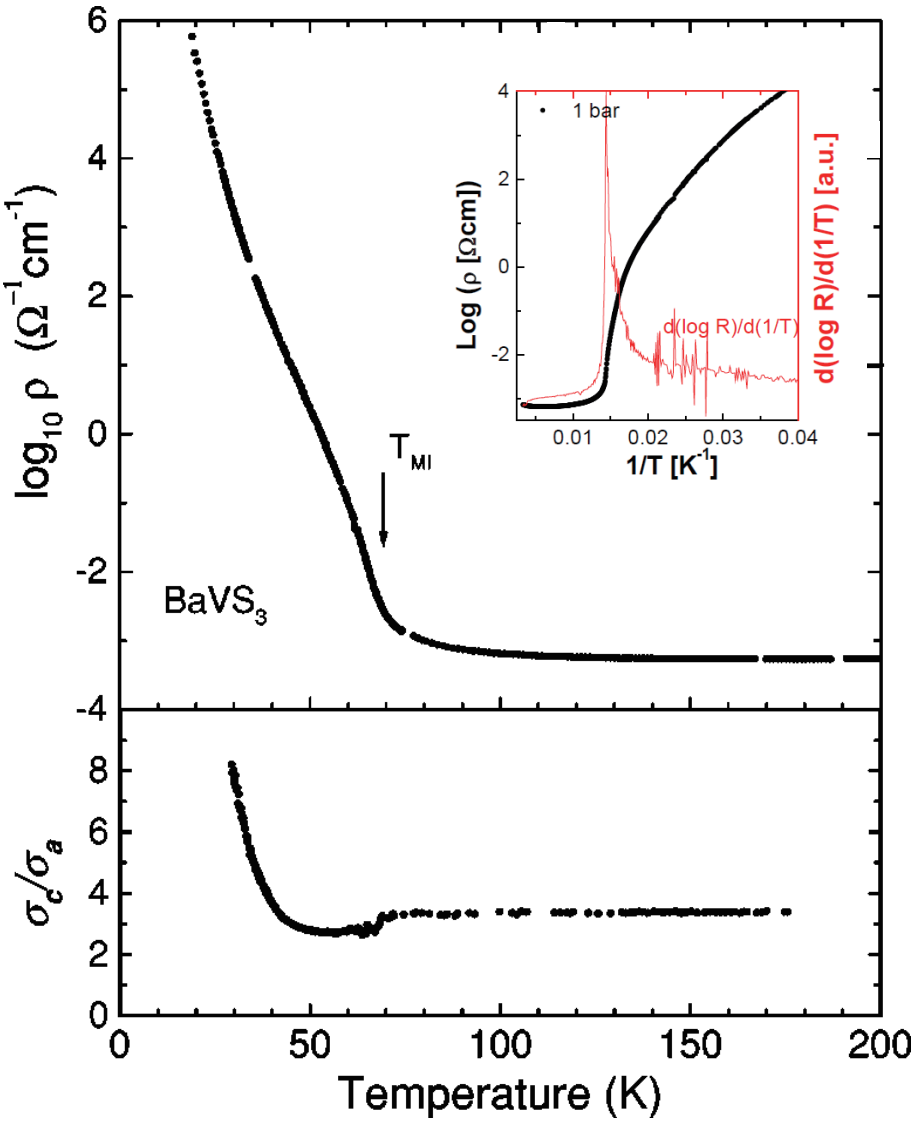

Figure 1.13: (upper): Temperature dependence of electric resistivity at ambient pressure.[15, 26] The arrow indicates the MI transition temperature, defined as peak temperature in d(log$R$)/d(1/T) (inset). (lower): Temperature dependence of the conduction anisotropy σ_c / σ_a in $BaVS_3$.[15] The conduction anisotropy is as small as 3.7 above 40 K, and below 40 K it increases with decreasing temperature.

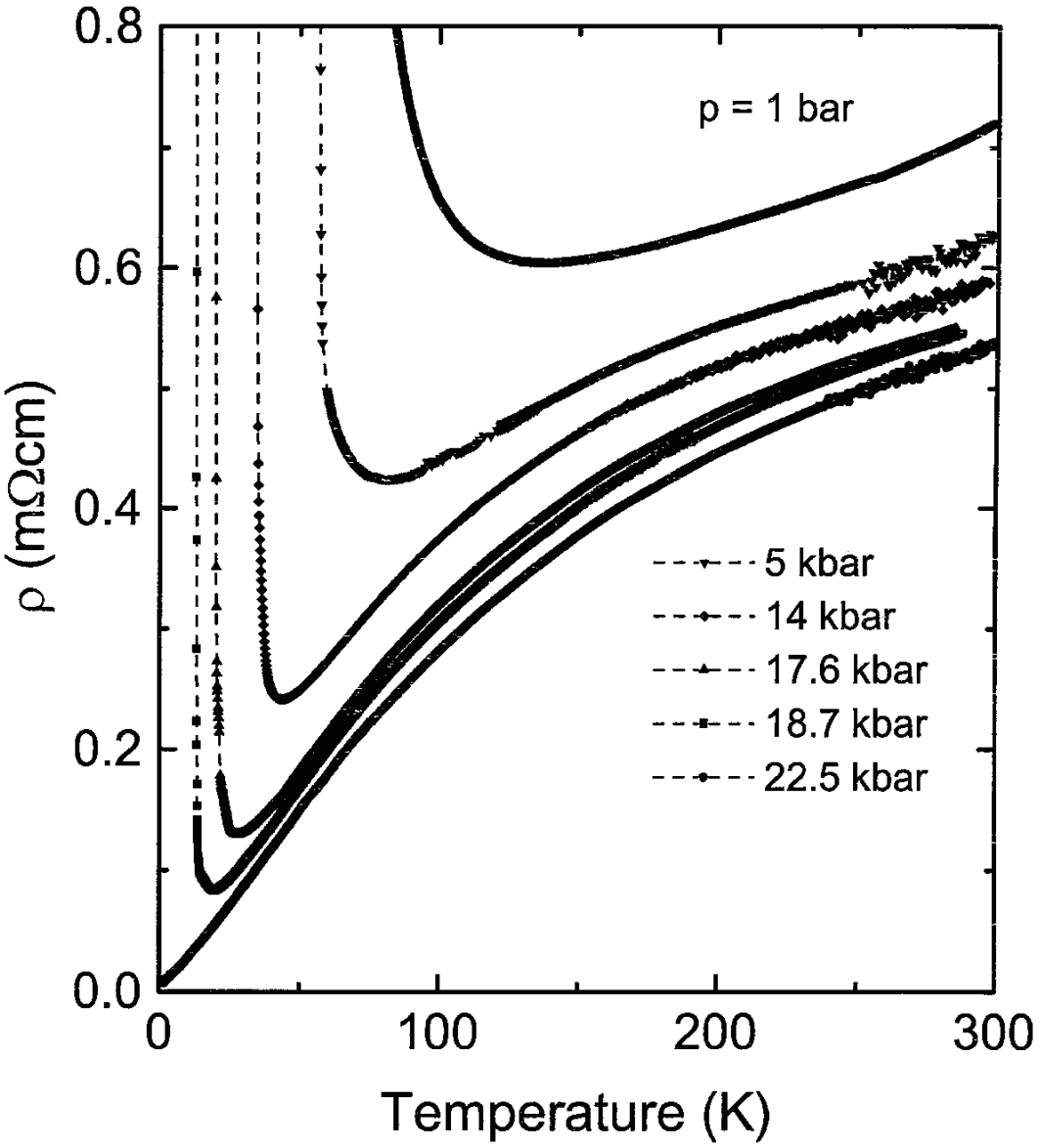

Figure 1.14: Temperature dependences of electric resistivity of $BaVS_3$ under designated pressure.[25, 26] The electric resistivity decrease with applying pressure. T_{MI} was suppressed with applying pressure and not observed at 22.5 kbar.

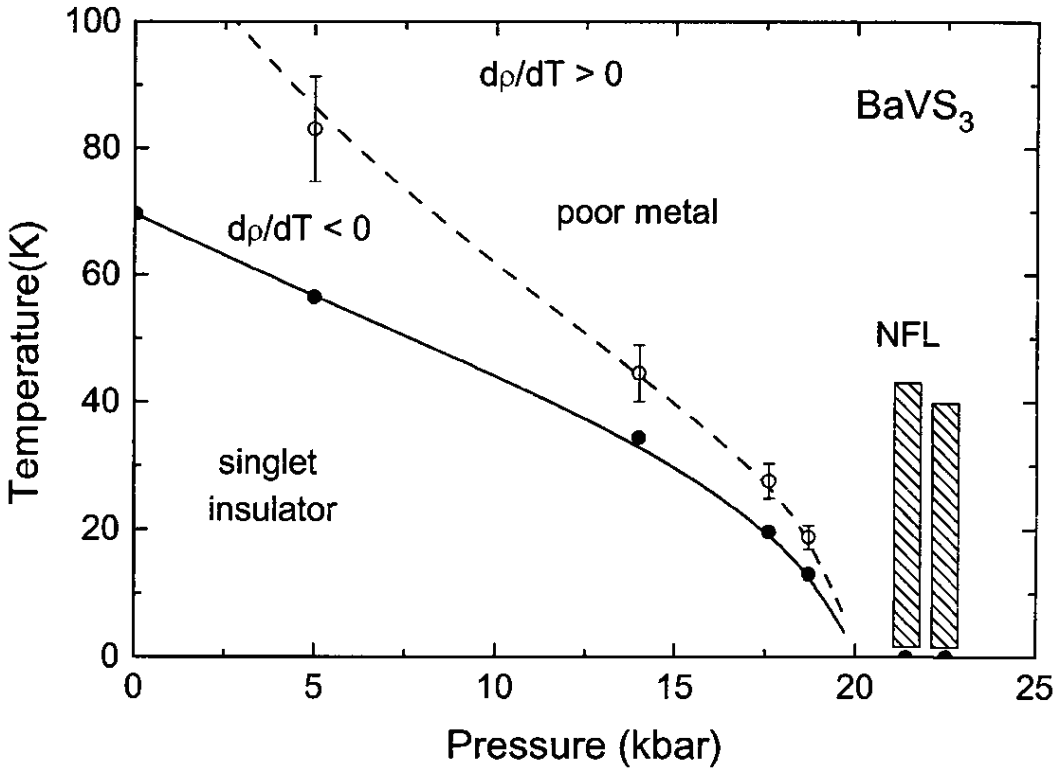

Figure 1.15: Pressure-Temperature (p-T) phase diagram of $BaVS_3$ determined by electric resistivity measurements.[25] Dashed line is the temperature at $(\mathrm{d}\rho/\mathrm{d}T = 0)$, solid line represents T_{MI} defined as peak temperature in $\mathrm{d}(\log\rho)/\mathrm{d}(1/T)$. NFL means the non-Fermi liquid region with $(\rho \propto A \times T^n, n \sim 1.25 - 1.5)$.

1.95 GPa, At a pressure slightly lower than p_{cr} (2.0 GPa), the MI transition is suppressed and the metallic state is maintained down to 2.0 K by applying magnetic field of 12 T.[26] This suggests that the gap formation associated with the MI transition is related to (antiferro-magnetic) spin fluctuations, which is affected by the magnetic field. This implies an existence of coupling between magnetism and transport phenomena, thus we are interested in the details of magnetism.

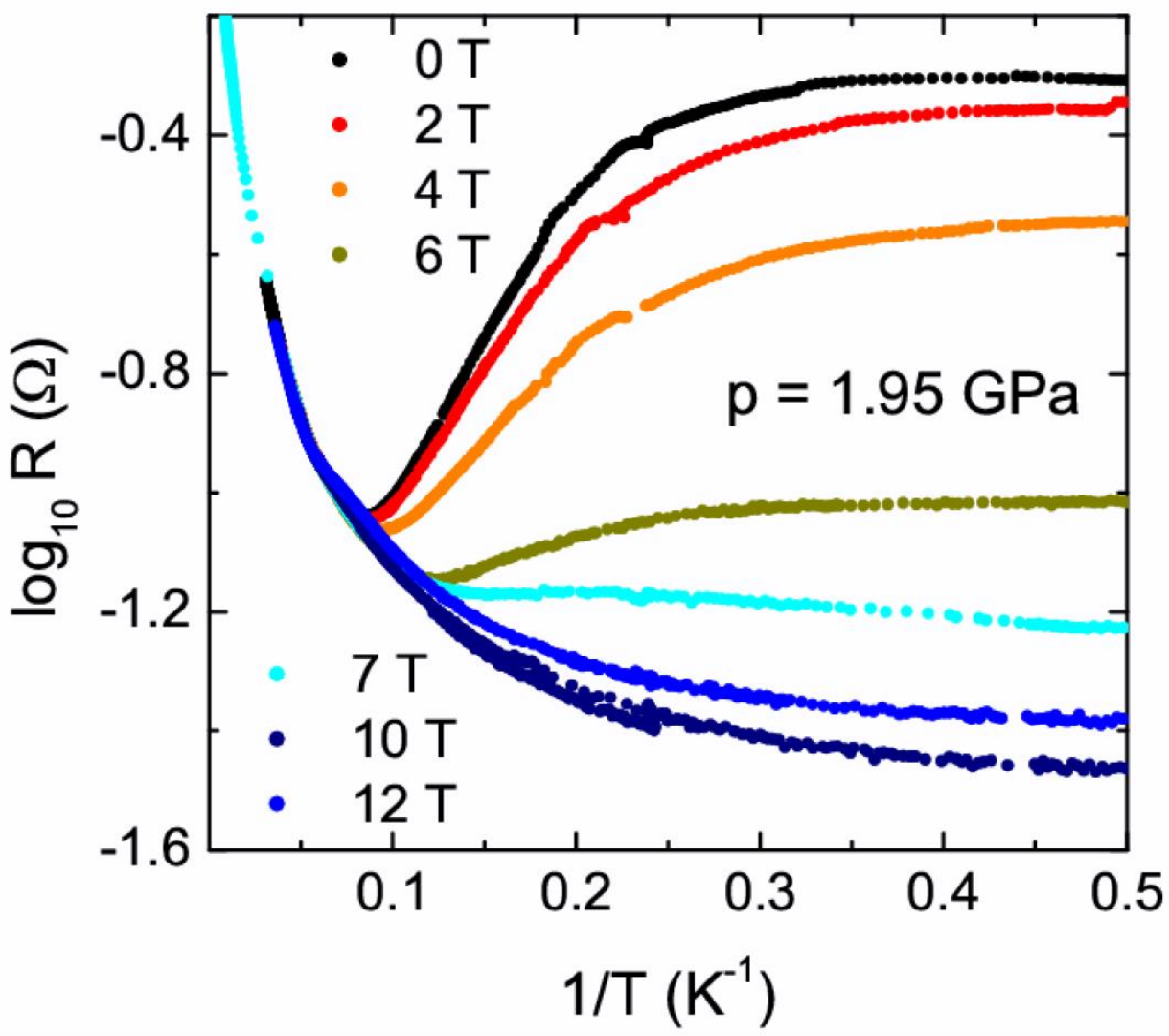

Figure 1.16: Temperature dependences of magneto-resistance at 1.95 GPa,[26] slightly below p_{cr} (2.0 GPa). By applying a magnetic field, the electric resistance gradually approaches that of a high-temperature metallic state, and the MI transition is suppressed in a magnetic field of 12 T. Interestingly, T_{MI} of 16 K hardly changes with applying a magnetic field below 10 T and disappear at 12 T.

1.2.3 Preliminary electric resistivity measurement

We measured the electric resistivity using a single crystal sample and a diamond anvil pressure cell. The purpose of this experiment was to determine the typical target pressure of our magnetization measurement under pressure. Figure 1.17 shows the temperature dependence of the electric resistance under designated pressure (upper panel).The MI transition similar to that of the previous study [15] was observed, and at the pressure of about 1.0 GPa, the temperature dependence of electric resistivity at low temperatures shows metallic behavior. The lower panel of Fig. 1.17 shows the magneto-resistance. We found that the magneto-resistance at 1.0 GPa shows a positive magneto-resistance, which is significantly different from other pressure regions except around B_{M} at ambient pressure and 20 K. For this reason, we decide to conduct the magnetization measurement in the pressure region of especially around 1.0 GPa.

1.2.4 Magnetism under ambient pressure

The temperature dependence of magnetic susceptibility of $BaVS_3$[15] is shown in Fig. 1.18. It has been considered so far that the magnetic susceptibility in paramagnetic region above T_{MI} χ obeys the Curie-Weiss law with localized spin S =1/2 at every other V ions[21] and the Weiss temperature $\Theta_{\mathrm{W}} \sim 9$ K. [27] Magnetic susceptibility shows a spin-Peierls-like transition at T_{MI}, where magnetic moments forms incomplete- singlet dimers. Then, the susceptibility gradually decreases and shows an anomaly at T_{x} = 30 K, which corresponds to an incommensurate magnetic ordering with the evaluated ordered moment of 0.5 μ_{B}/f.u. determined by neutron diffraction measurement[28] as shown in Fig. 1.19. Resonant soft X-ray diffraction measurement clarified that the magnetic order is a type of co-linear anti-ferro magnetic order, $T_{\mathrm{x}} = T_{\mathrm{N}}$.[29] We must note that this anti-ferro magnetism is easy to destructed by sulfur deficient and turns to ferro- magnetism (see Appendix in detail).

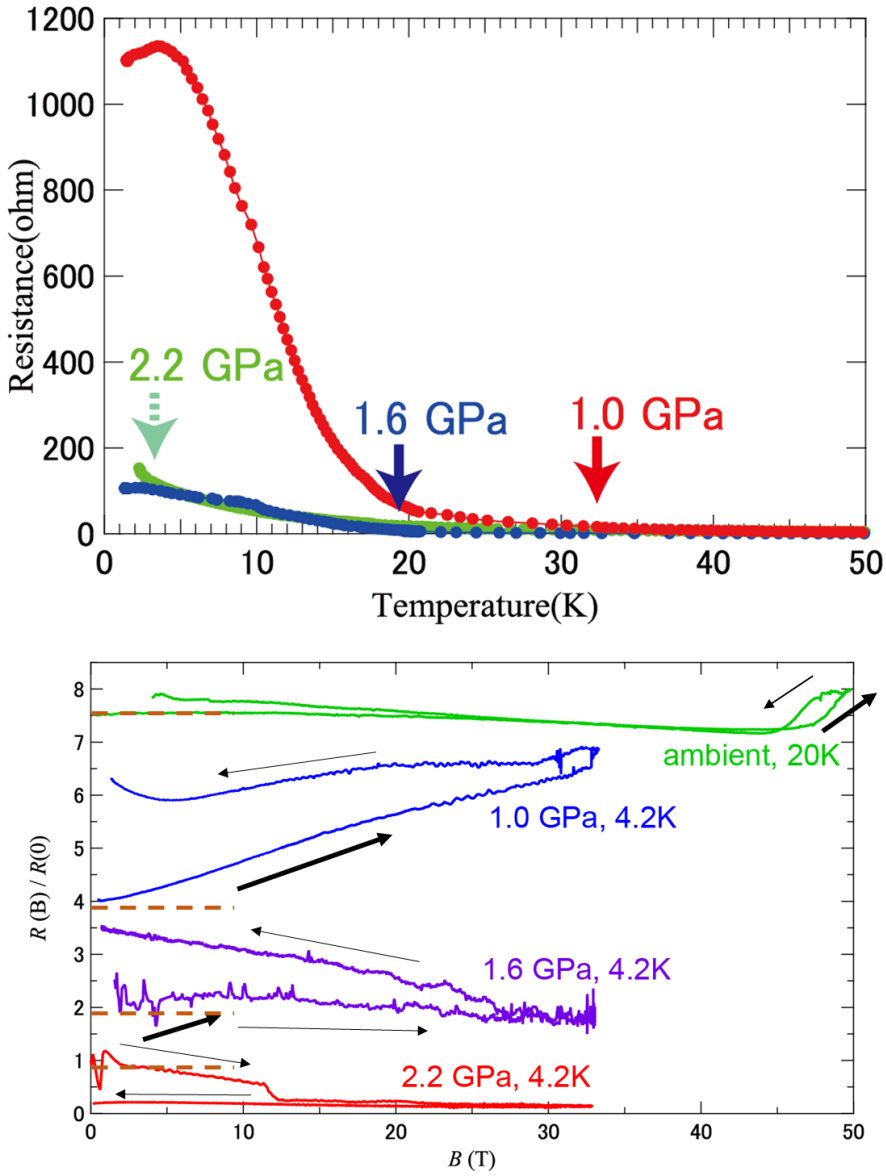

Figure 1.17: (upper panel): (Preliminary-) experimental results of the temperature dependence of resistance of $BaVS_3$ under high pressure for current: $i \parallel c$-axis condition. The solid arrows represents $T_{\rm MI}$ for designed pressure. At 1.0 GPa and below 4.2 K, metallic state with $(\mathrm{d}R/\mathrm{s}T > 0)$ was observed. At 2.2 GPa, above $p_{\rm cr} \sim 2.0$ GPa, there is no peak at $(\mathrm{d}R/\ \mathrm{d}(1/T))$, but the resistance continues to increase down to 2 K (dotted arrow), which is probably due to poor sample purity (see Appendix for impurity effects). (lower panel): Magneto-resistance for $B \perp i$, $i \parallel c$-axis conditions. Magneto-resistance under ambient pressure (without pressure cells) is shown as reference data. The data is shifted upward for readability. Magneto-resistance has hysteresis, probably due to the long relaxation time of CDW domain alignment.

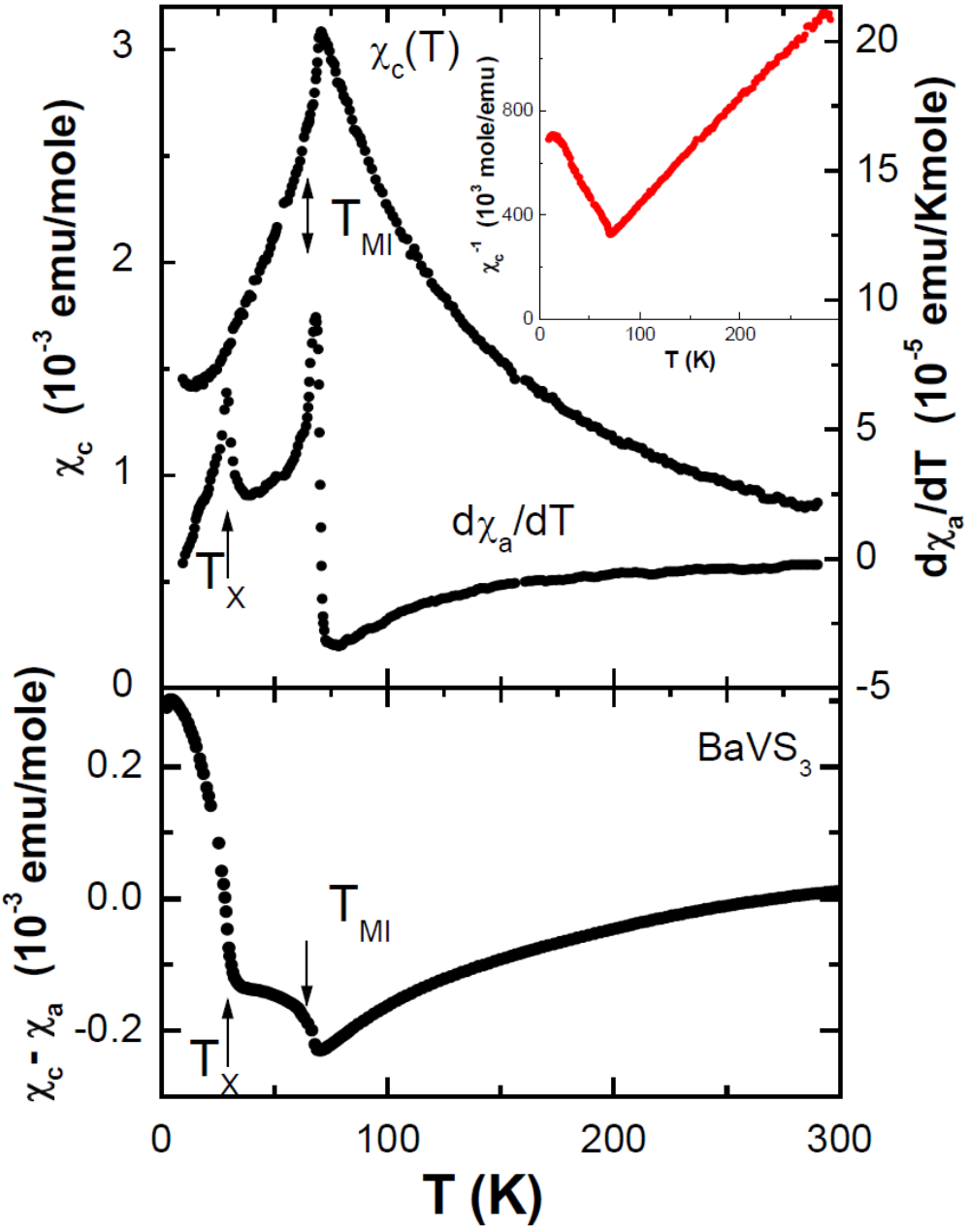

Figure 1.18: Temperature dependence of (upper panel) magnetic susceptibility χ_c and $\mathrm{d}\chi_a/\mathrm{d}T$, and (lower panel) $\chi_c - \chi_a$, where χ_c and χ_a represent magnetic susceptibilities along the c and a axis of $BaVS_3$, respectively[15]. The inset of upper panel shows the inverse magnetic susceptibility $1/\chi_c$ [26]. Magnetic susceptibility shows a steep decrease below T_{MI}. At first glance it appears to be magnetically ordered at T_{MI}, but that is not true (see Fig. 1.19). [28]

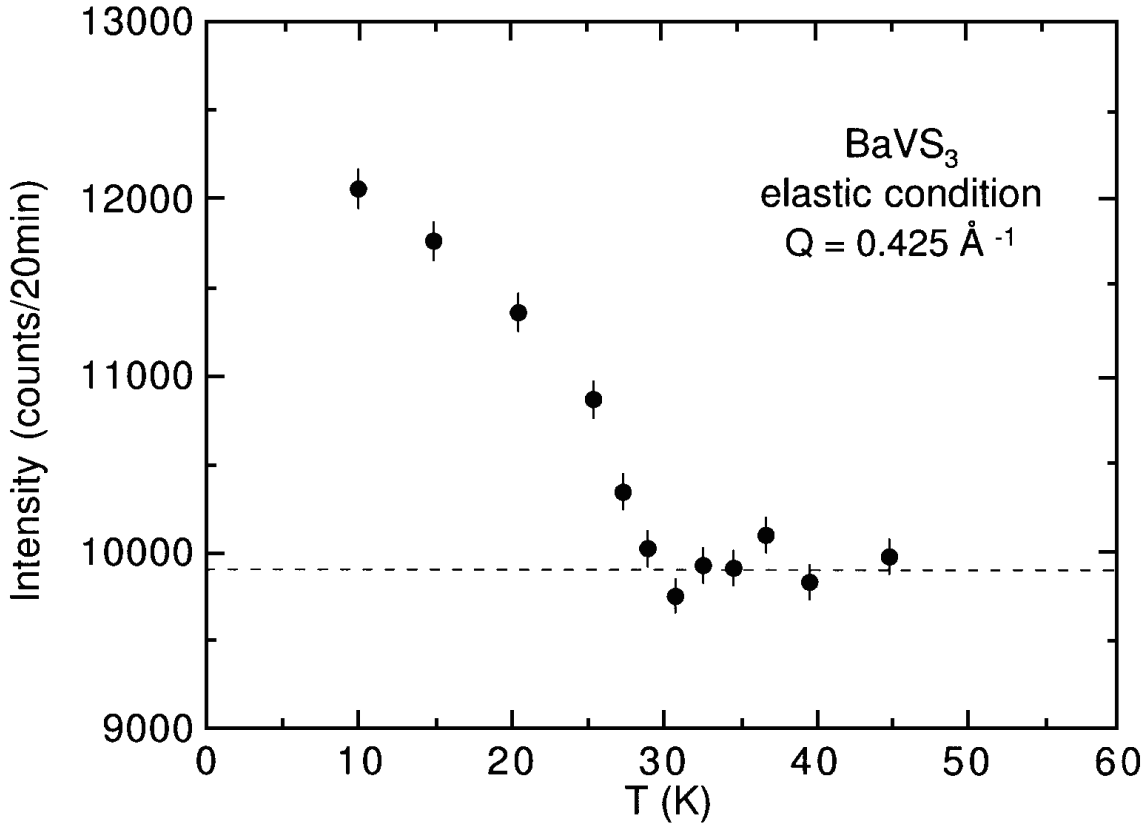

Figure 1.19: Temperature dependence of the magnetic intensity of the peak at $Q = 0.425$ Åin the elastic neutron diffraction measurements. [28] Peak intensity increases rapidly below $T_{\rm x} \sim 30$ K, indicating the magnetic order develops below $T_{\rm x}$.

Finally, we mention the results of high field magnetization of $BaVS_3$. A metamagnetic transition was observed at transition field $B_M \sim 50$ T at 4.2 K both for $B \parallel c$and $B \perp c$, as shown in Fig. 1.20. [30] The magnetization curve exhibits a magnetization plateau above B_M with the magnetization value of about 0.4 μ_B/f.u., which is consistent with the evaluated ordered moment by the neutron diffraction experiment[28]. Importantly, the plateau that appears to be saturated (after the metamagnetic transition) is another magnetic state that is different from the "forced ferromagnetic state", which is thermodynamically equivalent to high temperature paramagnetic state (see Fig. 1.21). The origin of this metamagnetic transition and the state after the transition were still unclear.

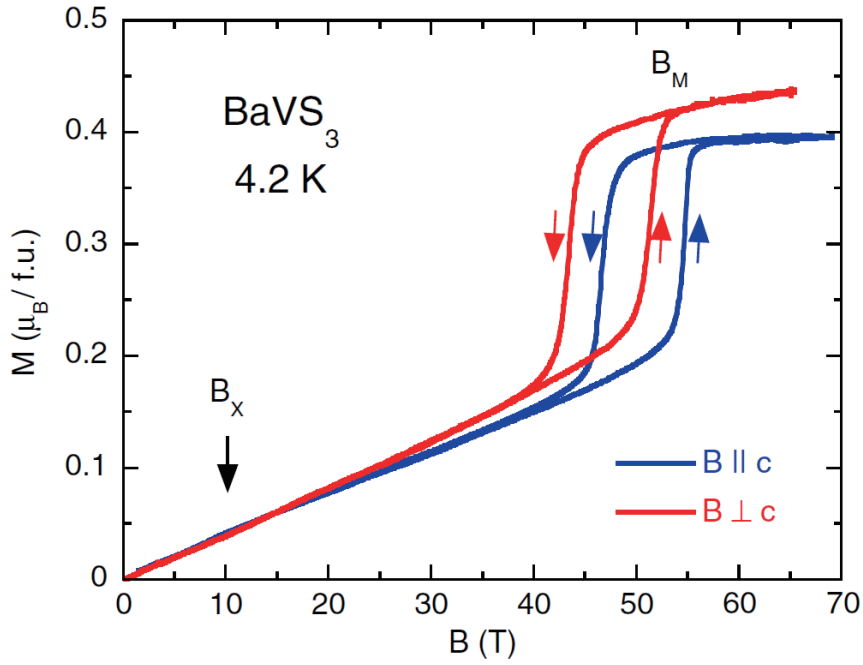

Figure 1.20: High field magnetization curves of a single crystal sample of $BaVS_3$ at 4.2 K. A metamagnetic transition with large hysteresis of about 8 T was observed at $B_M \sim 55$ T for $B \parallel c$ axis, and $B_M \sim 50$ T for $B \perp c$.[30] The magnetization value of about 0.4 μ_B/f.u. at $B = 60$ T was estimated, which value is approximately half of the saturation magnetization expected for V^{4+} with spin $S = 1/2$.

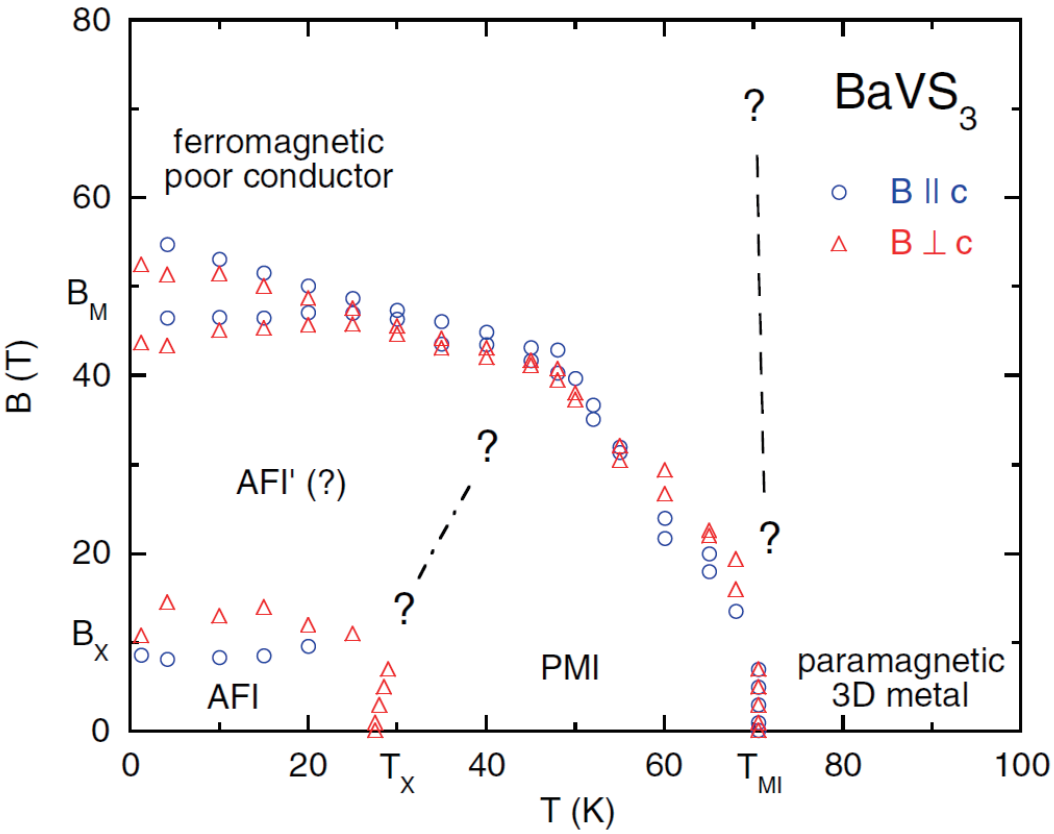

Figure 1.21: Magnetic field-Temperature (B-T) phase diagram of $BaVS_3$ constracted by the results of high-field magnetization measurements and magnetic susceptibility measurements.[30]

1.2.5 Summary of previous studies

This section has described the physical characteristics of $BaVS_3$. Although a number of studies have been conducted on $BaVS_3$, some important issues are still remained, one of them is the magnetic state, especially below T_{MI}. Through the discussion in the previous studies, the following premise is believed. The vanadium sites have spatial modulation (even at room temperature), half of the vanadium sites are V^{4+} with $S = 1/2$, while the other half are not spin-polarized. However, there is no experimental evidence showing spatial splitting of electronic state of vanadium below T_{MI}. This means that the splitting was not observed regardless of the experimental effort.

1.2.6 Motivation of this study

In order to clarify the magnetism of $BaVS_3$, it is essential to study its magnetic properties under pressure. Especially, we aimed at observing how the metamagnetic behavior, for which there was no reasonable explanation, changes by applying hydrostatic pressure. Since $BaVS_3$ has at most $S = 1/2$ magnetism, we thought that it was difficult to measure magnetic properties with sufficient quality by using a commonly used magnetization detection system under pressure. Therefore, we had developed a measuring device at first, and later measured magnetic susceptibility and magnetization. The details of the experiment are described in experimental chapter..

2 Experimental

2.1 Sample preparation

$BaVS_3$ powdered samples were synthesized by the solid state reaction technique and annealed in sulfur gas atmosphere[24]. We utilized a Teflon cylinder (ID - OD= ϕ 1.4 - 2.0 mm, $L = 8.0$ mm) as a sample cell, and $BaVS_3$ powder of about 40 mg was packed into the cell. We were afraid of that sulfur deficiency might occur when the sample was directly pressed (or axial pressure), which is similar to the situation of making a sintered sample. Hence we adopted the combination of powder sample and soft cell, and fixed them with varnish.

We should note that we have previously performed all experiments with single crystal samples of about 100 needle crystals (total amount of $\sim$ 20 mg). However, we could not observe expected metamagnetic transition even at ambient pressure, due to probably sample quality such as sulfur deficiency. This study shows that the powder sample is sufficient for observing the metamagnetic transition of magnetization and the change in magnetic susceptibility under pressure.

2.2 High pressure application

We used a CuBe piston cylinder-type pressure cell and Daphne 7474 oil as a pressure medium. Figure 2.2 shows a cut view of piston cylinder-type pressure cell.

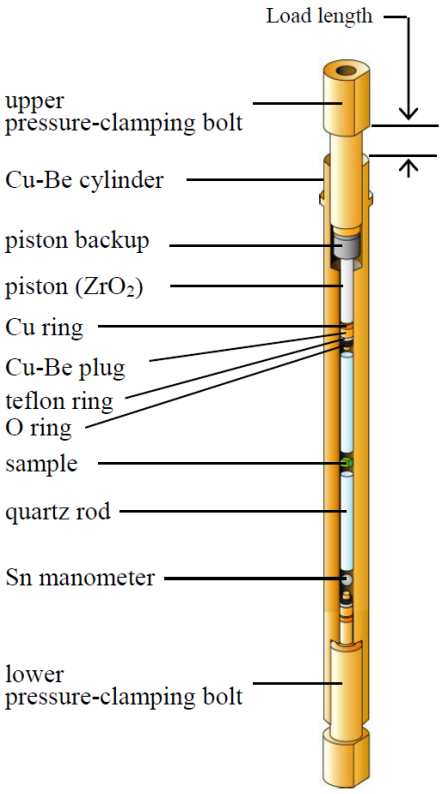

Figure 2.1: Cut view of our CuBe piston cylinder pressure cell.

Since the piston cylinder has a simple structure, the characteristic pressure of the pressure cell can be evaluated based on material mechanics calculations, as shown in Fig.2.2 [31]. The curve *e*-*g* represents an elastic deformation, the *e*-*j*-*i* curve is a curve with full plastic deformation in the entire cell (= cell breaks), and the curve of *e*-*j*-*h* shows partly plastic deformation. R is available region for the large residual plastic deformation. The utilizable pressure with the piston cylinder pressure cell lies in the meshed region R. In our pressure cell, the highest pressure is about $p_{\max} \sim 1.3$ GPa from $K = 6$ cm / 2 cm = 3, $S_y \sim 1.3$ GPa.

In terms of material engineering, the longer the cylinder length, the higher the generated pressure. However in practice, due to the eccentricity of the cylinder outer wall and the bore, the piston-cylinder cell can be destroyed without reaching the material strength limit. The longer the cylinder length, the more eccentric the cylinder is during machining. To balance these conditions, we have prepared a pressure cell with a cylinder length of 9.5 cm. The detailed designs of pressure cell are shown in Appendix.

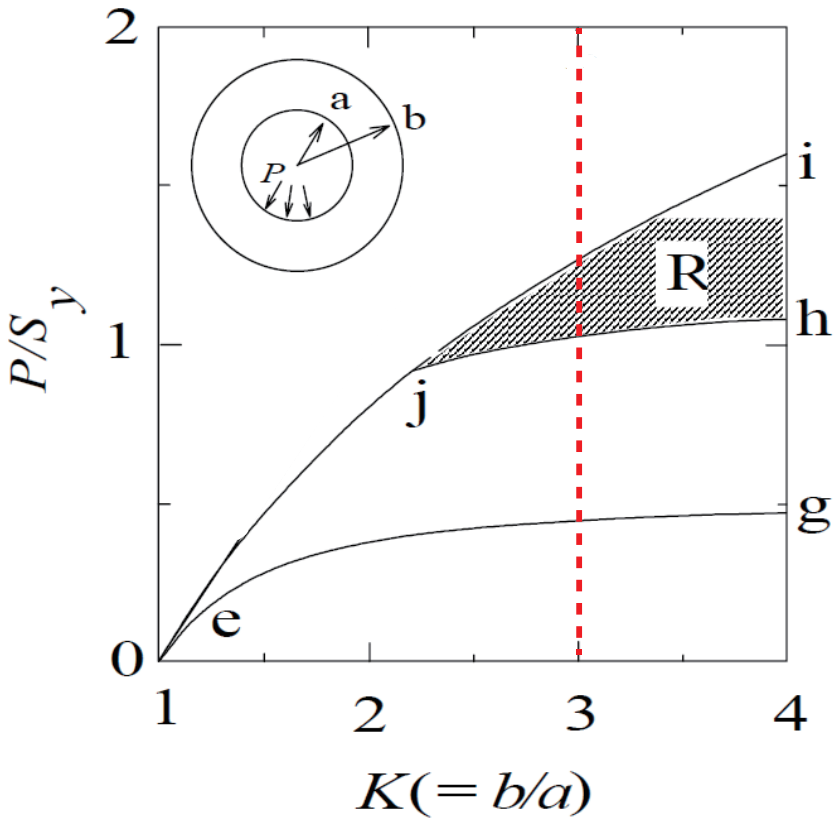

Figure 2.2: Generated pressure calculated by inner/outer radius ratio $K = b/a$ with infinite cylinder length. S_y represents the reference strength, such as the yield strength and/or tensile strength. *e*-*g*: elastic deformation cell. *e*-*j*-*i*: full plastic deformation cell. *e*-*j*-*h*: partly plastic deformation cell. *R*: available region for the large residual plastic deformation.

CuBe is an alloy with a tensile strength of about 1.3 GPa, which is not suitable for measurement of $BaVS_3$ with the critical pressure of the MI transition p_{cr} of 2.0 GPa. Due to the high conductivity of alloys, the compatibility of the pulsed magnetic field with this pressure cell is poor. If possible, it is better to use a pressure cell made of NiCrAl alloy, which has higher tensile strength (2.2 GPa), and lower conductivity, but larger background-para-magnetism than those of CuBe alloy. The magnetization signal of $BsVS_3$ in the NiCrAl pressure cell could not be observed due to the large background signal even with SQUID magnetometer, and thus we utilize CuBe pressure cells.

The pressure was estimated from the superconducting transition temperature T_c of Sn. Figure 2.3 and 2.4 show the magnetic field dependence of T_c. We determined $T_c(p)$ at zero magnetic field as cross point (dotted circle in Fig. 2.4) of linear approximations of $T_c(P, B)$ at the two regions of +10 $\sim$ +40 Oe and -10 $\sim$ -40 Oe. Then, the pressure was determined by using the following equation[32];

$$T_c(p, 0 \text{ Oe}) - 3.764 = 4.63 \times p - 0.0216 \times p^2. \tag{2.1}$$

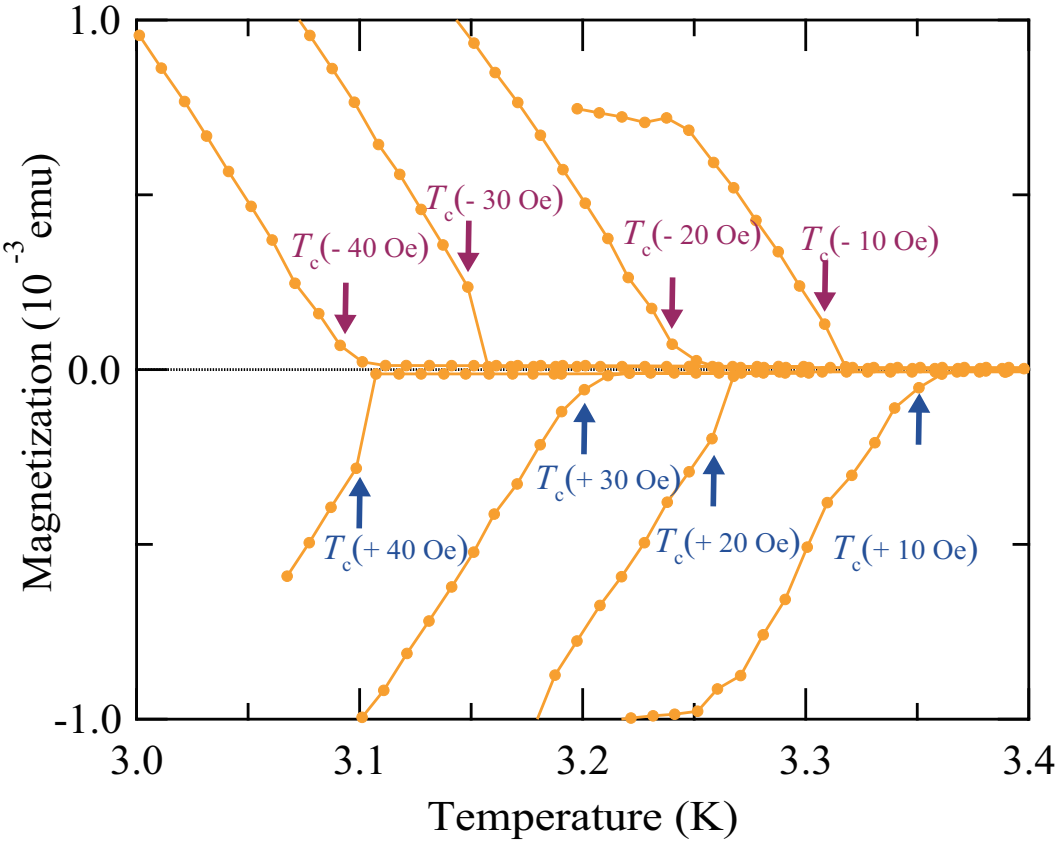

Figure 2.3: Diamagnetism of tin superconductivity under 0.80 GPa at several magnetic field, taking into account the effect of the residual magnetic field. The arrows indicates the critical temperature of tin's superconducting transition in certain magnetic fields. The first temperature at which the diamagnetism exceeded 10^{-4} emu (in 0.01 K steps) is defined as T_c. In this definition method, the error in pressure due to mis-evaluation of T_c was empirically about 0.02 GPa

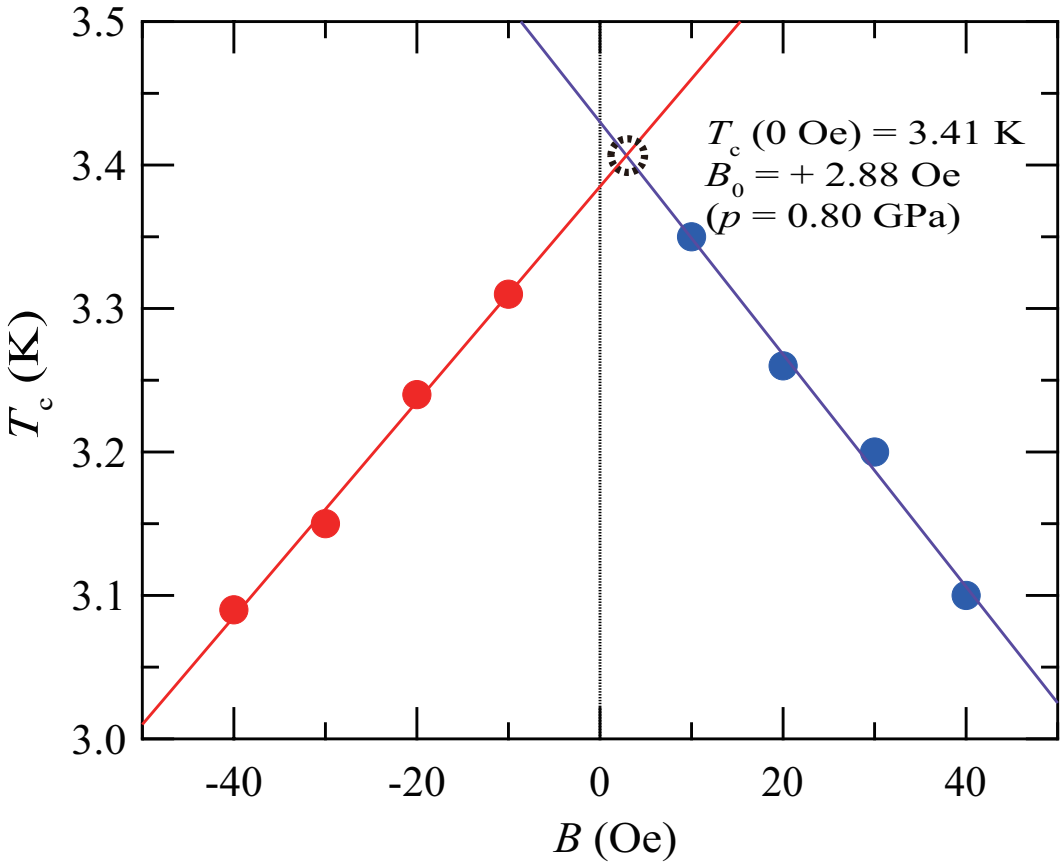

Figure 2.4: Determination of $T_c(p)$ at zero magnetic field. The filled circles represents the critical temperature measured in Fig. 2.3. In this case, residual magnetic field is $B_0 = +2.88$ Oe, and the superconducting transition temperature is $T_c(p, 0\text{ Oe}) = 3.41$ K, and thus the calculated pressure is $p = 0.80$ GPa by the equation 2.1.

2.3 Low-field magnetization and magnetic susceptibility

Low-field magnetization (T = 4.2 K, B : 0 $\sim$ 7 T) and magnetic susceptibility (T : 2 $\sim$ 300 K, B : 1.0 T) were measured using a SQUID magnetometer (Quantum Design, MPMS XL-7L). In order to eliminate background signal from pressure cell, we developed and used an analysis method, as follows; (See §3.3.4 in Ref. [33])

- Collect background data of only pressure cells with FULL DC SCAN ...(1)
- Measure data of sample + pressure cell with FULL DC SCAN ...(2)
- Subtract the data (2) - (1) ...(3)
- Determine the reference (temperature, magnetic field) conditions ...(4-1)
- Mask a part of scan length (corresponding to "Scan Length" in normal DC measurement) (4-2)
- Perform "three-gaussian fitting" on the masked data (4-3)
- Repeat (4-1) to (4-3) so that all fitting parameters are 90% or more (4-4)
- Perform fitting with the determined area and initial values for all measurement (temperature, magnetic field) conditions (4-5)
- Evaluate the magnitude of magnetization (5):

Here, "three gaussian fitting" was performed to the SQUID voltage $V(x)$ data as follows:

$$\begin{aligned} V(x) =& A \times exp\left(-\left(\frac{x-x_0}{d}\right)^2\right) \\ & - \frac{1}{2}A \times \left[exp\left(-\left(\frac{x-x_0-x_1}{d}\right)^2\right) + exp\left(-\left(\frac{x-x_0+x_1}{d}\right)^2\right)\right] \\ & + a_0 + a_1 \cdot x \end{aligned} \tag{2.2}$$

where A is an coefficient for determining the magnitude of magnetization, x means rod position, x_0 represents sample center position, x_1 and d are variables due to spatial distribution of measuring coils, a_0 and a_1 shows background correction parameters, respectively.

We show the three-gaussian fitting of the SQUID voltage data in Fig. 2.5. Theoretically, the SQUID voltage $V(x)$ (red points) are calculated as the sum of the contributions from three coils. The theoretical formula, however, seems to be weak to noise gains at a position farther than the sample center position ($|x| >> 2$), and the magnetization signal with the pressure cell could not be evaluated. Our devised three-gaussian fitting (black line) is a solid fitting for noise away from the sample center, and can fully approximate the red pints in the region of $x < \pm\ 1.8$. It should be noted that in the gaussian-fitting, a_0 and A greatly changes depending on the fitting range, and may cause an error in the magnetization evaluation of the measurement sample. To solve this problem, we calibrated the coefficient in the same fitting range for each measurement using the standard sample Pd. With this fitting, we were able to observe small changes in the magnetization of $BaVS_3$ with sufficient accuracy.

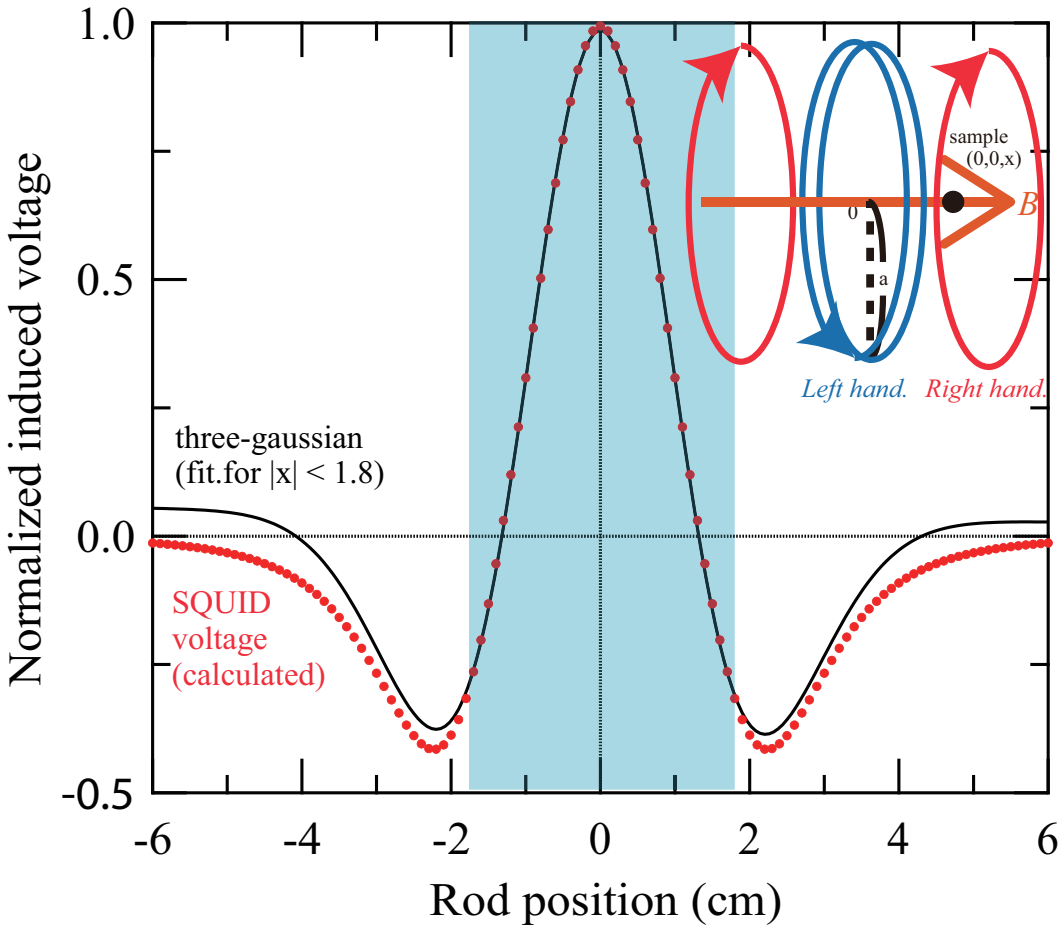

Figure 2.5: Demonstration of three-gauss fitting. The inset figure shows the schematic view of induction coil in SQUID magnetometer. The red points represents the SQUID voltage with B-A-B type aligned induction coils (B: Left handed, A: Right handed), conventional alignment for SQUID magnetometer. The induced SQUID voltage is calculated data. In the region of $|x| < 1.8$, three-gauss fitting seems to be a good approximation for red plot.

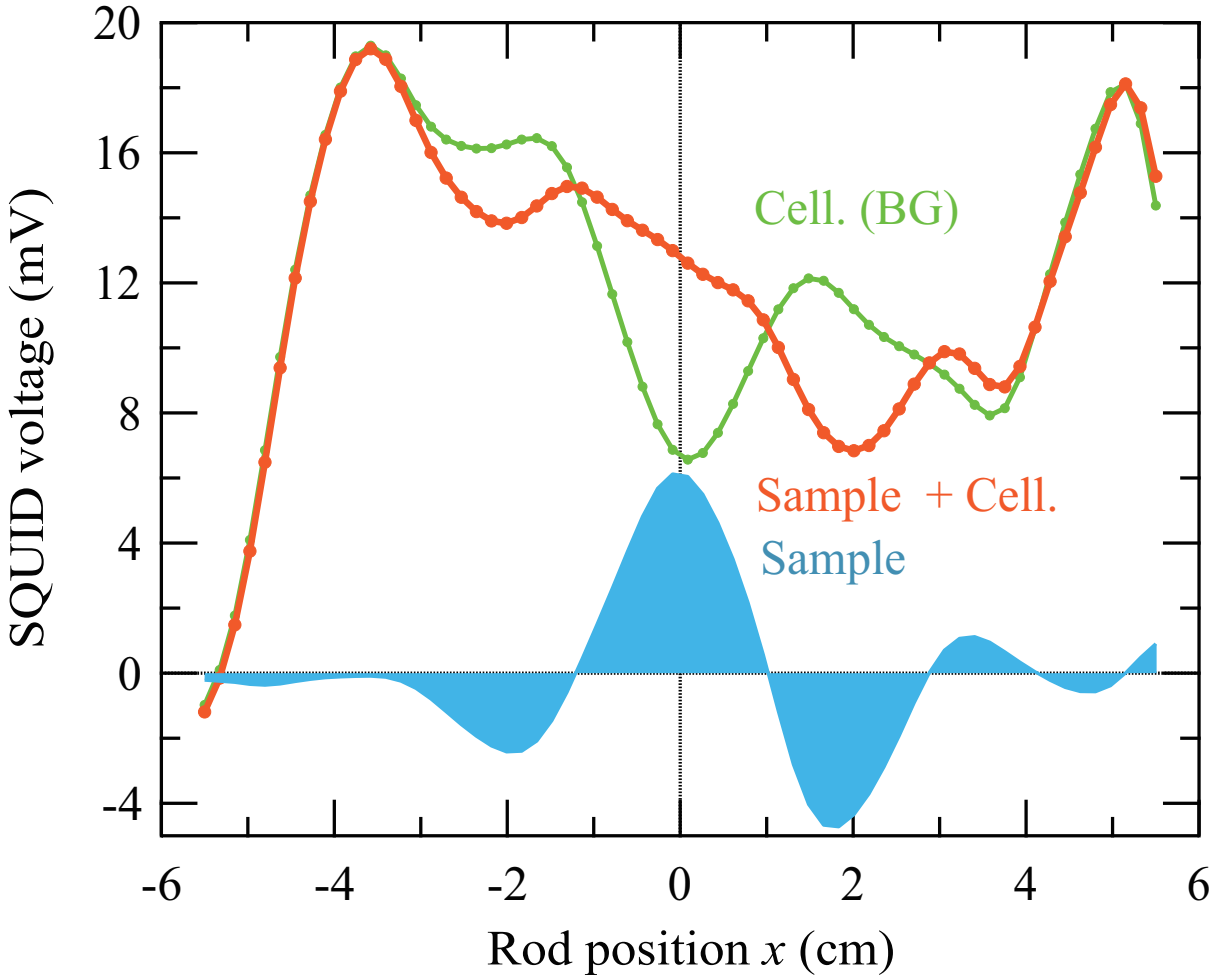

Figure 2.6: Position dependences in SQUID voltage data for background signal from pressure cell (orange) and pressure cell with $BaVS_3$ sample (green). The blue plot shows ((orange) - (green)). (Sample is placed at -0.4 $< x <$ 0.4 cm.)

The analysis procedure from the subtraction of the SQUID voltages mentioned before to the magnetization data for magnetic susceptibility and low-field magnetization, the conditions at (0.70 GPa, 1.0 T, 2 - 300 K) is shown in Figs.2.7 - 2.10.

The program macros used in the above analysis are described in Appendix 1.

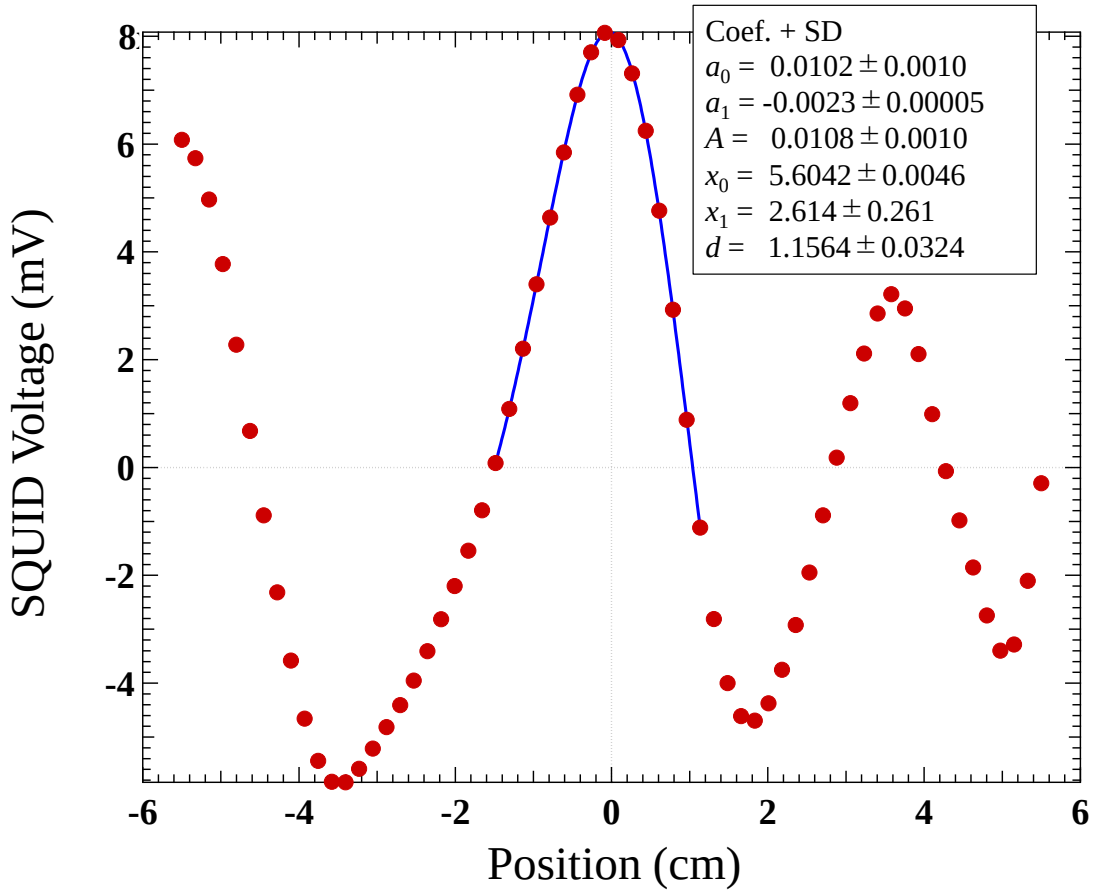

Figure 2.7: Fitting of the experimental data at the conditions of 0.70 GPa, 1.0 T, and 2.0 K. We performed three-gaussian fitting in $4.0 < x < 7.0$ region (Position: $-1.5 < x - x_0 < 1.5$) and obtained the inset parameters. The plot is shifted sideways so that x_0 is the center of the figure.

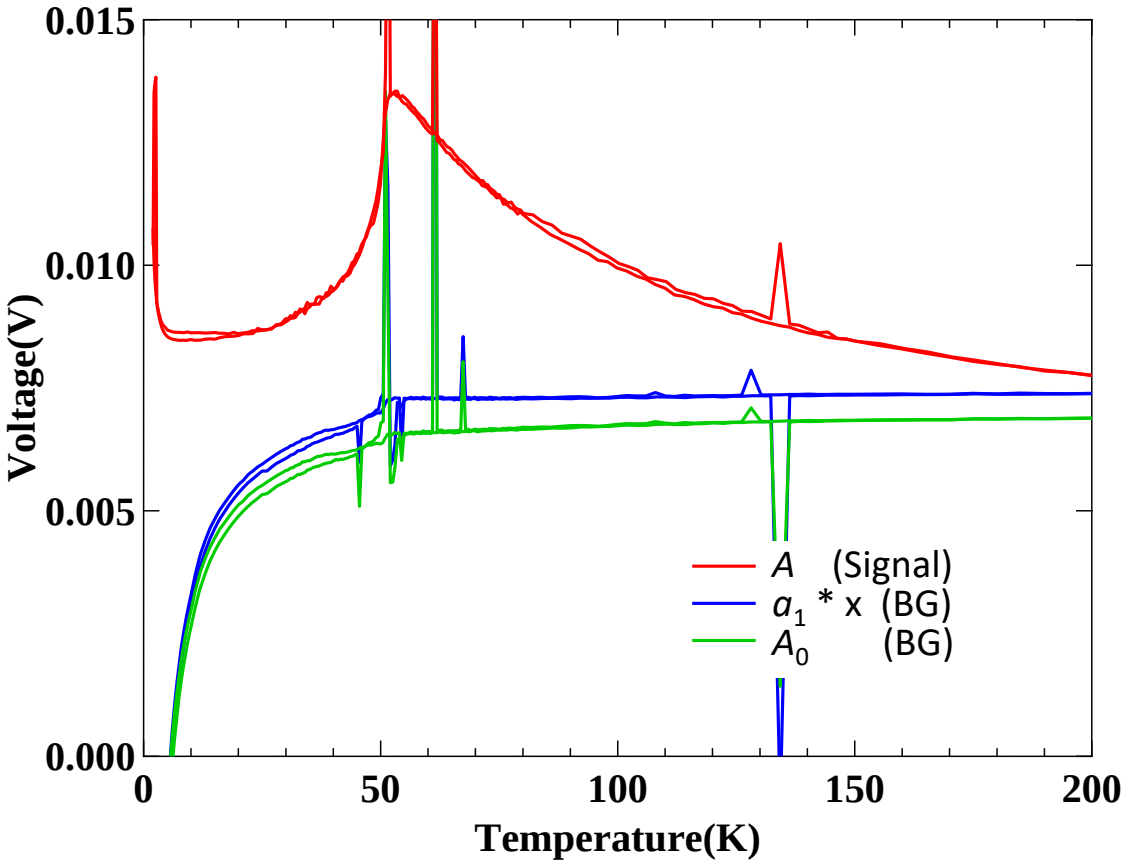

Figure 2.8: Obtained fitting parameters $(A, a_0, a_1 x_0)$ of the experimental data at the conditions of 0.70 GPa, and 1.0 T. The red line (A) represents the temperature dependence of magnetic susceptibility in $BaVS_3$, and the others (a_0, a_1) correspond to remaining background components at the sample position. The spiked anomalies around 50 K, 60 K, 130 K are caused by poor fitting. The sudden increase in magnetization below 10 K is caused by the paramagnetism of background which could not be completely subtracted.

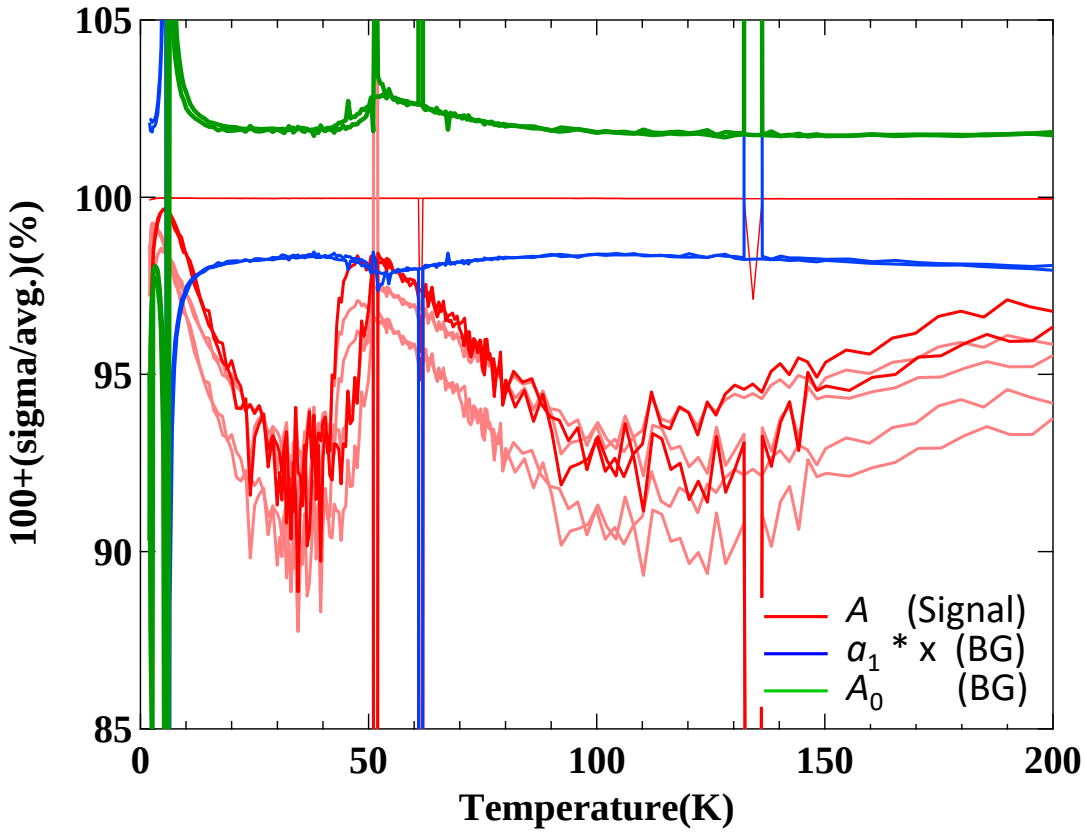

Figure 2.9: Error in parameters $\frac{sigma}{average}(\%)$ calculated from the fittings. The plot colors correspond to those in Fig. 2.8. We set "good fitting data" when the deviation of the data is below 10% (90-110 in the figure) and used them as the measurement points.

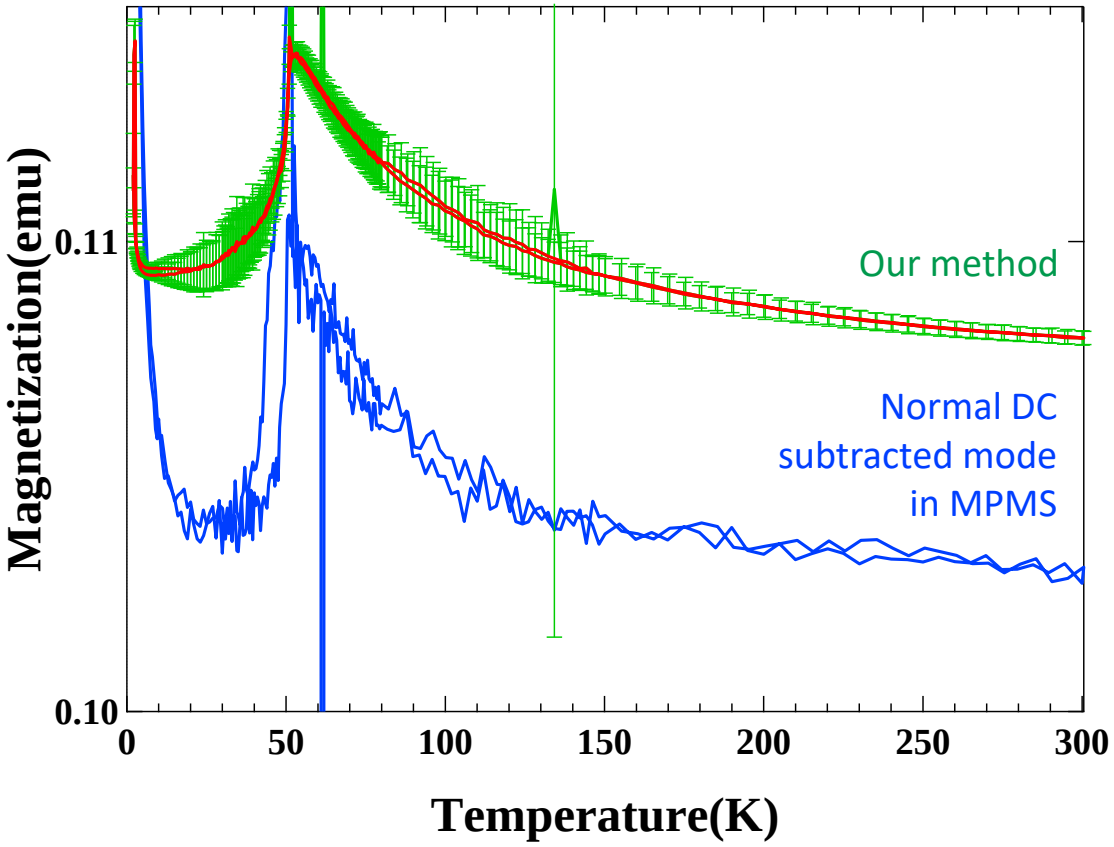

Figure 2.10: Magnetization data measured at 1.0 T. The upper curve shows the data delivered by our original analysis method. The calculated central value is indicated by a red dot and the error is indicated by a green bar. The lower curve indicates the data measured with normal DC-subtracted mode. The latter data is smaller than the actual magnitude magnetization value. This means the background subtraction is not perfect. The sudden rise in magnetization near the lowest temperature is a component from the pressure cell that could not be subtracted.

2.4 High-field magnetization

High-field magnetization measurements were done by an induction method at 4.2 K in pulsed magnetic fields of up to 55 T with 40 ms pulse duration, as shown in Fig.2.11. The absolute value was calibrated by the low-field magnetization data mentioned above. We show in Fig.2.12 a block diagram of high-field magnetization measurement system.

In general, there are four major problems when we measure magnetization under high pressure in a pulsed high magnetic field.

- Magnetic field shielding effect by skin depth of metal pressure cell.
- Temperature rise due to Joule heating caused by eddy current.
- Out-signal misalignment by spatial distribution of pressure cell components.
- Enhancement of magnetic field inhomogeneity due to pressure cell para-magnetism.

To address these issues, we have taken the following actions:

- Confirmation that there is no $\mathrm{d}B/\mathrm{d}t$ (field sweep speed) dependence in transition magnetic field.
- Insertion of Teflon, a thermal insulation material, between the metallic cell and sample.
- Averaging out-signal at several positions.
- Mount as much samples as possible and repeat the measurement, and integrate the data.

With these efforts we were able to conduct significant magnetization measurements up to 55 T, while keeping the temperature of the sample probably below 10 K (with initial temperature: 4.2 K), which is far below the characteristic temperatures T_{N} and T_{MI}. We performed all the high-field measurement in 4.2 K liquid helium.

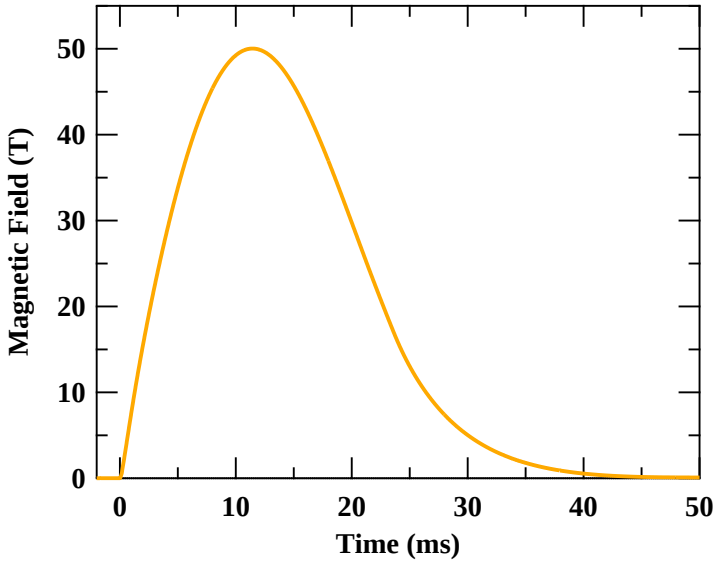

Figure 2.11: Time dependence of magnetic field

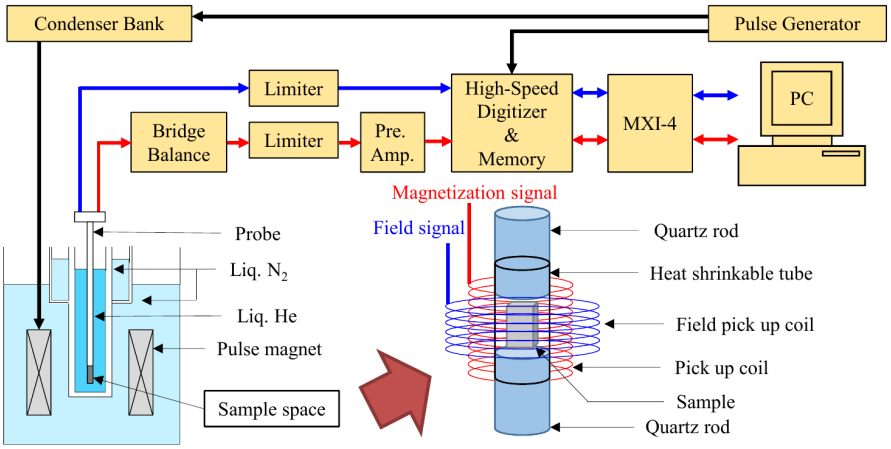

Figure 2.12: Block diagram of magnetization measurement system

The induced voltage due to the time differential of the magnetic field is about three orders of magnitude larger than that of the magnetization. In actual measurement, it is necessary to eliminate the contribution of the magnetic field by devising the arrangement of the pick-up coils. Figure 2.13 shows the schematic coil design of magnetization measurement under high pressure, used in this study. Because the space between the pressure cell and pulse magnet is narrow, where pick-up coil is wound, we have adopted a "B-A-B type" pick-up coil arrangement instead of the "co-axial coil " arrangement commonly used for magnetization measurement in a pulsed magnetic field.

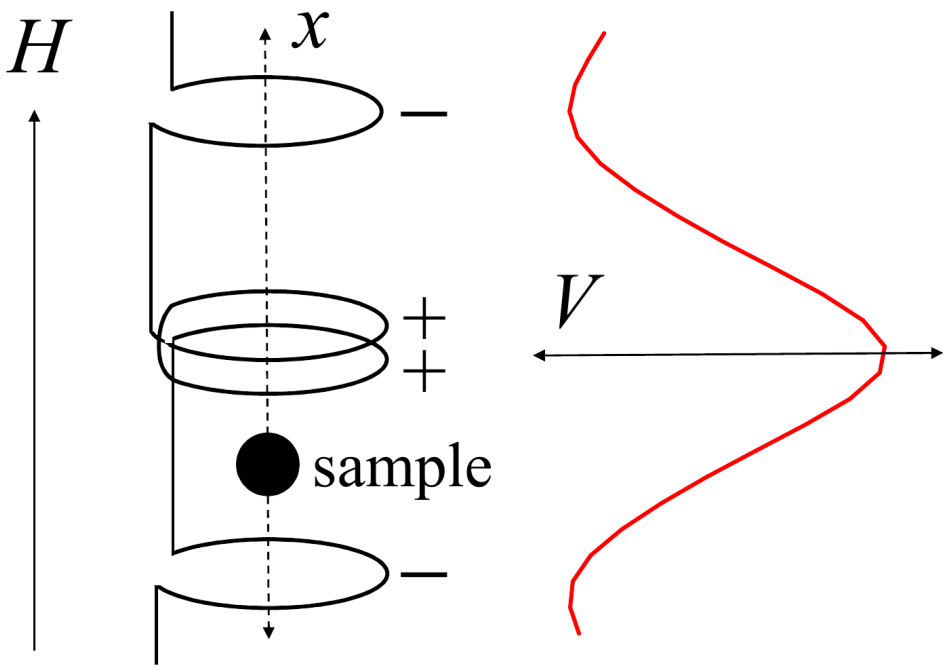

Figure 2.13: (left): Schematic configuration of a pick-up coil for magnetization measurements under high pressure. From top, 40-turns (ccw), 80-turns (cw), and 40-turns (ccw) to vanish the voltage induced by external magnetic field. cw: clock-wise, ccw: counter clock-wise. (right) Expected sample position dependence of magnetization-induced voltage in our magnetization measurement system.

In the magnetization measurement by the induction method, difference between induced voltage when the sample is at the center of the pick-up coil (V_{in}) and when the sample is far enough from the pick-up coil (V_{out}) corresponds to the time derivative of magnetization $\mathrm{d}M/\mathrm{d}t$. We show an example of induction voltage (V_{in}) and (V_{out}) in Fig. 2.14, and subtracted voltage (V_{in}) - (V_{out}) in Fig. 2.15. In the magnetization measurement under pressure, the sensitivity is lower than in the normal magnetization measurement at ambient pressure, and there are many noise sources. Due to the poor signal-to-noise ratio, it is difficult to evaluate meaningful results in a single measurement. We performed magnetization measurements several times under the same conditions, integrated the data, and made an effort to increase the accuracy of the experimental results.

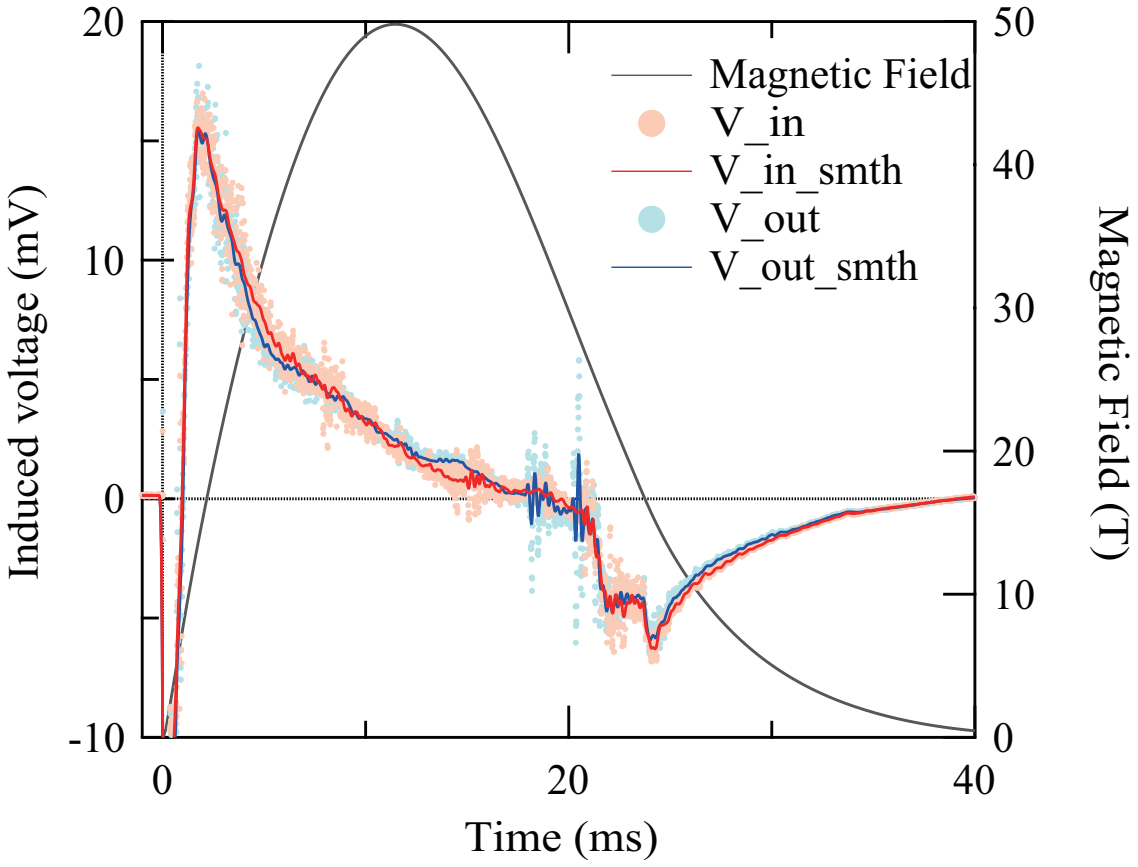

Figure 2.14: Induced raw voltages V_{in} (orange) and V_{out} (blue). The light circle plots represent the raw induced voltages at each sample positions. Red- and blue- solid lines are the results of smoothing

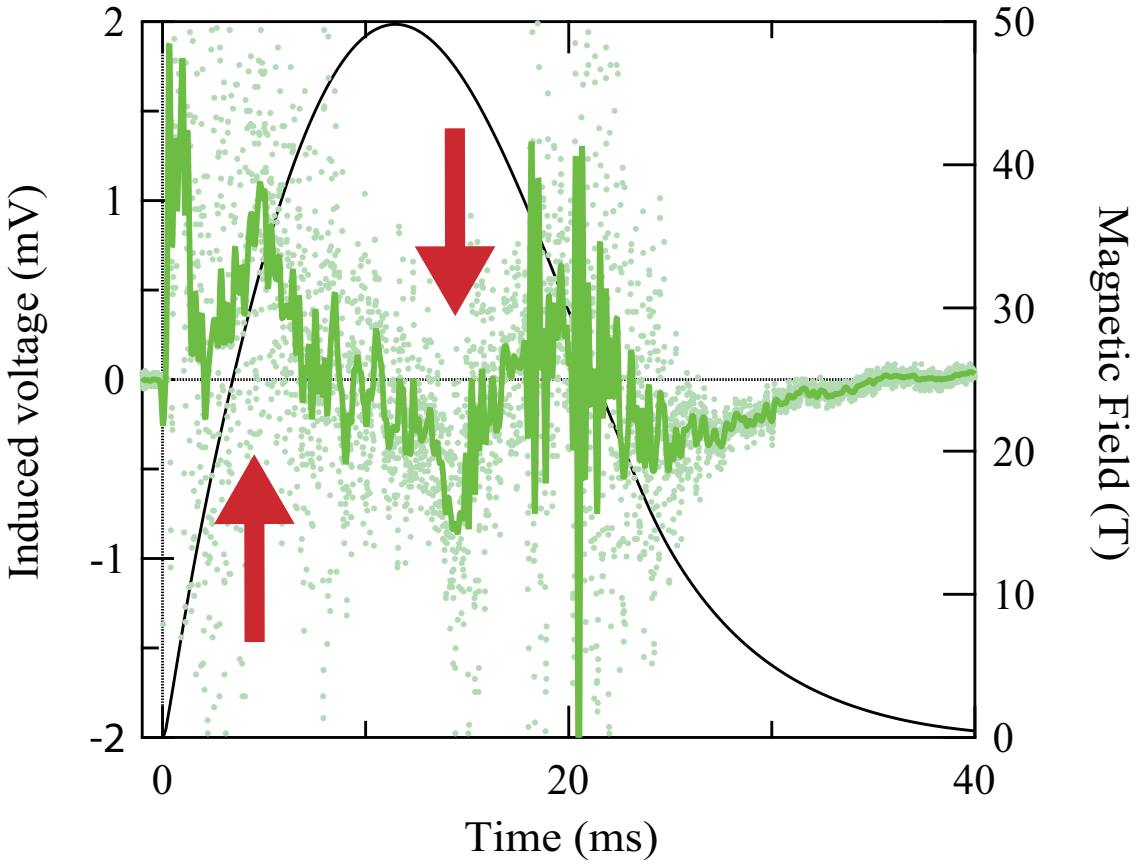

Figure 2.15: Subtracted induced voltages V_{in} - V_{out}. The green solid line is the result of smoothing. Red arrows indicate a sudden increase in $\mathrm{d}M/\mathrm{d}B$, corresponding to a metamagnetic transition.

3 Results and analyses

3.1 High-field magnetization curve

First, we confirmed whether a metamagnetic transition was observed in the powder samples used in this study. Metamagnetic transition that had been observed in polycrystalline sample in the past [34] were less obvious than experiments with single crystal samples. If the clear metamagnetic transition occurs only in a single crystalline sample, then the metamagnetic transition is likely to be due to magnetic anisotropy. If the metamagnetic transition is observed in a powdered sample, it is caused by level crossing that means collapse of the energy gap by a magnetic field.

Figure 3.1 shows magnetization curve of a powder sample of $BaVS_3$ at ambient pressure in magnetic fields of up to 53 T. We observed a metamagnetic-transition with large hysteresis of about 8 T at the transition field $B_M \sim 50$ T. Note that the transition magnetic field during the application of the magnetic field was adopted as B_M. The metamagnetic transition did not become multi-step transitions and the magnetization curve seems to be the same as that of a single crystal sample for $B \perp c$[30], indicating that the magnetic exchange interaction is almost isotropic and weak. (Note that this magnetization curve is of magnetic ordered state.) We considered that the weak anisotropy of metamagnetic transition field observed in the single crystal is caused by the symmetry of the spin gap, which must be anisotropic in momentum space. Here after, only the magnetization curve for field ascending process is indicated.

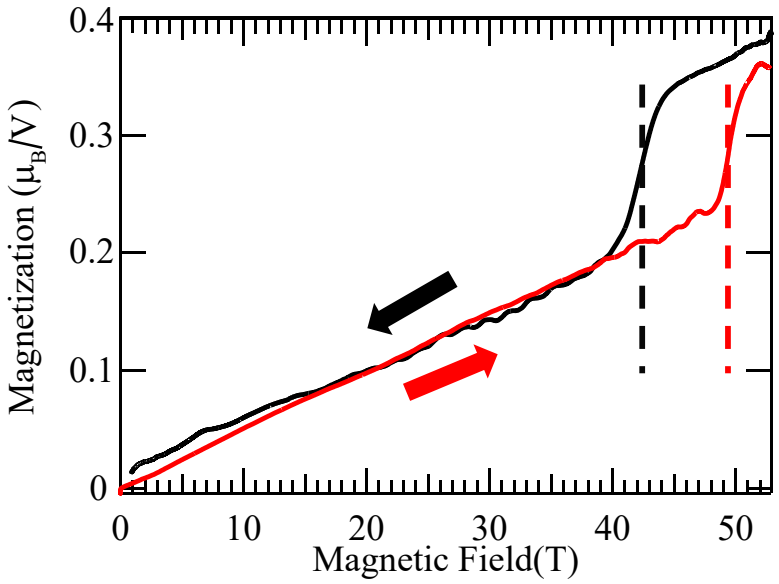

Figure 3.1: High field magnetization curve of a powder sample of $BaVS_3$ at ambient pressure. The red and black lines represent field ascending and field descending process, respectively. The broken line shows the critical magnetic field where dM/dB shows a peak.

We show the pressure dependence of the magnetization curves in Fig. 3.2. We clearly found that the B_{M} monotonically decreases with increasing pressure. The metamagnetic transition broadens with increasing pressure, shifts to low magnetic field side, and is not observed at 0.90 GPa (see also Fig. 3.3).

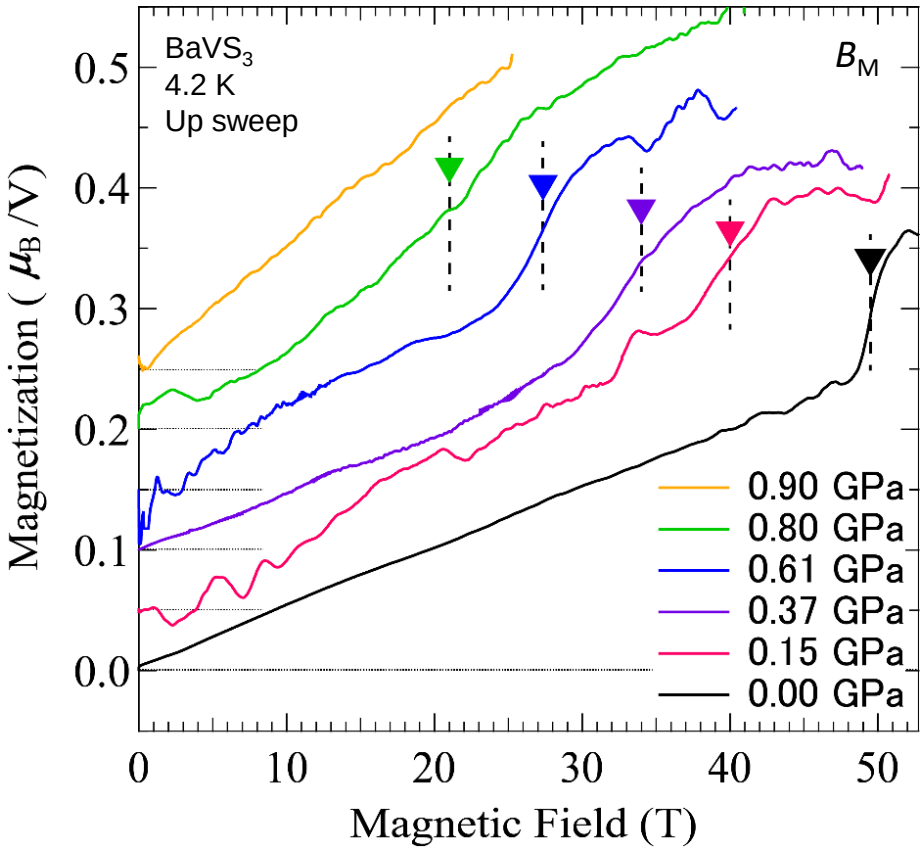

Figure 3.2: High field magnetization curves under designated pressures. Triangular marks with a broken line represent the metamagnetic transition fields for each pressures. The plots under pressure shift upside for readability.

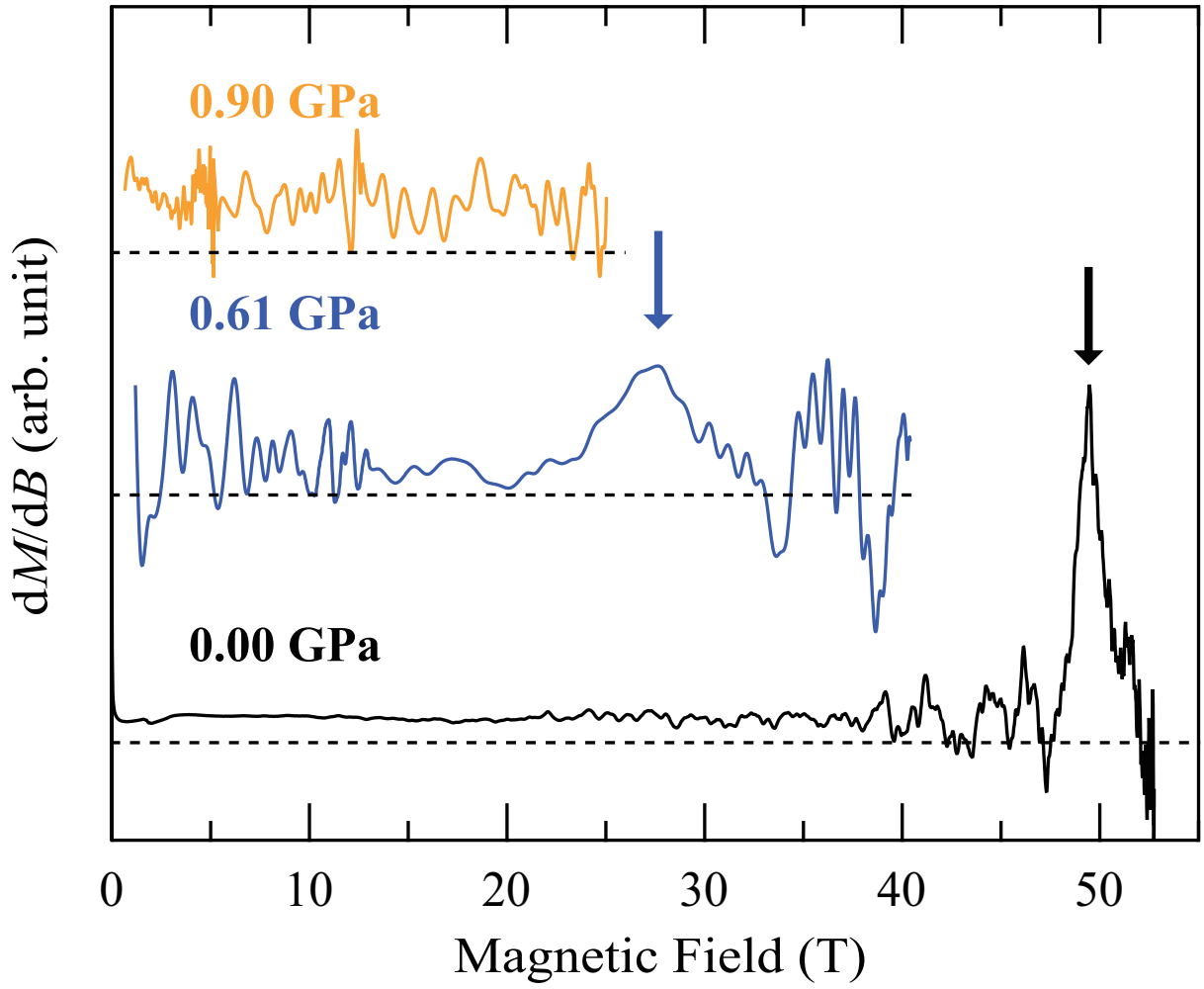

Figure 3.3: $\mathrm{d}M/\mathrm{d}B$ at 0.00 GPa , 0.61 GPa and 0.90 GPa. Arrows indicate the critical field of the metamagnetic transition at 0.00 GPa and 0.61 GPa. No significant peak was observed in $\mathrm{d}M/\mathrm{d}B$ at 0.90 GPa.

3.2 Analysis of magnetization curve

3.2.1 Pressure-Magnetic field(p-B) phase diagram

A new pressure-magnetic field (p-B) phase diagram was constructed from the metamagnetic transition field data, as shown in Fig. 3.4. The B_{M} shows the linear pressure dependence below 0.80 GPa, and suddenly disappear at $p_{\mathrm{M}} \sim 0.90$ GPa.

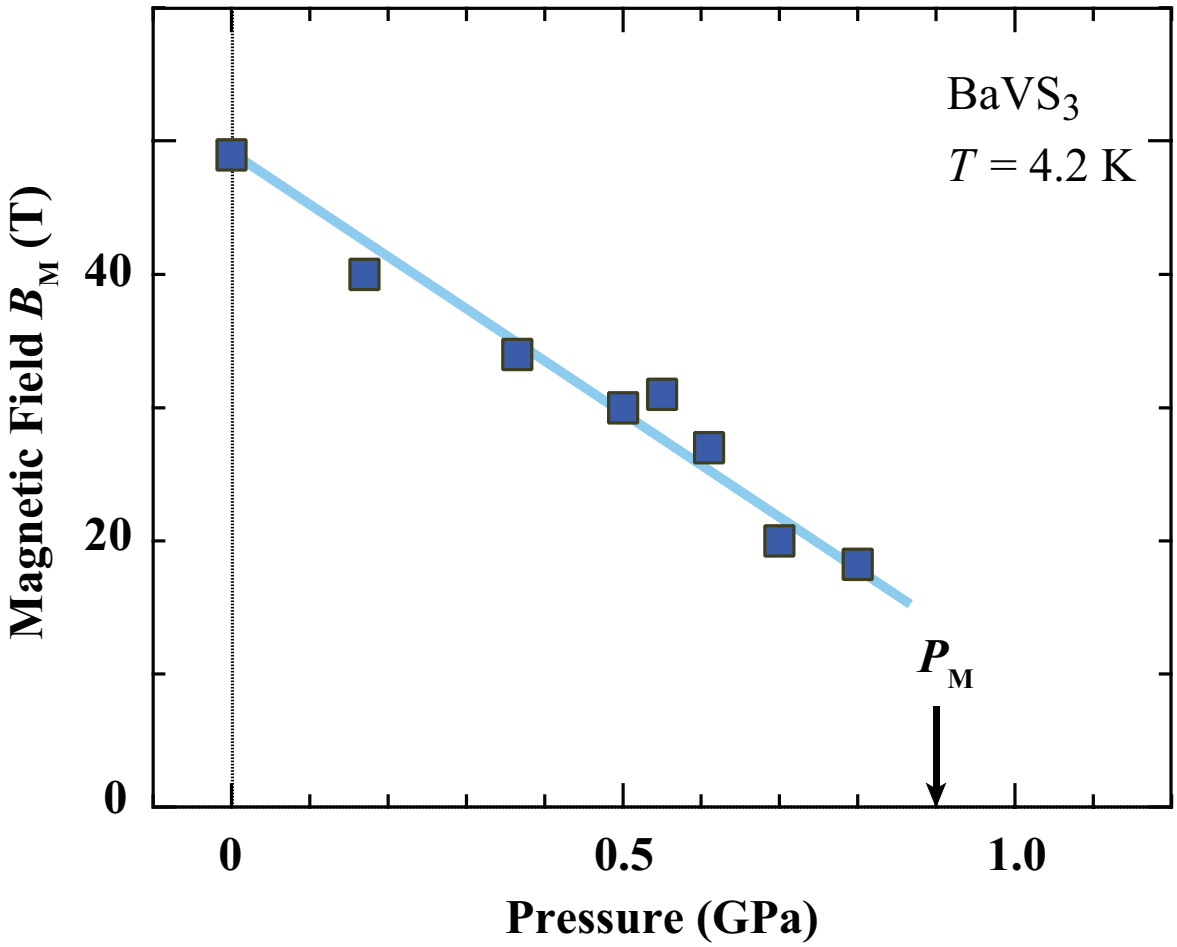

Figure 3.4: Pressure-magnetic field (p-B) phase diagram constructed by metamagnetic transition field B_{M} data of $BaVS_3$ at 4.2 K. The critical pressure of metamagnetic transition p_{M} are shown by black arrow.

3.2.2 Critical pressure for metamagnetic transition

We defined the critical pressure for metamagnetic transition p_{M}. We have two options. That is,

- Pressure at which the extrapolated line of B_{M} becomes 0 T
- Minimum pressure where metamagnetic transition was no longer observed

B_{M} below 0.80 GPa can be described as a linear function of pressure;

$$B_{\mathrm{M}}(p) = -41.0 \times p + 50(T) \tag{3.1}$$

When this equation is applicable, B_{M} is expected to be 13 T at 0.90 GPa. Here we show in Fig. 3.5 all the magnetization curves at 4.2 K measured under different pressures and the magnetization curve calculated by the Brillouin function .The magnetization curve at 0.90 GPa shows a significantly different behavior from that of 0.80 GPa even in a low magnetic field region below 13 T. We emphasized this fact and defined p_{M} as 0.90 GPa.

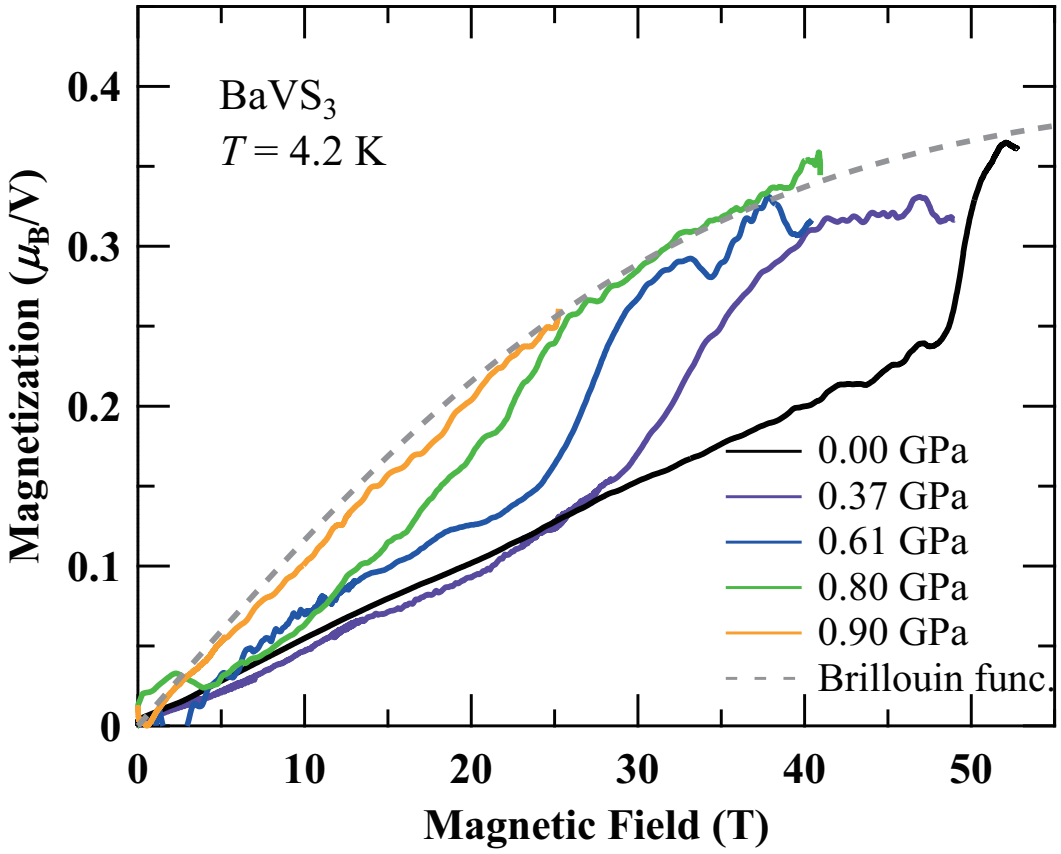

Figure 3.5: Magnetization curves under designated pressures and their analysis by the Brillouin function with ($J = 0.2$, $T_{\mathrm{eff}} = 18$ K, $g = 2$) (dotted line).

3.2.3 Paramagnetic-like behavior at $B>B_{\mathrm{M}}$ and/or $p>p_{\mathrm{M}}$

In order to clarify the magnetic state above the metamagnetic transition field, we analyze the magnetization curves. It turns out that magnetization curves at $B>B_{\mathrm{M}}$ asymptotically approach the Brillouin function;

$$M = Ng\mu_{\mathrm{B}} J \cdot B_J(x) \tag{3.2}$$

$$B_J(x) = \frac{2J+1}{2J}\coth\left(\frac{2J+1}{2J}x\right) - \frac{1}{2J}\coth\left(\frac{1}{2J}x\right) \tag{3.3}$$

$$x = \frac{g\mu_{\mathrm{B}} JH}{k_{\mathrm{B}} T_{\mathrm{eff}}}, \tag{3.4}$$

where J means an angular momentum quantum number, N is the number of magnetic ions, g is the g-factor, μ_{B} represents the Bohr magnetron, and k_{B} is the Boltzmann constant, T_{eff} shows effective temperature including molecular field interaction. From the fitting, we obtained the parameters as $J = 0.2$, $T_{\mathrm{eff}} = 18$ K,and $g = 2$. (See Fig. 3.5)

The Brillouin function well describes the magnetization curve of a paramagnet. Namely, the magnetic state in this region is close to be a paramagnetic state. This is in good agreement with the fact that metamagnetism is observed even at a temperature sufficiently higher than T_{N}. The metamagnetic transition in $BaVS_3$ is essentially equivalent to the transition from a paramagnetic (or nonmagnetic) state to paramagnetic state, and one might suspect that the spin gap opened at T_{MI} was collapsed by the magnetic field B_{M}. However, the obtained parameter $J = 0.2$ corresponds to about 40 % of $3d^1$ magnetic moment, that is a completely different value $J = 0.3$ determined from effective Bohr magnetron for the paramagnetic state at $T > T_{\mathrm{MI}}$, even if we consider the splitting of the spin state of two-site vanadium (in the next section). We believe that this plateau is a type of forced ferromagnetic state in which 67 % of the magnetic moments compared to that in high-temperature paramagnetic region are aligned by magnetic field.

3.3 Magnetic susceptibility

Next, we show the temperature dependence of magnetic susceptibilities at different pressures in Fig. 3.6. We observed a peak at $T_{\mathrm{MI}} \sim 70$ K at ambient pressure (0.00 GPa), which is good agreement with that in previous report[21]. For $T > T_{\mathrm{MI}}$, all the magnetic susceptibilities under different pressures obey the Curie-Weiss law with the same constants as those at ambient pressure ($p_{\mathrm{eff}} \sim (1.28 \pm 0.03)\ \mu_{\mathrm{B}}$, $\Theta_{\mathrm{W}} \sim (8.0 \pm 3.5)$ K), where p_{eff} and Θ_{W} represents effective Bohr magnetron and Weiss temperature, respectively. This result means that the magnitude of the magnetic exchange interaction and localized moment of this material does not change with pressure, which is good agreement with the discussion given by high-field magnetization. The non-trivial value $(1.28 \pm 0.03)\ \mu_{\mathrm{B}}$ of p_{eff} is characteristic of metallic magnetism. In this case, the high-temperature paramagnetism of this substance can be quantitatively evaluated from the $p_{\mathrm{eff}}$and obtain $J = 0.3$ $g = 2$, resulting in that only 60-65% of $3d^1$ electrons contribute to the magnetism of $BaVS_3$.

In addition, we found that the T_{N} hardly changes by applying pressure. We also found a small shoulder-like anomaly around $T_{\mathrm{a}} = 60$ K at ambient pressure, which was not reported so far.

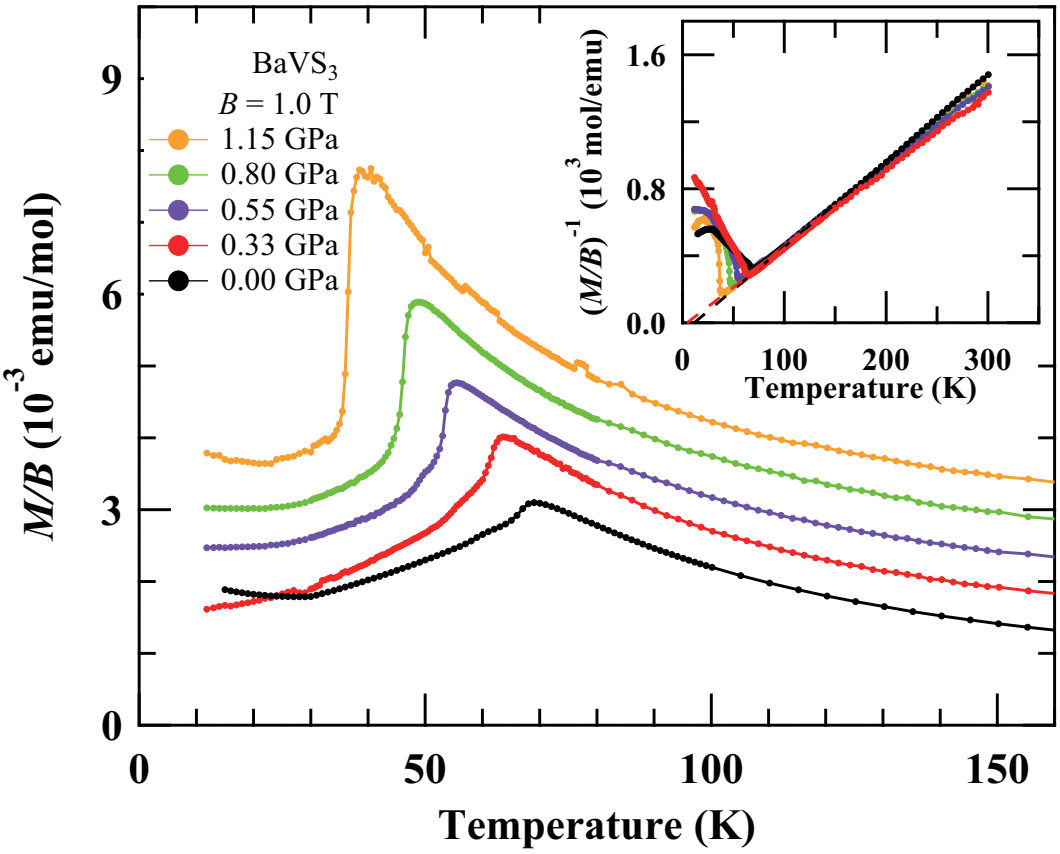

Figure 3.6: Temperature dependences of magnetic susceptibility M/B at 1.0 T under designated pressures. The data under each pressure is shifted upward so that the systematic changes are easy to see. The inset shows the inverse susceptibility $(M/B)^{-1}$. The dashed line indicates the Curie-Weiss law with maximum/minimum slope for $T >$ 100 K.

3.4 Analysis of magnetic susceptibility

3.4.1 Two spin gap analysis

To enhance the shoulder-like anomalies in magnetic susceptibility, we demonstrate the temperature derivative of magnetic susceptibility $\mathrm{d}(M/B)/\mathrm{d}T$ in Fig. 3.7. The temperature profile can be reproduced by a superposition of two Gaussian functions I_{MI} and I_a with the background function $f_{BG}(T)$ defined as follows;

$$f_{BG}(T) = \begin{cases} -A_1/T^2 + A_0 \ (T > T_{\mathrm{MI}}) \\ -\frac{A_2}{T_{\mathrm{MI}}} \cdot \tanh \frac{T-(T_{\mathrm{MI}}-\Delta T)}{2\Delta T} + A_3 \cdot T + A_0 \ (T < T_{\mathrm{MI}}), \end{cases} \tag{3.5}$$

where ΔT is the difference in peak temperature between M/B and $\mathrm{d}(M/B)/\mathrm{d}T$. A_1 stands for the Curie constant, A_2 is a coefficient that indicates the drop of the magnetization due to a gap formation, and A_3 shows a coefficient that the magnetic susceptibility decreases with the square of temperature, indicating a gradual gap formation. The same coefficients A_0, A_1, A_2 and A_3 were used for all the analysis of magnetic susceptibilities under different pressures. We believe that these coefficients should be associated with the magnitude of the local magnetic moment and the strength of the magnetic correlation, and hence some sort of magnetic properties of $BaVS_3$ are hardly affected by pressure, which is in good agreement with all our results.

Given that the peak I_{MI} corresponds to the formation of a spin gap, we thought that the peak I_{a} also indicates the formation of another spin gap. We found that the height of both Gaussian peaks increases with increasing pressure and their widths are almost constant up to 0.70 GPa and completely disappears at 0.90 GPa. From this temperature dependence, we defined 0.90 GPa as a critical pressure, which is in good agreement with p_{M} defined from the metamagnetic transition. Accordingly, we conclude that the metamagnetic transition somehow relates to the spin gap formation at T_{a}.

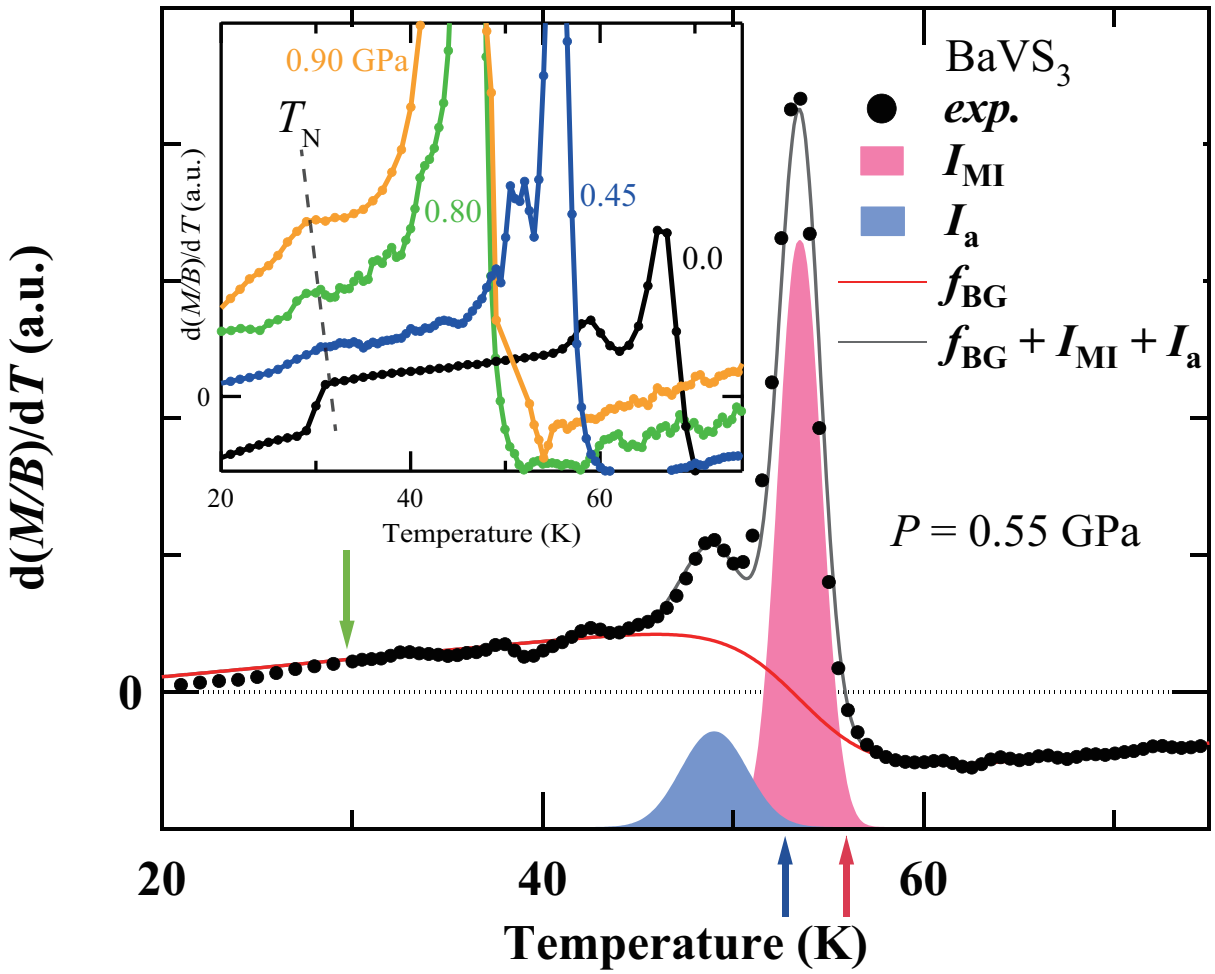

Figure 3.7: The temperature derivative of magnetic susceptibility $\mathrm{d}(M/B)/\mathrm{d}T$. The analysis at 0.55 GPa is shown as a typical example. Red, blue and green arrows represent T_{MI}, T_{a} and T_{N}, respectively. We defined T_{MI}, T_{a} as the temperature at their higher side representing 10% of the peak height of I_{MI}, I_{a}, respectively. The filled circles represent the experimental data, and the solid line represents the fitting curve. Colored areas show Gaussian fitting profiles. The inset show the pressure dependence of $\mathrm{d}(M/B)/\mathrm{d}T$. I_{a} exists up to 0.80 GPa and is not confirmed at 0.90 GPa. The dotted line represents anomalies related to magnetic ordering temperature T_{N}.

3.4.2 Pressure-Temperature(p-T) phase diagram

We draw the p-T phase diagram in Fig. 3.8 as pressure dependences of ($T_{\rm MI}$,$T_{\rm a}$,$T_{\rm N}$) from the magnetic susceptibility. The $T_{\rm MI}$ shows the linear pressure dependence at least below 1.15 GPa, which is the same tendency against pressure as in the previous electrical resistivity measurements[25]. $T_{\rm N}$ is almost constant in this pressure range, which is consistent with the results in recent μSR experiments under high pressure[38]. $T_{\rm a}$ as a function of pressure is almost parallel to the slope of $T_{\rm MI}$ up to 0.80 GPa.

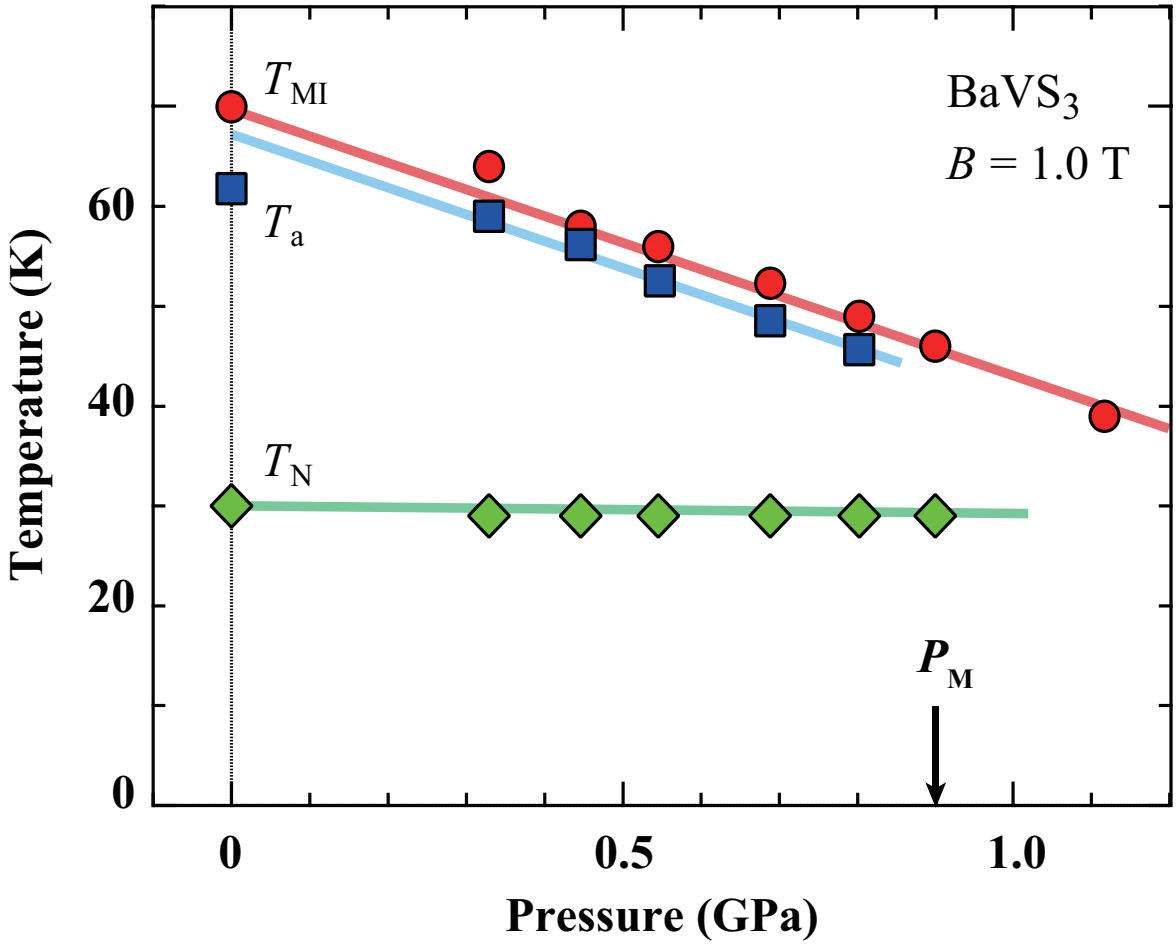

Figure 3.8: p-T phase diagram constructed by the Néel temperature $T_{\rm N}$ (rhombuses), the metal-to-insulator transition temperature $T_{\rm MI}$ (circles), and the anomaly temperature $T_{\rm a}$ (squares) of $BaVS_3$ measured at 1.0 T. The critical pressure $p_{\rm M}$ where $T_{\rm a}$ disappears is shown by arrow in figure.

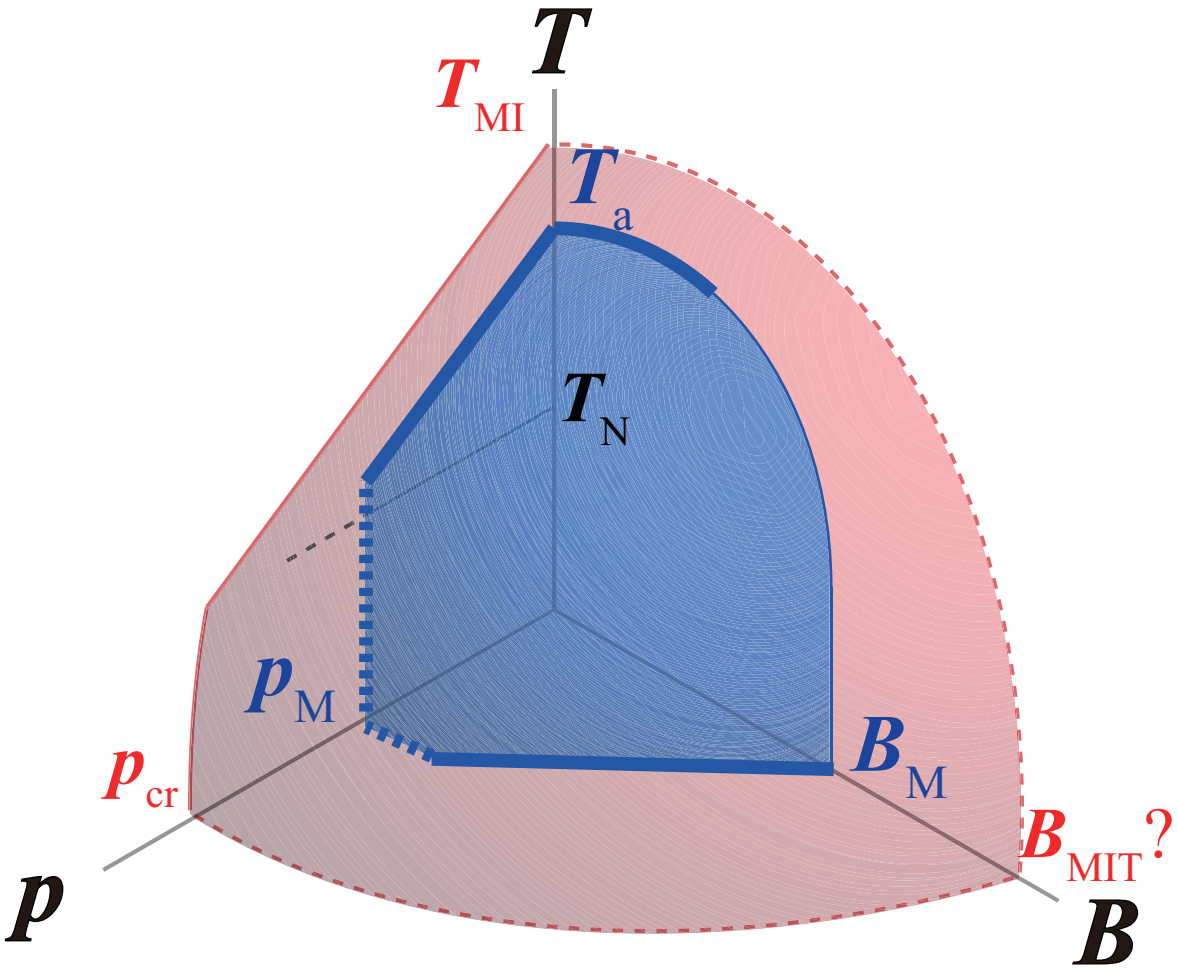

Figure 3.9: Schematic view of Pressure-Magnetic field-Temperature phase diagram in $BaVS_3$. Solid lines are phase boundaries determined from experimental results, dashed lines are expected phase boundaries. We expect the appearance of B_{MIT} at extremely high magnetic field, where the MI transition is completely suppressed by a magnetic field.

3.5 p-B-T phase diagram

From phase diagrams in 3.2.1, 3.4.2, and the B-T phase diagram obtained in the previous study[30],we made a schematic view of the p-B-T phase diagram as in Fig. 3.9. According to both pressure dependences of the magnetic susceptibilities and the high-field magnetizations, we conclude that the B_{M}, T_{a}, and p_{M} belong to the same phase boundary and the new phase is realized inside the expected phase boundary constructed out of T_{MI}, p_{cr}, and B_{MIT}. We expect the appearance of B_{MIT} at extremely high magnetic field, where the MI transition is completely suppressed by a magnetic field. From this phase diagram, two kinds of spin gaps (Δ_{MI}, Δ_{a}) open in $BaVS_3$ and each gap has its individual critical pressure where the gaps close at different pressures, namely p_{cr} and p_{M}.

4 Discussion: Origin of spin gap Δ_a

4.1 Outcome of this study and related previous discussion

The outcome of this study consists of the following interesting points: (I). The existence of two spin gaps (Δ_a and Δ_{MI}) with different energy scales below T_{MI}, (II). The Weiss temperature and the Curie constant hardly changes with increasing pressure even though B_M changes drastically, (III). T_{MI}, T_a and B_M show linear pressure dependences in the low pressure region, but only T_a and B_M disappear at p_M, (IV). Magnetization curves above B_M are asymptotic to 0.4 μ_B/V, which is lower than the expected saturation magnetization value of about 0.6 μ_B/V, (V). The critical pressure of metamagnetic transition ($p_M \sim 0.9$ GPa) is considerably smaller than the critical pressure ($p_{cr} \sim 2.2$ GPa) for the MI transition and/or Lifsitz point, where coherent-incoherent CDW transition occurs (see Fig. 1.11). These findings support that Δ_a has a different origin from Δ_{MI}.

Before discussing the nature of Δ_a, we should describe the previous important arguments. The energy gaps related to the MI transition (including Δ_{MI}) opens in the A_{1g} band mainly due to the Peierls instability and continues to open in a magnetic field range $B > B_M$ at ambient pressure [21, 30, 36]. From the XRD measurements under high pressure[23], Δ_a is not accompanied by a crystallographic symmetry breaking at least low-field and high-pressure region around p_M. It should be noted that, to our knowledge, no experimental result positively shows the valence distribution of vanadium ions and/or spatial spin modulation at $T_N < T < T_{MI}$, except for the Peierls-like transition at T_{MI}.[39, 35, 36] The orbital order model discussed in previous studies contradicts this point. We show a schematic diagram of the orbital order model (Fig. 4.1) and the effect of external parameters (Fig. 4.2).

In order to understand the magnetism of $BaVS_3$, it seems necessary to consider itinerancy. The key here is, "Which bands have itinerant properties." Theoretical calculations based on LDA + DMFT show that the E_g bands that overlap in the *ab* plane are itinerant bands.[20] On the other hand, the Peierls-like transition observed in experimental studies is a characteristic of one-dimensional metal, so that the A_{1g} orbital connected along the *c*-axis seems to be itinerant. Since it is not possible to determine which situation is correct from the current information, we considered the possible origins of Δ_a in each situation. In other words, we propose "model A, where the E_g bands are itinerant" and "model B, where the A_{1g} orbitals are itinerant."

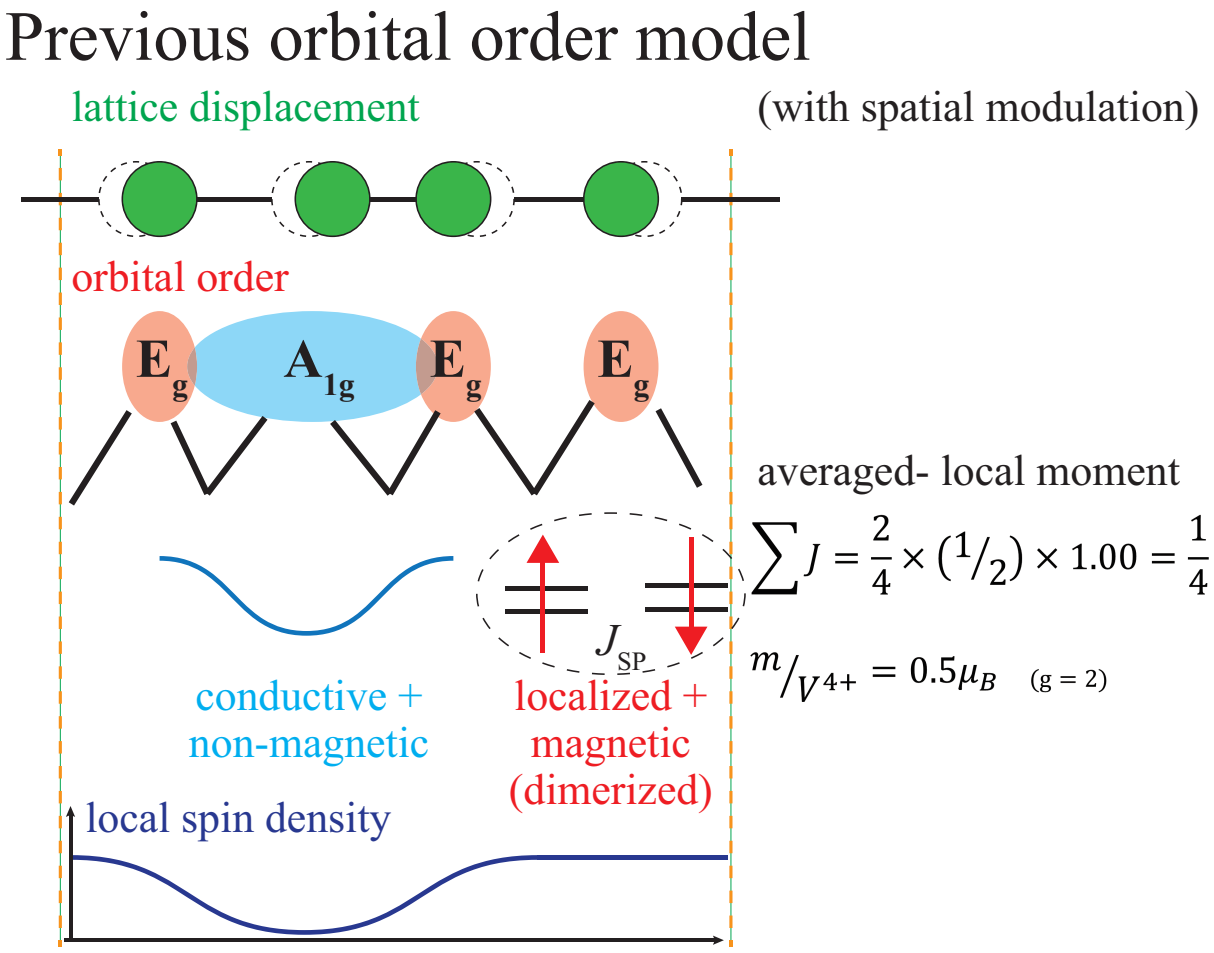

Figure 4.1: Schematic view of orbital order model in previous discussions.

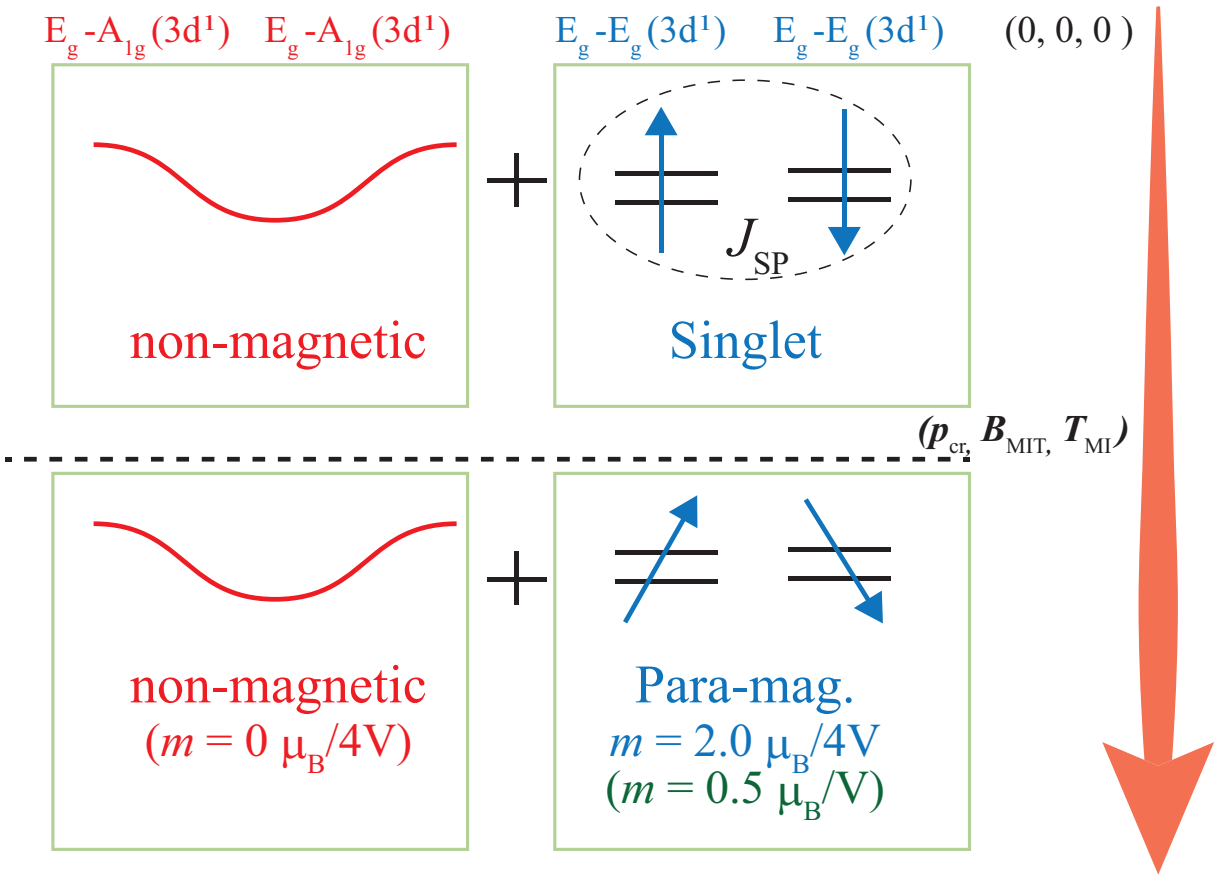

Figure 4.2: External parameter effect on orbital order model.

4.2 Model A: c-d hybridization

Model A is a c-d hybridization model, which is a hybridization between conduction (itinerant) electron and localized d-electron, resulting in on-site spin reduction. We show a schematic view of electronic state in model A (Fig. 4.3) and external field effect (Fig. 4.4)

Although there is no clear evidence for the heavy fermion-like behavior, in reality, the vanadium oxide LiV_2O_4 exhibits heavy fermion behavior due to the hybridization between the narrow A_{1g} band and the broad and itinerant E_g band. This kind of dual nature of d-electrons in LiV_2O_4 is possible because the occupation numbers of d-electrons per V ion is $n_d \sim 1.5$, i.e., $n_{A_{1g}} \sim 1.0$ and $n_{E_g} \sim 0.5$.[37, 40] On the other hand, in the present case, the V ion is occupied only nearly one electron, i.e., $n_d \sim 1.0$, so that such a dual nature is at first sight impossible. However, according to the theoretical calculation based on LDA+CDMFT,[20] the spectral weight of A_{1g} state extends below the Fermi level (FL) down to -2eV giving the occupation about $n_{A_{1g}} \simeq 0.6$, while that of E_g states exhibits the sharp peak around the FL with $n_{E_g} \simeq 0.4$ below the FL as seen in Fig. 7 of Ref. [20]. The former contribution may be regarded as the localized one and the latter as the itinerant one, which is a variant of the itinerant-localized duality discussed in Ce-based heavy fermion metals in Ref. [41]. Nevertheless, according to the specific heat measurement of the present system, the Sommerfeld constant is $\gamma \sim 15.7\,\mathrm{mJ/K^2\,mole\,V}$[24] which corresponds to the effective mass $m^* \sim 7m$[36]. In this sense, the experimental separation of itinerant-localized component is not so clear, which is in consistent with theoretical calculations. Furthermore, there is another problem with a physical picture based on the Kondo effect: $BaVS_3$ exhibits a metamagnetic transition with large hysteresis. There is usually no hysteresis when breaking the Kondo effect of a single magnetic ion by the magnetic field.[42] However, the first order metamagnetic transition is possible also in the lattice system with negative contribution in the 4-th order term of the Landau free energy which is realized if the second derivative of the renormalized density of states of quasi-particles at the Fermi level.

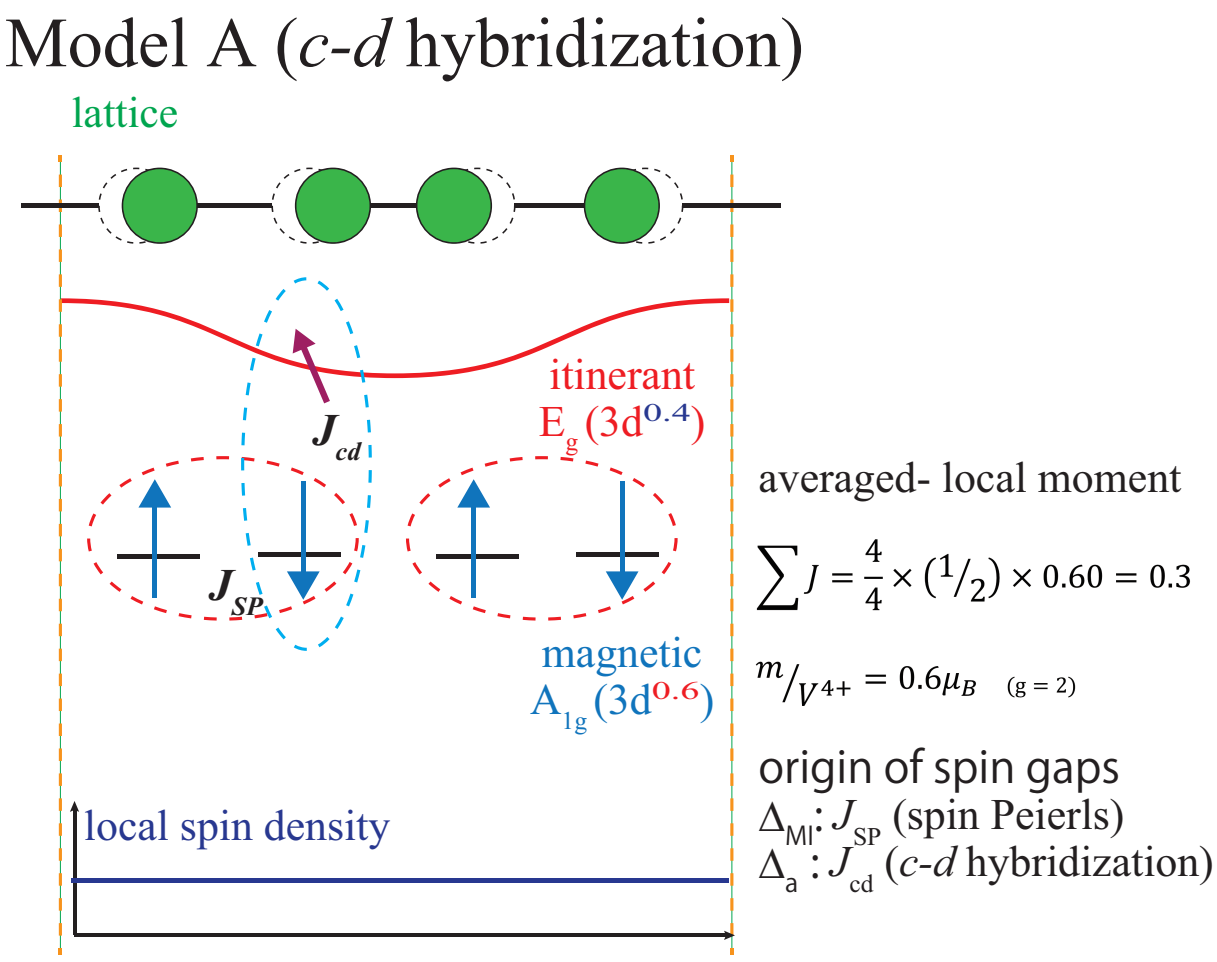

Figure 4.3: Schematic view of model A: *c-d* hybridization and Peierls transition.

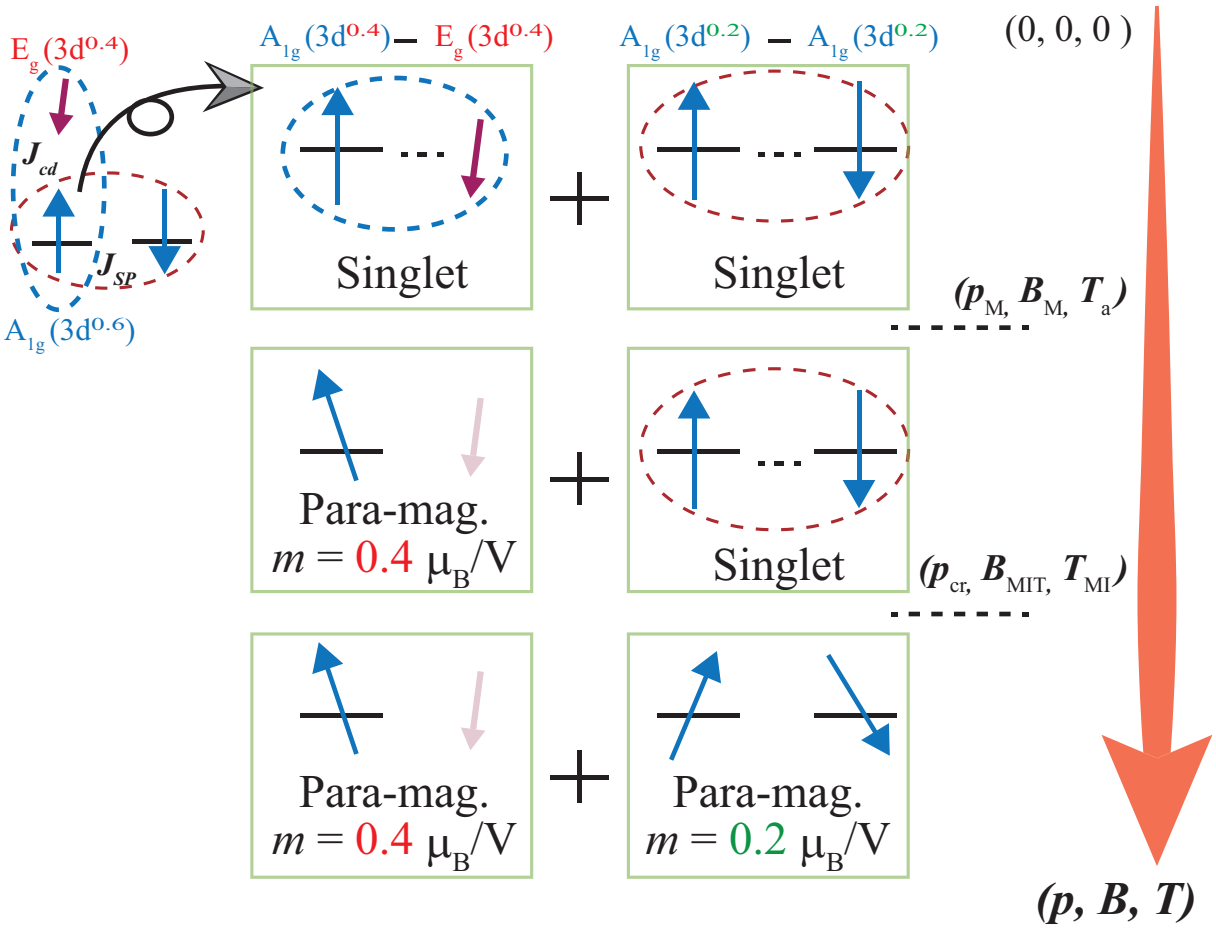

Figure 4.4: External parameter effect on model A.

4.3 Model B: multiple spin Peierls-like transitions

Model B is multiple spin Peierls-like transitions of localized moment in two E_g bands. We show a schematic view of electronic state in model B (Fig. 4.5) and external parameter effect (Fig. 4.6)

Electrons in almost degenerate E_{g1} and E_{g2} orbitals behave as localized magnetic moments and hybridize with itinerant electrons in A_{1g} orbitals. The Peierls transition at T_{MI} makes an electronic gap in the A_{1g} orbital, and at the same time a spin gap Δ_{MI} opened in the E_{g2} orbital. On the other hand, another spin gap Δ_a in the E_{g1} orbital forms at T_a. The difference in transition temperature depends on the difference in the strength of spin-orbit or spin-lattice coupling in each orbital. At $P = P_M$, the local magnetic moment in E_{g1} orbital behaves as spin-liquid by reaching a certain quantum critical point under pressure, and the magnetic moment is partially restored. Then magnetic moment in both $E_{g1}$and E_{g2} orbitals are recovered and show the anti-ferro quantum critical point at p_{cr}.

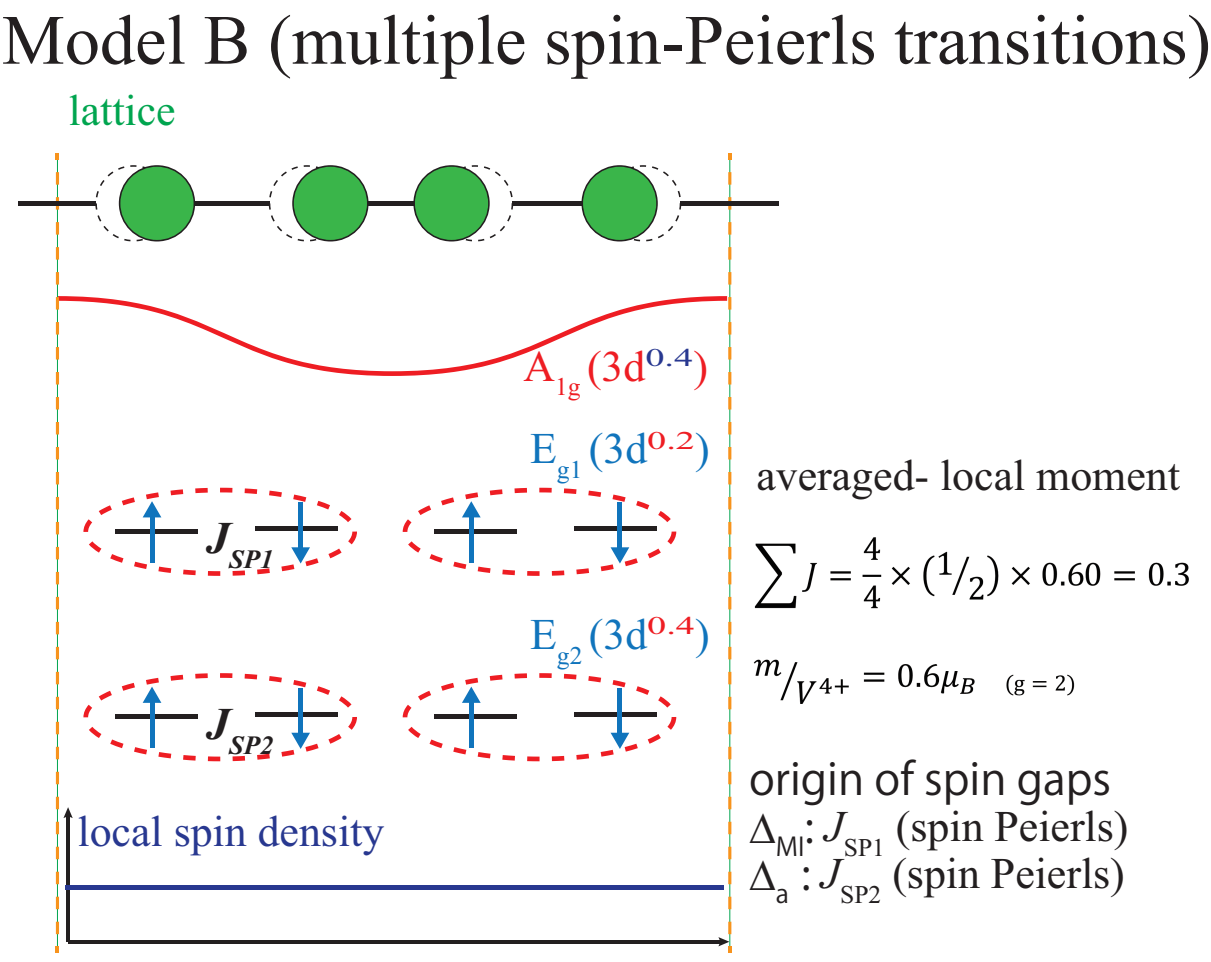

Figure 4.5: Schematic view of model B: multiple Peierls transition.

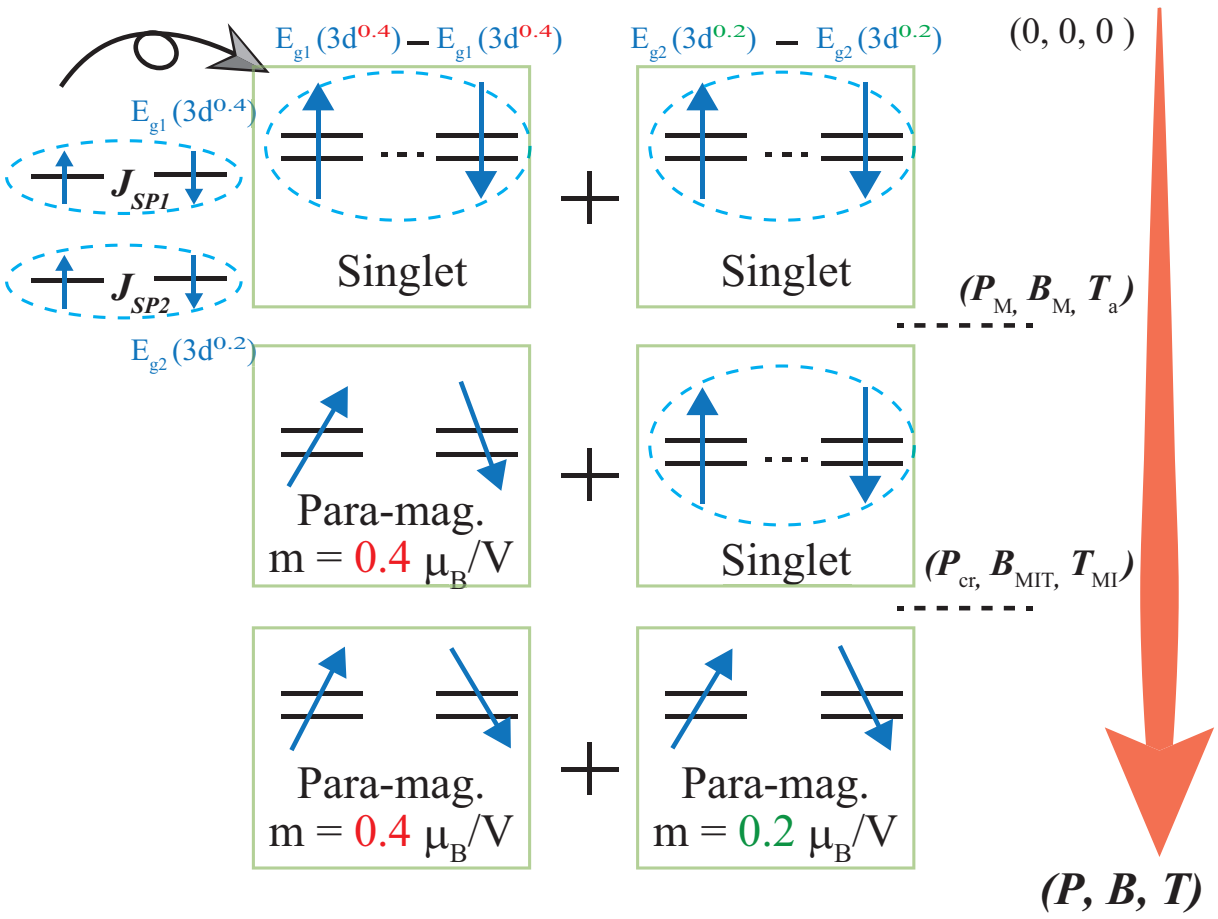

Figure 4.6: External parameter effect on model B.

5 Conclusions

In conclusion, we have performed magnetic measurements of $BaVS_3$ under high pressure. An anomaly in magnetic susceptibility at T_a was found, and the results revealed the relationship between the anomaly and metamagnetic transition at B_M. We concluded a new phase boundary, p_M-B_M-T_a in p-B-T phase diagram. We discuss the origin of spin gap formations and propose two new model explaining the magnetic properties. We summarize our models in Table. 1. These two models are consistent with most experimental findings. Specific heat measurements in high magnetic fields and/or under high pressure provide decisive evidence for these two models. In case of model A, the Sommerfeld constant γ will decrease in the range of $B > B_M$ and/or $p > p_M \sim 0.90$ GPa, and that for model B will increase. To obtain further knowledge about the magnetic phase diagram of $BaVS_3$, direct observation of B_{MIT} is desired . We have shown that the combination of high pressure and high magnetic fields can provide a new insight of the origin of the metal-insulator transition system in $BaVS_3$.

	Δ_{MI} at (T_{MI}, B_{MIT}, p_{cr})	Δ_a at (T_a, B_M, p_M)	
origin	Peierls transition	Kondo effect	Peierls transition
orbital	$A_{1g} + E_g$	$A_{1g} + E_g$	$A_{1g} + E_{g2}$
structural transition	○	×	△
specific heat	bT^3	$\gamma T + bT^3$	bT^3

Table 5.1: Summary of our discussions: Δ_{MI} related to main component of the MI transition opens in $A_{1g} + E_{g1}$ orbitals caused by Peierls transition. There must be another gap formation of Δ_a, according to the mechanism described in models A (Kondo effect, Δ_a opens in $A_{1g} + E_g$ orbital) and model B (Peierls transition, Δ_a opens in $A_{1g} + E_{g2}$ orbital)

Appendix I

In this appendix, I show the *igor* program macro for the estimation of magnetic susceptibility with .dc.raw data obtained by MPMS. This calculation macro arbitrarily masks a part of the measurement data points and calculates the magnitude of the magnetization and the error between the analysis parameters, similarly to the normal DC measurement using MPMS. This macro includes three types of magnetization calculation methods.

```
#pragma rtGlobals=1

macro MPMS_dataload()

Menu "Functions"
FunctionList("*",";","KIND:2,NPARAMS:0")
End

macro initialize()
Load_Raw()
end macro

function Load_Dat()
LoadWave/G/D/N/L={0,0,0,1,3} ;rename wave0, Field_T; rename wave1,
Temperature_K; rename wave2, LongMoment_emu
LoadWave/G/D/N/L={0,0,0,6,1} S_path+S_filename;rename wave0, LongRegFit
end

function Load_Raw()
LoadWave/G/D/N/L={0,0,0,1,2} ;rename wave0, Field_raw;
rename wave1, Temperature_raw
LoadWave/G/D/N/L={0,0,0,6,1} S_path+S_filename;rename wave0, Position_raw
LoadWave/G/D/A/L={0,0,0,15,1} S_path+S_filename; rename wave0, LongResponse_raw
LoadWave/G/D/A/L={0,0,0,18,1} S_path+S_filename; rename wave0, LongResponse_BGsub
end


Function ThreeGauss(pa, x)
wave pa
variable x
return pa[0]+pa[1]*x+
pa[2]*exp(-((x-pa[3])/pa[4])^2)
-pa[2]/2*exp(-((x-pa[3]-pa[5])/pa[4])^2)
-pa[2]/2*exp(-((x-pa[3]+pa[5])/pa[4])^2)
end

macro test()
silent 1;pauseupdate
variable poi1 = 64 //point_per_scan
```

```
variable num1 //total_nomber_of_scans
variable basescan = 70 //88 //what number's scan to base on
variable tempnow
num1 = Dimsize(LongResponse_BGsub,0)/poi1
//print num1
make/O/N = (num1) y0,y1,A,x0,delta,distance,d_y0,d_y1,d_A,d_x0,d_delta,
d_distance,field_T,temp_K,M_emu,dM_emu,
make/O/N = (poi1) field0, temp0, posi0, long0
field0 = Field_raw[x+poi1*basescan]
temp0=Temperature_raw[x+poi1*basescan]
posi0=Position_raw[x+poi1*basescan]
long0=LongResponse_BGsub[x+poi1*basescan]
WaveStats/R=(0,(poi1)) temp0
tempnow = V_avg
//long0=LongResponse_raw[x+0]
Display /W=(55,20,807,505) long0 vs posi0
ModifyGraph rgb=(52224,0,0)
ModifyGraph mode=3,marker=19
ModifyGraph tick=2
ModifyGraph zero=2
ModifyGraph mirror=1
ModifyGraph font="Times"
ModifyGraph minor=1
ModifyGraph fSize=12
ModifyGraph fStyle=1
ModifyGraph standoff=0
Label left "\\F'Times'\\Z16\\f01long0"
Label bottom "\\F'Times'\\Z16\\f01posi0"
Cursor A long0 0; Cursor B long0 (poi1)
ShowInfo
ThreeGaussfit()

AppendToGraph fit_long0
ModifyGraph lsize(fit_long0)=2,rgb(fit_long0)=(0,0,65280)
print tempnow
end macro


macro run()
variable i
variable poi1 = 64 //point_per_scan
variable num1 //total_nomber_of_scans
num1 = Dimsize(LongResponse_raw,0)/poi1

silent 1;pauseupdate
do
i+=1
```

```
field0 = Field_raw[(x+poi1*(i-1))]
temp0=Temperature_raw[(x+poi1*(i-1))]
posi0=Position_raw[(x+poi1*(i-1))]
long0=LongResponse_BGsub[(x+poi1*(i-1))]
//long0=LongResponse_raw[(x+poi1*(i-1))]

ThreeGaussfit()
y0[i-1] = W_coef[0]
y1[i-1] = W_coef[1]
A[i-1] = W_coef[2]
x0[i-1] = W_coef[3]
delta[i-1] = W_coef[4]
distance[i-1] = W_coef[5]
d_y0[i-1] = W_sigma[0]
d_y1[i-1] = W_sigma[1]
d_A[i-1] = W_sigma[2]
d_x0[i-1] = W_sigma[3]
d_delta[i-1] = W_sigma[4]
d_distance[i-1] = W_sigma[5]

field_T[i-1] = field0[0]
WaveStats/R=(0,(poi1)) temp0
temp_K[i-1] = V_avg
M_emu[i-1] = A[i-1]*1.825/(0.002*8589*0.9125)//係数確認
dM_emu[i-1] = d_A[i-1]*1.825/(0.002*8589*0.9125)//係数確認
//fitting[i-1]=
while(i<=num1-1)


Display /W=(55,20,807,505) M_emu vs temp_K
ModifyGraph rgb=(52224,0,0)
ModifyGraph tick=2
ModifyGraph zero=2
ModifyGraph mirror=1
ModifyGraph font="Times"
ModifyGraph minor=1
ModifyGraph fSize=12
ModifyGraph fStyle=1
ModifyGraph standoff=0
ErrorBars M_emu Y,wave=(dM_emu,dM_emu)
AppendToGraph M_emu vs temp_K
ModifyGraph tick=2
Label left "\\F'Times'\\Z16\\f01Magnetization(emu)"
Label bottom "\\F'Times'\\Z16\\f01Temperature(K)"

Differentiate M_emu/X=temp_K/D=M_emu_DIF
Duplicate/O M_emu_DIF,M_emu_DIF_smth;DelayUpdate
```

```
Smooth/B 5, M_emu_DIF_smth
end macro

function ThreeGaussfit()
make/D/N=6/O W_coef
W_coef[0] = {0,0,0.01,5.2,1,1.5}
//W_coef[0] = {0,0,0.01,5.5,1,2} for susceptibility on BaVS3
FuncFit/NTHR=0/TBOX=768 ThreeGauss W_coef long0[pcsr(A), pcsr(B)] /X=posi0 /D

end
```

//////ガウシアン3個による解析用。ほぼうまくいく(a-b-aコイル間の距離をconstとして処理)//////////

```
macro test2()
silent 1;pauseupdate
variable poi1 = 64 //point_per_scan
variable num1 //total_nomber_of_scans
num1 = Dimsize(LongResponse_BGsub,0)/poi1
//print num1
make/O/N = (num1) y0,y1,A,x0,delta,distance,d_y0,d_y1,d_A,d_x0,
d_delta,d_distance,field_T,temp_K,M_emu
make/O/N = (poi1) field0, temp0, posi0, long0
field0 = Field_raw[x+0]
temp0=Temperature_raw[x+0]
posi0=Position_raw[x+0]
long0=LongResponse_BGsub[x+0]
//long0=LongResponse_raw[x+0]

Display /W=(55,20,807,505) long0 vs posi0
ModifyGraph rgb=(52224,0,0)
ModifyGraph mode=3,marker=19
ModifyGraph tick=2
ModifyGraph zero=2
ModifyGraph mirror=1
ModifyGraph font="Times"
ModifyGraph minor=1
ModifyGraph fSize=12
ModifyGraph fStyle=1
ModifyGraph standoff=0
Label left "\\F'Times'\\Z16\\f01long0"
Label bottom "\\F'Times'\\Z16\\f01posi0"
Cursor A long0 0; Cursor B long0 (poi1)
ShowInfo
```

```
ThreeGaussfit2()

AppendToGraph fit_long0
ModifyGraph lsize(fit_long0)=2,rgb(fit_long0)=(0,0,65280)
end macro


macro run2()
variable i
variable poi1 = 64 //point_per_scan
variable num1 //total_nomber_of_scans
num1 = Dimsize(LongResponse_BGsub,0)/poi1

silent 1;pauseupdate
do
i+=1
field0 = Field_raw[(x+poi1*(i-1))]
temp0=Temperature_raw[(x+poi1*(i-1))]
posi0=Position_raw[(x+poi1*(i-1))]
long0=LongResponse_BGsub[(x+poi1*(i-1))]
//long0=LongResponse_raw[(x+poi1*(i-1))]

ThreeGaussfit2()
y0[i-1] = W_coef[0]
y1[i-1] = W_coef[1]
A[i-1] = W_coef[2]
x0[i-1] = W_coef[3]
delta[i-1] = W_coef[4]
distance[i-1] = 2
//distance[i-1] = W_coef[5]
d_y0[i-1] = W_sigma[0]
d_y1[i-1] = W_sigma[1]
d_A[i-1] = W_sigma[2]
d_x0[i-1] = W_sigma[3]
d_delta[i-1] = W_sigma[4]
d_distance[i-1] = W_sigma[5]
field_T[i-1] = field0[0]
WaveStats/R=(0,(poi1)) temp0
temp_K[i-1] = V_avg
M_emu[i-1] = A[i-1]*1.825/(0.002*8589*0.9125)
while(i<=num1-1)

Display /W=(55,20,807,505) M_emu vs temp_K
ModifyGraph rgb=(52224,0,0)
ModifyGraph tick=2
ModifyGraph zero=2
ModifyGraph mirror=1
```

```
ModifyGraph font="Times"
ModifyGraph minor=1
ModifyGraph fSize=12
ModifyGraph fStyle=1
ModifyGraph standoff=0
Label left "\\F'Times'\\Z16\\f01Magnetization(emu)"
Label bottom "\\F'Times'\\Z16\\f01Temperature(K)"

end macro



Function ThreeGauss2(pa, x)
wave pa
variable x
return pa[0]+pa[1]*x+pa[2]*exp(-((x-pa[3])/pa[4])^2)
-pa[2]/2*exp(-((x-pa[3]-2)/pa[4])^2)
-pa[2]/2*exp(-((x-pa[3]+2)/pa[4])^2)
//return pa[0]+pa[1]*x+pa[2]*exp(-((x-pa[3])/pa[4])^2)
-pa[2]/2*exp(-((x-pa[3]-pa[5])/pa[4])^2)
-pa[2]/2*exp(-((x-pa[3]+pa[5])/pa[4])^2)
end



function ThreeGaussfit2()
//make/D/N=6/O W_coef
make/D/N=5/O W_coef
//W_coef[0] = {0,0,0.01,5.5,2,2}
W_coef[0] = {0,0,0.01,5.5,2}
FuncFit/NTHR=0/TBOX=768 ThreeGauss2 W_coef long0[pcsr(A), pcsr(B)] /X=posi0 /D
end



//////文献と同じ評価//////////

Function bunken(pa1, x)
wave pa1
variable x
return pa1[2]*(2*(pa1[3]^2+(x-pa1[4])^2)^(-3/2)
-(pa1[3]^2+(pa1[5]+x-pa1[4])^2)^(-3/2))
-(pa1[3]^2+(-pa1[5]+x-pa1[4])^2)^(-3/2)
+pa1[0]+pa1[1]*x
end

macro test_bunken()
```

```
silent 1;pauseupdate
variable poi1 = 64 //point_per_scan
variable num1 //total_nomber_of_scans
num1 = Dimsize(LongResponse_BGsub,0)/poi1
//print num1
make/O/N = (num1) y0,y1,A,Radius,x0,distance,d_y0,d_y1,d_A,d_x0,
d_Radius,d_distance,field_T,temp_K,M_emu
make/O/N = (poi1) field0, temp0, posi0, long0
field0 = Field_raw[x+0]
temp0=Temperature_raw[x+0]
posi0=Position_raw[x+0]
long0=LongResponse_BGsub[x+0]
//long0=LongResponse_raw[x+0]

Display /W=(55,20,807,505) long0 vs posi0
ModifyGraph rgb=(52224,0,0)
ModifyGraph mode=3,marker=19
ModifyGraph tick=2
ModifyGraph zero=2
ModifyGraph mirror=1
ModifyGraph font="Times"
ModifyGraph minor=1
ModifyGraph fSize=12
ModifyGraph fStyle=1
ModifyGraph standoff=0
Label left "\\F'Times'\\Z16\\f01long0"
Label bottom "\\F'Times'\\Z16\\f01posi0"
Cursor A long0 0; Cursor B long0 (poi1)
ShowInfo
bunkenfit()

end macro


macro run_bunken()
variable i
variable poi1 = 64 //point_per_scan
variable num1 //total_nomber_of_scans
num1 = Dimsize(LongResponse_BGsub,0)/poi1

silent 1;pauseupdate
do
i+=1
field0 = Field_raw[(x+poi1*(i-1))]
temp0=Temperature_raw[(x+poi1*(i-1))]
posi0=Position_raw[(x+poi1*(i-1))]
long0=LongResponse_BGsub[(x+poi1*(i-1))]
```

```
//long0=LongResponse_raw[(x+poi1*(i-1))]

bunkenfit()
y0[i-1] = W_coef[0]
y1[i-1] = W_coef[1]
A[i-1] = W_coef[2]
Radius[i-1] = W_coef[3]
x0[i-1] = W_coef[4]
distance[i-1] = W_coef[5]
d_y0[i-1] = W_sigma[0]
d_y1[i-1] = W_sigma[1]
d_A[i-1] = W_sigma[2]
d_Radius[i-1] = W_sigma[3]
d_x0[i-1] = W_sigma[4]
d_distance[i-1] = W_sigma[5]
field_T[i-1] = field0[0]
WaveStats/R=(0,(poi1)) temp0
temp_K[i-1] = V_avg
M_emu[i-1] = A[i-1]*1.825/(0.002*8589*0.9125)
while(i<=num1-1)

Display /W=(55,20,807,505) M_emu vs temp_K
ModifyGraph rgb=(52224,0,0)
ModifyGraph tick=2
ModifyGraph zero=2
ModifyGraph mirror=1
ModifyGraph font="Times"
ModifyGraph minor=1
ModifyGraph fSize=12
ModifyGraph fStyle=1
ModifyGraph standoff=0
Label left "\\F'Times'\\Z16\\f01Magnetization(emu)"
Label bottom "\\F'Times'\\Z16\\f01Temperature(K)"

end macro

function bunkenfit()
make/D/N=6/O W_coef
//W_coef[0] = {0.001,0,0.5,2,4,-1}
W_coef[0] = {0.0,0.0002,1,2,5.5,-1}
FuncFit/NTHR=0/TBOX=768 bunken W_coef long0[pcsr(A), pcsr(B)] /X=posi0 /D

end
////////////////////////////////////
```

```
////////////ガウシアン1個での解析用。あまりうまくいかない////////////

macro test_gauss()
silent 1;pauseupdate
variable poi1 = 64 //point_per_scan
variable num1 //total_nomber_of_scans
num1 = Dimsize(LongResponse_raw,0)/poi1
//print num1
make/O/N = (num1) y0,y1,A,x0,delta,distance,d_y0,d_y1,d_A,d_x0,
d_delta,d_distance,field_T,temp_K,M_emu
make/O/N = (poi1) field0, temp0, posi0, long0
field0 = Field_raw[x+0]
temp0=Temperature_raw[x+0]
posi0=Position_raw[x+0]
long0=LongResponse_BGsub[x+0]

Display /W=(55,20,807,505) long0 vs posi0
ModifyGraph rgb=(52224,0,0)
ModifyGraph mode=3,marker=19
ModifyGraph tick=2
ModifyGraph zero=2
ModifyGraph mirror=1
ModifyGraph font="Times"
ModifyGraph minor=1
ModifyGraph fSize=12
ModifyGraph fStyle=1
ModifyGraph standoff=0
Label left "\\F'Times'\\Z16\\f01long0"
Label bottom "\\F'Times'\\Z16\\f01posi0"
Cursor A long0 0; Cursor B long0 (poi1)
ShowInfo
Gaussfit()

AppendToGraph fit_long0
ModifyGraph lsize(fit_long0)=2,rgb(fit_long0)=(0,0,65280)
end macro

macro run_gauss()
variable i
variable poi1 = 64
variable num1
```

```
num1 = Dimsize(LongResponse_raw,0)/poi1

silent 1;pauseupdate
do
i+=1
field0 = Field_raw[(x+poi1*(i-1))]
temp0=Temperature_raw[(x+poi1*(i-1))]
posi0=Position_raw[(x+poi1*(i-1))]
long0=LongResponse_BGsub[(x+poi1*(i-1))]

Gaussfit()
y0[i-1] = W_coef[0]
y1[i-1] = W_coef[1]
A[i-1] = W_coef[2]
x0[i-1] = W_coef[3]
delta[i-1] = W_coef[4]
d_y0[i-1] = W_sigma[0]
d_y1[i-1] = W_sigma[1]
d_A[i-1] = W_sigma[2]
d_x0[i-1] = W_sigma[3]
d_delta[i-1] = W_sigma[4]
field_T[i-1] = field0[0]
WaveStats/R=(0,(poi1)) temp0
temp_K[i-1] = V_avg
M_emu[i-1] = A[i-1]*1.825/(0.002*8589*0.9125)
while(i<=num1-1)

Display /W=(55,20,807,505) M_emu vs temp_K
ModifyGraph rgb=(52224,0,0)
ModifyGraph tick=2
ModifyGraph zero=2
ModifyGraph mirror=1
ModifyGraph font="Times"
ModifyGraph minor=1
ModifyGraph fSize=12
ModifyGraph fStyle=1
ModifyGraph standoff=0
Label left "\\F'Times'\\Z16\\f01Magnetization(emu)"
Label bottom "\\F'Times'\\Z16\\f01Temperature(K)"

end macro

Function oneGauss(pa_gauss, x)
wave pa_gauss
variable x
return pa_gauss[0]+pa_gauss[1]*x
+pa_gauss[2]*exp(-((x-pa_gauss[3])/pa_gauss[4])^2)
```

```
end

function Gaussfit()
make/D/N=5/O W_coef
W_coef[0] = {0,0,1,5.5,2}
FuncFit/NTHR=0/TBOX=768 oneGauss W_coef long0[pcsr(A), pcsr(B)] /X=posi0 /D
end


end macro
```

Appendix II

Antiferro-to-Ferro magnetic transition tuned by chemical pressure and/or impurities

One of the great mysteries of $BaVS_3$ is the extraordinarily large impurity effect[43, 44]. In $BaVS_3$, it has been reported that the antiferromagnetic order at $T_N \simeq 30$ K disappears and the ferromagnetic transition at $T_c \simeq 15$K occurs by sulfur deficiency of more than 5% [43] (see Fig.5.1) or substitution of Sr ions at about 7% for Ba ions[44]. The magnetic susceptibility changes upon Sr substitution are shown in Fig. 5.2 , 5.3.

Little is known about the magnetically ordered state of this material, including our work. Although this antiferro-to-ferro magnetic (AF-F) transition is supposed to provide important insights into the determinant of the magnetic state, it seems difficult to prepare replacement sample $Ba_{1-x}Sr_xVS_3$ with high quality. In comparison with our results, this Sr substitution is unlikely to be a simple chemical pressure effect, because the ferromagnetic transition did not occur under hydrostatic pressure.

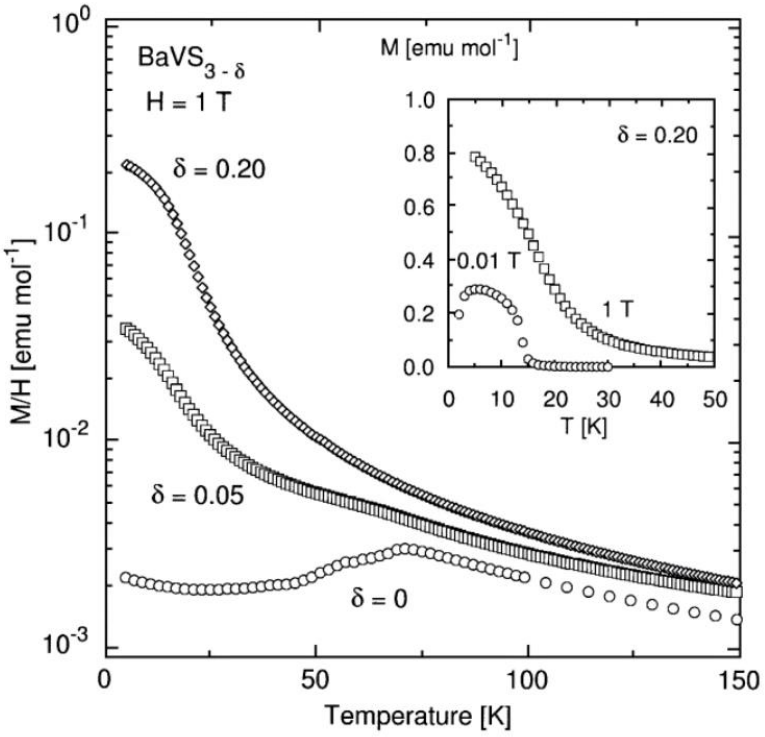

Figure 5.1: Temperature dependence of magnetic susceptibilities of sulfur-deficient $BaVS_{3-\delta}$ samples[43]. The peak in magnetic susceptibility indicating the MI transition does not appear and the ferro-magnetic ordring occurs in $\delta > 0.05$ samples (see also inset: expanded magnetic susceptibility of $\delta = 0.20$sample in low temperature region).

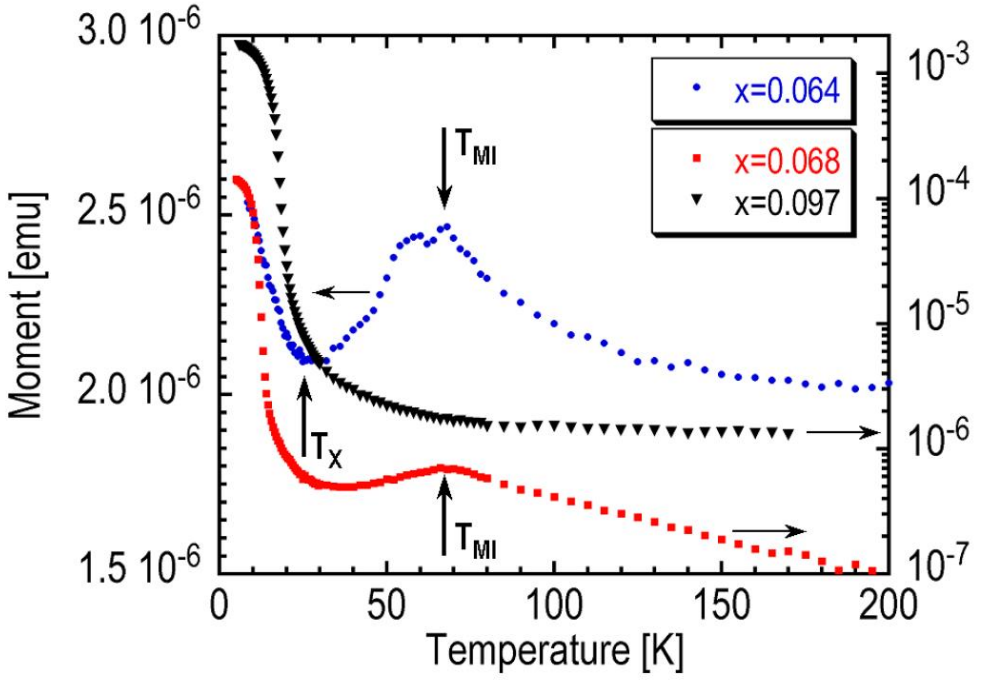

Figure 5.2: Temperature dependence of magnetic susceptibilities of single crystalline $Ba_{1-x}Sr_xVS_3$[44]. The proportion that shows antiferro-magnetism decreases with increasing substitution amount x, and disappear in $x = 0.097$ compounds.

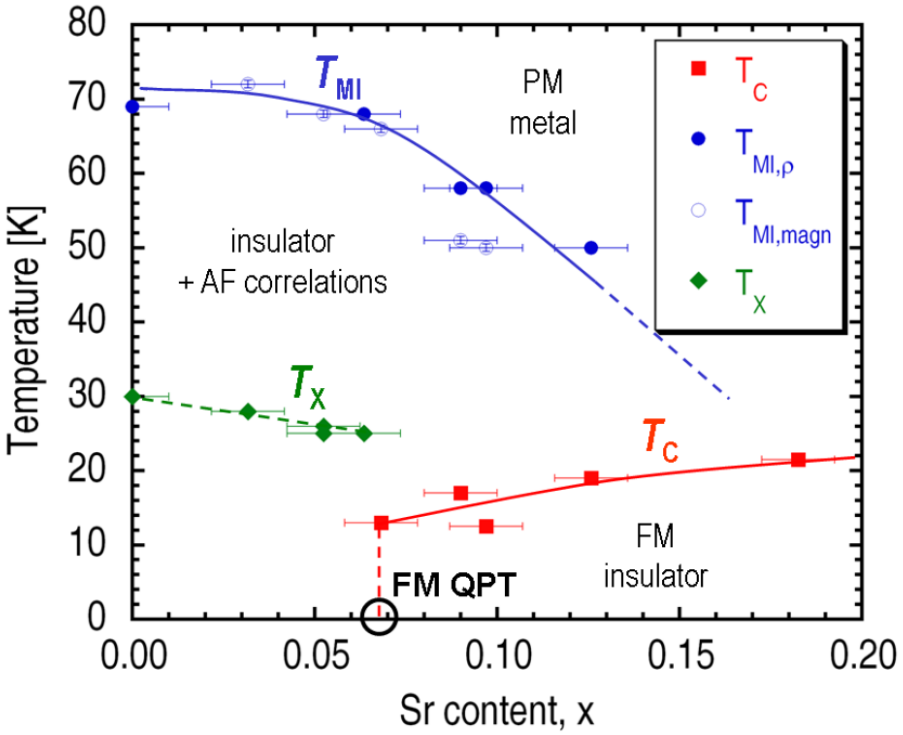

Figure 5.3: Phase diagram of $Ba_{1-x}Sr_xVS_3$ controlled by Sr substitution amount x[44]. The critical point of AF-F transition exists around $x \simeq 0.07$.

References

[1] L. D. Landau and E. M. Lifshitz , *StatisticalPhysics*, Iwanami shoten publisher, (1969).

[2] M. Imada, A. Fujimori, and Y. Tokura, Rev. Mod. Phys., **70**, 1039 (1998).

[3] R. E. Peierls, *Quantum Theory of Solids*, Oxford Press (1955).

[4] J. A. Northby, H. A. Groenendjik, L. J. de Jongh, J. C. Bonner, I. S. Jacobs, and L. V. Interrante, Phys. Rev. B, **25**, 3215 (1982).

[5] F. Wudl, D. E. Schafer, W. M. Walsh, L. W. Rupp, F. J. DiSalvo, J. V. Waszczak, M. L. Kaplan, and G. A. Thomas, J. Chem. Phys., **66**, 377 (1977).

[6] J. Kondo, *The physics of dilute magnetic alloy*, SHOKABO Co., Ltd. (1983).

[7] N. Sato and K. Miyake, *Heavy Fermion Physics : Magetism and Superconductivity*, The University off Nagoya Press, (2013).

[8] S. Gabáni, E. Bauer, S. Berger, K. Flachbart, Y. Paderno, C. Paul, V. Pavlík, and N. Shitsevalova, Phys. Rev. B, **67**, 172406 (2003).

[9] S. Catalano, M. Gibert, J. Fowlie, J. Íñiguez, J-M. Triscone, and J. Kreisel, Rep. Prog. Phys. **81**, 046501 (2018).

[10] H. Fujishiro, T. Fukase, and M. Ikebe, J. Phys. Soc. Jpn.,**67**, 2582 (1998).

[11] J. Hemberger, A. Krimmel, T. Kurz, H. -A.Krug von Nidda, V. Yu. Ivanov, A. A. Mukhin, A. M. Balbashov, and A. Loidl, Phys. Rev. B,**66**, 094410 (2002).

[12] S. Majumdar and S. van Dijken, J. Phys. D: Appl. Phys., **47**, 034010 (2014).

[13] R. Gardner, M. Vlasse, and A. Wold, Acta Crystallogr. Sect. B, **25**, 781 (196p).

[14] H. Kuriyaki, H. Berger, S. Hishioka, H. Kawakami, K. Hirakawa, and F. A. Levy, Synthetic Metals, **71**, 2049 (1995).

[15] G. Mihály, I. Kézsmárki, F. Zamborszky, M. Miljak, K. Penc, P. Fazekas, H. Berger, and L. Forró, Phys. Rev. B, **61**, R7831 (2000).

[16] T. Inami, K. Ohwada, H. Kimura, M. Watanabe, Y. Noda, H. Nakamura, T. Yamasaki, M. Shiga, N. Ikeda, and Y. Murakami, Phys. Rev. B, **66**, 085101 (2007).

[17] M. Ghedira, M. Anne, J. Chenevas, M. Marezio, and F. Sayetat, J. Phys. C, **19**, 6489 (1986).

[18] S. Fagot, P. Foury-Leylekian, S. Ravy, J.-P. Pouget, M. Anne, G. Popov, M. V. Lobanov, and M. Greenblatt, Solid State Sci., **7**, 718 (2005).

[19] M. Takano, H. Kosugi, N. Nakanishi, M. Shimada, T. Wada, and M. Koizumi, J. Phys. Soc. Jpn. L, **43**, 1101 (1977).

[20] F. Lechermann, S. Biermann, and A. Gerges, Phys. Rev. B, **76**, 085101 (2007).

[21] S. Fagot, P. Foury-Leylekian, S. Ravy, J.-P. Pouget, and H. Berger, Phys. Rev. Lett., **90**, 196401 (2003).

[22] H. Sato, K. Tobimatsu, A. Tanaka, H. Nakamura, H. Hayashi, H. Iwasawa, K. Shimada, H. Namatame, and M. Taniguchi, JPS Conf. Proc., **3**, 013015 (2014).

[23] S. Bernu, P. Fertey, J.-P. Itié, H. Berger, P. Foury-Leylekian, and J.-P. Pouget, Phys. Rev. B, **86**, 235105 (2012).

[24] H. Imai, H. Wada, and M. Shiga, J. Phys. Soc. Jpn., **65**, 3460 (1996).

[25] L. Forró, R. Gaál, H. Berger, P. Fazekas, K. Penc, I. Kézsmárki, and G. Mihály, Phys. Rev. Lett., **85**, 1938 (2000).

[26] N. Barišić,doctoral thesis, Ecole Polytechnique Fédérale de Lausanne(EPFL), (2004).

[27] T. Graf, D. Mandrus, J. M. Lawrence, J. D. Thompson, P. C. Canfield, S.-W. Cheong, and L. W. Rupp, Jr., Phys. Rev. B, **51**, 2037 (1995).

[28] H. Nakamura, T. Yamasaki, S. Giri, H. Imai, M. Shiga, K. Kojima, M. Nishi, K. Kakurai, and N. Metoki, J. Phys. Soc. Jpn., **69**, 2763 (2000).

[29] R. A. de Souza, U. Staub, V. Scagnoli, M. Garganourakis, Y. Bodenthin, and H. Berger, Phys. Rev. B, **84**, 014409 (2011).

[30] Y. Narumi, K. Suga, K. Kindo, T. Yamasaki, M. Shiga, and H. Nakamura, J. Phys. Soc. Jpn., **76**, 013706 (2007).

[31] A. Fujitsugu, 高圧力の科学と技術, **12**, 288 (2002).

[32] T. F. Smith and C. W. Chu, Phys. Rev., **159**, 353 (1967).

[33] MPMS MultiVu Application User's Manual, Quantum Design.

[34] M. Shiga, H. Imai, H. Mitamura, and T. Goto, Phys. B: Cond. Matt., **294**, 149 (2001).

[35] S. Fagot, P. Foury-Leylekian, S. Ravy, J.-P. Pouget, É. Lorenzo, Y. Joly, M. Greenblatt, M. V. Lobanov, and Guerman Popov, Phys. Rev. B, **73**, 033102 (2006).

[36] I. Kézsmárki, G. Mihály, R. Gaál, N. Barišić, A. Akrap, H. Berger, L. Forró, C. C. Homes, and L. Mihály, Phys. Rev. Lett. **96**, 186402 (2006).

[37] S. Kondo, D. C. Johnston, C. A. Swenson, F. Borsa, A. V. Mahajan, L. L. Miller, T. Gu, A. I. Goldman, M. B. Maple, D. A. Gajewski, E. J. Freeman, N. R. Dilley, R. P. Dickey, J. Merrin, K. Kojima, G. M. Luke, Y. J. Uemura, O. Chmaissem, and, J. D. Jorgensen, Phys. Rev. Lett, **78**, 3729 (1997).

[38] J. Sugiyama, H. Nakamura, R. Khasanov, D. Andreica, Y. Sassa, O. K. Forslund, E. Nocerino, N. Matsubara, and M. Mansson, 日本物理学会 2019 年秋季大会　概要集 (10pB11-8), 1592 (2019).

[39] V. Ilakovac, M. Guarise, M. Grioni, T. Schmitt, K. Zhou, L. Braicovich, G. Ghiringhelli, V. N. Strocov, and H. Berger, J. Phys., Condens. Matter., **25**, 505602 (2013).

[40] H. Kusunose, S. Yotsuhashi, and K. Miyake, Phys. Rev. B, **62**, 4403 (2000).

[41] Y. Kuramoto and K. Miyake, J. Phys. Soc. Jpn., **59**, 2831 (1990).

[42] P. Haen, J. Flouquet, F. Lapierre, P. Lejay, and G. Remenyi, J. Low Temp. Phys., **67**, 391 (1987).

[43] T. Yamasaki, H. Nakamura, and M. Shiga, J. Phys. Soc. Jpn., **69**, 3068 (2000).

[44] A. Gauzzi, N. Barišić, F. Licci, G. Calestani, F. Bolzoni, P. Fezekas, E. Gilioli, and L. Forró, arXiv:cond-mat/0601286v1.

Publication List

1. "Vanishing Metamagnetic Transition in the Metal-to-Insulator Transition Compound $BaVS_3$ under High Pressure "
   T. Tahara, T. Kida, Y. Narumi, T. Takeuchi, H. Nakamura, K. Miyake, K. Kindo, and M. Hagiwara,
   to be published in JPSJ

2. "Negative and Positive Magnetoresistance in the Itinerant Antiferromagnet $BaMn_2Pn_2$ "
   K-K. Huynh, T. Ogasawara, K. Kitahara, Y. Tanabe, S. Y. Matsushita, **T. Tahara**, T. Kida, M. Hagiwara, D. Arčon, and K. Tanigaki,
   Phys. Rev. B, **99**, 195111 (2019).

3. "De Haas-van Alphen Oscillations for Small Electron Pocket Fermi Surfaces and Huge H-linear Magnetoresistances in Degenerate Semiconductors PbTe and PbS "
   S. Kawakatsu, K. Nakaima, M. Kakihana, Y. Yamakawa, H. Miyazato, T. Kida, **T. Tahara**, M. Hagiwara, T. Takeuchi, D. Aoki, A. Nakamura, Y. Tatetsu, T. Maehira, M. Hedo, T. Nakama, and Y. Ōnuki,
   J. Phys. Soc. Jpn., **88**, 013704 (2018).

4. "Electronic States of Antiferromagnet FeSn and Pauli Paramagnet CoSn "
   M. Kakihana, K. Nishimura, D. Aoki, A. Nakamura, M. Nakashima, Y. Amako, T. Takeuchi, T. Kida, **T. Tahara**, M. Hagiwara, H. Harima, M. Hedo, T. Nakama, and Y. Ōnuki,
   J. Phys. Soc. Jpn., **88**, 014705 (2018).

5. "Effects of Magnetic Field and Pressure on the Valence-Fluctuating Antiferromagnetic Compound $EuPt_2Si_2$ "
   T. Takeuchi, T. Yara, Y. Ashitomi, W. Iha, M. Kakihana, M. Nakashima, Y. Amako, F. Honda, Y. Homma, D. Aoki, Y. Uwatoko, T. Kida, **T. Tahara**, M. Hagiwara, Y. Haga, M. Hedo, T. Nakama, and Y. Ōnuki,
   J. Phys. Soc. Jpn., **87**, 074709 (2018).

6. "Electronic States in $EuCu_2(Ge1-xSi_x)_2$ Based on the Doniach Phase Diagram "
   W. Iha, T. Yara, Y. Ashitomi, M. Kakihana, T. Takeuchi, F. Honda, A. Nakamura, D. Aoki, J. Gouchi, Y. Uwatoko, T. Kida, **T. Tahara**, M. Hagiwara, Y. Haga, M. Hedo, T. Nakama, and Y. Ōnuki,
   J. Phys. Soc. Jpn., **87**, 064706 (2018).

7. "Magnetic Properties and Effect of Pressure on the Electronic State of $EuCo_2Ge_2$ "
   Y. Ashitomi, M. Kakihana, F. Honda, A. Nakamura, D. Aoki, Y. Uwatoko, M. Nakashima, Y. Amako, T. Takeuchi, T. Kida, **T. Tahara**, M. Hagiwara, Y. Haga, M. Hedo, T. Nakama, and Y. Ōnuki,
   Physica B: Cond. Matt., **536**, 192 (2018).

Acknowledgment

The author wish to express my sincere gratitude to Prof. Masayuki Hagiwara at AHMF (Center for Advanced High Magnetic Field) in Osaka University for his patient guidance, valuable suggestions, enlightening discussions, and continuous encouragement. I wishes to express his gratitude to Dr. Yasuo Narumi at AHMF for teaching me the experimental techniques, valuable suggestions, and helpful advice. I also would like to thank Dr. Takanari Kida for teaching me the experimental techniques, valuable suggestions, and helpful advice.

I particularly acknowledge the following researchers; Dr. Kazumasa Miyake at Osaka University for theoretical suggestions. Dr. Tetsuya Takeuchi at Osaka University for helpful discussions. Prof. Hiroyuki Nakamura at Kyoto University for providing me the single crystal and powdered sample of $BaVS_3$, and helpful advice. Prof. Katsuya Shimizu and Dr. Tomoko Kagayama, Mr. Hidenori Fujita at Osaka University for teaching me the experimental techniques for applying pressure. Dr. Atsushi Miyake, Dr.Akihiro Kondo at University of Tokyo for teaching me the experimental techniques for applying pressure. Prof. Yoshichika Onuki and his group at Ryukyu University for providing me several Eu compounds. Dr. Khuong Huynh, Prof. Katsumi Tanigaki and their group at Tohoku University for providing me $BaMn_2Bi_2$ and its family samples. Dr. Hiroaki Shishido and his group at Osaka Prefecture University for providing me SmB_6/SrB_6 superlattice sample. Prof. Koichi Kindo at University of Tokyo for making the pulse magnet.

I wish to express my gratitude to the members of Hagiwara Laboratory in Osaka University, Dr. Mitsuru Akaki, Dr. Yuya Sawada, Mr. Kazuya Taniguchi, Ms.Yukiko Shibata, Ms. Mitsuki Torikoshi, Mr. Kazuki Sato, Mr. Reishi Ohta, Mr. Ryoto Mito, Mr. Kengo Nishii, Mr. Katsuki Nihongi, Mr. Daisuke Matsuzaki, Mr. Kouta Koshida, Mr. Tomoki Kikuta, Mr. Ken-ichi Fujii, and Etsuji Morikawa.

Acknowledgment (in Japanese)

本研究を進めるに際して多くの方のご指導を拝しましたこと、この場を借りて御礼申し上げます。

指導教員の萩原政幸教授には、学部 4 年生からあわせて 6 年間と長い間、大変お世話になりました。私が多大なご迷惑をお掛けしたにもかかわらず、見捨てることなく最後まで指導してくださり、感謝しています。

鳴海康雄准教授には、測定試料の決定をはじめ、直接的に指導して頂きました。研究が行き詰った時に指摘して頂いたことが核心を突く内容であることも多く、本研究をまとめる事が出来たのは鳴海先生の多大なるご指導、ご協力の結果です。

木田孝則助教は、実験技術の指導をはじめ、直接的に指導して頂きました。。今、研究が滞りなく遂行することができるのは木田先生の多大な精励による物だと感じております。

三宅和正招聘教授には、本研究の理論的な考察について、多くの部分をご協力いただきました。その豊富で深い知識に触発されて、多くの気づきを得ることが出来ました。深くお礼申し上げます。

大阪大学低温センターの竹内徹也助教には実験装置を貸していただいたほか、数々の助言をいただきましたこと感謝申し上げます。

谷口一也技官には、工作の際に毎回丁寧に指導して頂き、巧みな技術にいつも助けられました。毎回その技術力の高さに感銘を受けました。また研究で暗中模索していた私に温かい言葉をかけていただいたことが印象に残っております。深く感謝致します。

京都大学工学部の中村裕之教授には、単結晶および粉末 $BaVS_3$ 試料の作成およびご提供いただきましたことを感謝いたします。

大阪大学基礎工学部の清水克哉教授、加賀山朋子准教授、藤田秀紀氏、東京大学物性研究所の三宅厚志助教、近藤晃弘博士には、高圧力セルの使用方法の習熟やセルの改良等について、先人としてご協力いただきましたことを感謝します。皆さまのご協力無くしては本研究はありえなかったと思っています。

本研究で使用したパルスマグネット及びそれを用いた測定システムの開発者である東京大学物性研究所の金道浩一教授に感謝致します。

琉球大学の大貫惇睦客員教授のグループの方々、東北大学の Khuong Huynh 助教らのグループの方々、大阪府立大学の宍戸寛明准教授のグループの方々には、本論文に記載していませんが、共同研究に際して試料提供して頂くとともに、楽しく議論させていただいたことを大変感謝しております。

秘書の柴田由紀子さま、鳥越美月さまには、事務手続きをはじめ、研究生活全般を支えていただきましたことを感謝いたします。

赤木暢助教、澤田祐也博士には、日常的に考察に付き合っていただき、深く考察するきっかけを頂きましたまた、論文投稿や国際会議の参加に際して、面倒を見ていただいたこと、感謝しております。

博士後期課程まで同期として切磋琢磨した佐藤和樹氏については、一人では途中であきらめていたと思いますが、張り合うことで最後までやり抜くことが出来たと思います。ありがとうございます。

類似するテーマを研究している後輩の二本木克旭君、藤井健一君、森川悦司君には、自分の方法などを教えることを通して、多くのことに気づくことが出来ました。これからも頑張ってください。

太田麗嗣君、水戸陵人君、西井健剛君、松崎大亮君、越田洸匠君、菊田朋生君には、コロキウム等での質問を通して、問題点の整理を助けていただきました。感謝します。

有留那愉多君、金井田小夏さん、木村仁君、吐合慶亮君、常深文夫君、羽生魁星君とは、最後までともに研究を行えなかったことを残念に思います。コロキウム等を通

して優しく接することが出来なかったことをお詫び申し上げます。
最後に、私を支えてくれた方々に感謝します。